Opto-Mechanical Analysis of a Harsh Environment MEMS Fabry-Perot Pressure Sensor

by

Eric J. Brace

A thesis
presented to the University of Waterloo
in fulfillment of the
thesis requirement for the degree of
Masters of Applied Science (Nanotechnology)
in
Mechanical Engineering

Waterloo, Ontario, Canada, 2019

©Eric Brace 2019

AUTHOR'S DECLARATION

I hereby declare that I am the sole author of this thesis. This is a true copy of the thesis, including any required final revisions, as accepted by my examiners.

I understand that my thesis may be made electronically available to the public.

Abstract

The objective of this thesis is to develop an optically interrogated pressure sensor that is capable of measuring the applied fluid pressure in harsh environments. In its completed state, this sensor is intended be used in plastic injection moulding manufacturing in order to identify the current state of the plastic melt and optimize the process. An extrinsic fiber-optic Fabry-Perot pressure sensor, based on micro-electromechanical system (MEMS) is developed. A series of experiments are designed and carried out to validate the sensor's applicability for high temperature and pressure environments. Preliminary results are gathered using an existing silicon membrane in order to verify the concept, which was fabricated using anisotropic etching. Silicon on insulator (SOI) multiuser fabrication process is used to produce three designs of silicon membranes through Deep reactive-ion etching (DRIE). These devices are packaged with a stainless steel housing using epoxy to support the die and verify alignment between the fiber and reflective membrane. Once assembled, the Fabry-Perot cavity is formed between the membrane and fiber surface. Experimental results are collected using the proof of concept device for temperature ranges of 20 – 100 °C and gauge pressures from 0 - 1000 PSI, and for the SOI devices at room temperature and gauge pressures from 0 to 3000 PSI. Analysis of this data shows operating pressure ranges of 150 to 2300 PSI, maximum nonlinearity of less than 2.6% and sensitivities between 0.36 and 1.4 nm/PSI.

The experimental deflection results are compared against finite element and analytical models to verify the expected response. This is adjusted for temperature effects using predictions of material property temperature-dependence and thermal expansion. In order to examine the impact of fabrication methodology, a fixed-fixed support analytical model is compared to experimental data of the four membrane designs. It is found that the anisotropic etched membrane shows poor agreement with this analytical model, showing 570% greater sensitivity than predicted using the model. Finite element modeling of the system shows significant deformation in the membrane support structure, resulting in this greater sensitivity. A simply supported analytical model is also compared to the data, showing 100% greater sensitivity. This model is adjusted using a least squares procedure to fit the experimental data through modification of the support-defined leading coefficient. A high temperature trial shows reduced sensitivity to pressure, corroborating the predicted finite element behavior. Silicon on insulator DRIE membranes show similar error, on the order of 100%, when compared to the fixed-fixed analytical model. This model is adjusted in a similar manner to fit the experimental data.

The findings of this thesis suggest that unaccounted-for deflection is present in the membrane supports of DRIE and anisotropic etched MEMS devices, which significantly impacts sensor response to pressure. This results in higher sensitivity than analytically predicted occurring in the experimental trials of the as-fabricated devices. Future work should be focused on expanding the predictive power of MEMS membranes, stabilization of the optical signal and integration of temperature sensing to expand the capabilities of the device while correcting for real-time thermal aberration.

Acknowledgements

I would like to thank my supervisor, Dr. Patricia Nieva, for her ongoing support and guidance throughout my education. I would also like to thank my colleagues at the University of Waterloo SimsLab: Dr. Abdul Rahman Ghannoum for his mentorship and instrumental contributions to the project; Sepideh Ghaderian for her experimental support; Pedro Cordero for his contributions at the start of my work; as well as Axel Gonzales, Rishard Rameez and Rebecca Macarthur for their support and suggestions.

I would like to thank Ashwani Angra at MorHEAT Inc. for sponsoring this project while providing valuable industry insight and design improvements. I would like to acknowledge CMC Microsystems for the provision of products and services that facilitated this research, including fabrication, design and software support for the Silicon-on-Insulator chips. I would also like to thank Robert Wagner for his machining expertise and advice, as well as the Engineering Student Machine shop for their support and use of equipment.

Lastly, I would like to thank my friends and family for their love and support on the path that brought me here. You truly kept me going and moving towards progress throughout the challenges and triumphs.

Table of Contents

AUTHOR'S DECLARATION ii
Abstract iii
Acknowledgements v
Table of Contents vi
List of Figures viii
List of Tables xi
Chapter 1 Introduction 1
1.1 Motivation and Fields of Interest 2
1.2 Thesis Objectives and Organization 4
Chapter 2 Background 6
2.1 Fabry-Perot Interferometry 6
2.2 Reflection Cavity and Membrane Synthesis 9
2.2.1 Signal Demodulation 10
Chapter 3 Literature Review 12
3.1 Fabrication of Membranes and Sensors 12
3.1.1 Extrinsic Morphology 12
3.1.2 Intrinsic Morphology 15
3.2 Signal Collection 16
3.2.1 Linear Range Detection 16
3.2.2 Spectroscopy 18
Chapter 4 Membrane Design and Fabrication 20
4.1 SOIMUMPs Design 22
4.2 Design Analysis 25
4.2.1 Analytical Method 25
4.2.2 Finite Element Method 29
4.3 As-fabricated Custom SOI Inspection 34
Chapter 5 Optical System 36
5.1 Optical Path 36
5.2 Optical Components 38
Chapter 6 Packaging and Thermal Impact on Sensor Response 42
6.1 Packaging 42

6.1.1 Failure Condition - Thread Shearing 44
6.2 Full System Functionality Testing 45
6.3 Temperature Dependence of Material Properties 46
6.3.1 Silicon Membrane 47
6.3.2 Silicon Dioxide 49
6.4 Thermal Expansion of Components 50
6.4.1 Analytical Position Error Due to Packaging 50
6.4.2 Device Expansion 54
Chapter 7 Experimental Results, Validation and Discussion 57
7.1 Proof of Concept Trials 60
7.2 SOI Sensor Experimental Results 62
7.3 Experimental Verification and Discussion 67
7.4 Sensor Behaviour Characterization 74
7.4.1 Sensitivity 74
7.4.2 Dynamic Range 75
7.4.3 Grade of Linearity 76
7.5 Reproducibility and Error 78
Chapter 8 Conclusions 79
8.1 Contributions 80
8.2 Future Work 81
8.2.1 Prediction of Non-ideal Sensor Behaviour 81
8.2.2 Additional Stabilization 82
8.2.3 Environmental Protection 82
8.2.4 Expanded Functionality 82
8.2.5 Medical Applications 83
Appendix A – SE103 Data Sheet 84
Appendix B – On-chip Material Testing Devices 88
Appendix C - Predicted Sensor Response Graphs 92
Appendix D – Temperature Dependence of Sensor Response 100
Appendix E - Sensor Housing Drawing 107
Appendix F – Fiber Locator Drawing 109
Bibliography 110

List of Figures

Figure 1: Fabry-Perot ray diagram, reprinted with permission from [14] 6
Figure 2: Fringe field with R=0.8, reprinted with permission from [14] 7
Figure 3: Number of reflected modes vs. cavity distance in a Fabry-Perot device 8
Figure 4: Fabry-Perot pressure sensor optical cavity 9
Figure 5: Example of extrinsic Fabry-Perot device morphology – credited to W. J. Pulliam, P. M. Russler, and R. S. Fielder, “High-temperature high-bandwidth fiber optic MEMS pressure-sensor technology for turbine engine component testing,” in *Environmental and Industrial Sensing*, 2002, vol. 4578, pp. 229–238. [17] 13
Figure 6: Schematic of intrinsic Fabry-Perot pressure sensor © 2002 IEEE [11] 15
Figure 7: Visualization of linear range 17
Figure 8: Optical response intensity variation visualization – credited to W. J. Pulliam, P. M. Russler, and R. S. Fielder, “High-temperature high-bandwidth fiber optic MEMS pressure-sensor technology for turbine engine component testing,” in *Environmental and Industrial Sensing*, 2002, vol. 4578, pp. 229–238. [17] 18
Figure 9: Spectrometer signal response example © 2002 IEEE [11] 19
Figure 10: SE103 spec sheet dimensions (given in mm) [8] 20
Figure 11: SE103 membrane width measurement 21
Figure 12: SE103 PoC membrane dimensions – destructive testing 21
Figure 13: SOIMUMPs fabrication schematic, adapted from [32] 22
Figure 14: SOIMUMPs chip design masks 24
Figure 15: Design area visualization [32] 25
Figure 16: Predicted PoC fixed assumption model intensity 27
Figure 17: Predicted custom SOI membrane intensity, with 25μm thickness and 300μm width 28
Figure 18: FEA mesh convergence graph for PoC membrane simulated at 1000 PSI 30
Figure 19: PoC mapped bricks meshed model 30
Figure 20: PoC device FEA displacement results at 1000 PSI, top side 31
Figure 21: PoC device FEA displacement results at 1000 PSI, bottom side 32
Figure 22: PoC membrane von Mises stress visualization at 1000 PSI, top side 33
Figure 23: PoC membrane von Mises stress visualization at 1000 PSI, bottom side 33
Figure 24: As-fabricated SOIMUMPs chip membrane dimensions 35
Figure 25: As-fabricated SOIMUMPs etch cavity dimensions 35

Figure 26: Optical path design ... 37
Figure 27: Fiber probe tip - Top: Low temperature option, Thorlabs CFML21L10 Bottom: High temperature option, Thorlabs ferrule and custom machined support ... 38
Figure 28: PoC sensor cavity size visualization ... 38
Figure 29: Visualization of maximum collected reflection radius ... 40
Figure 30: Housing component – Left: Isometric view Right: Cross-sectional view ... 42
Figure 31: Packaging assembly cross-section view ... 43
Figure 32: Fiber locator - Isometric view ... 43
Figure 33: Thread diameter terminology visualization ... 45
Figure 34: Membrane and adhesive integrity verification ... 46
Figure 35: Silicon refractive index with respect to wavelength at 300°C [47] ... 48
Figure 36: PoC thermal expansion component visualization ... 50
Figure 37: SOI thermal expansion component visualization ... 51
Figure 38: 1000 PSI PoC maximum displacement dependence on Temperature ... 53
Figure 39: 1000 PSI 400 μm SOI maximum displacement dependence on Temperature ... 53
Figure 40: PoC FEA no applied pressure, 100°C – isometric view ... 54
Figure 41: PoC FEA no applied pressure, 100°C - side view ... 55
Figure 42: PoC FEA 1000 PSI 100°C - isometric view ... 56
Figure 43: PoC FEA 1000 PSI 100°C – cross-sectional side view ... 56
Figure 44: Experimental Set-up ... 59
Figure 45: LED breadboard ... 59
Figure 46: Normalized voltage response of chip 1 PoC from 0 to 1000 PSI in silicon oil, comparing results of five trials at 21°C ... 60
Figure 47: Normalized voltage response of chip 2 PoC from 0 to 1000 PSI in silicon oil, comparing results of three trials at 21°C ... 61
Figure 48: Voltage response of PoC chip 2 operation at various temperatures from 0 to 1000 PSI: 21, 40, 60, 80 and 100°C ... 62
Figure 49: Normalized voltage response of 200 μm SOI from 0 to 1000 PSI in silicon oil, comparing results of four trials at 21°C ... 63
Figure 50: Voltage response of 200 μm SOI from 0 to 3000 PSI in silicon oil at 21°C ... 64
Figure 51: Normalized voltage response of 300 μm SOI from 0 to 1000 PSI in silicon oil, comparing results of four trials at 21°C ... 65

Figure 52: 300 μm SOI oil test trial 5 raw data 0 to 1000 PSI at room temperature – significant variation in the response trend suggests that plasticity occurred 65
Figure 53: Normalized voltage response of 400 μm SOI from 0 to 1000 PSI in silicon oil, comparing results of two trials at 21°C 66
Figure 54: 400 μm SOI oil test trial 4 raw data 0 to 1000 PSI at room temperature – significant variation in the response trend suggests that plasticity occurred 67
Figure 55: PoC experimental results comparison with fixed and simply supported models, at room temperature with pressures from 0 to 1000 PSI 68
Figure 56: PoC experimental results comparison with adjusted model, at room temperature with pressures from 0 to 1000 PSI 69
Figure 57: 200 μm SOI experimental results comparison with fixed support model, at room temperature with pressures from 0 to 3000 PSI 70
Figure 58: 200 μm SOI experimental results comparison with adjusted model, at room temperature with pressures from 0 to 3000 PSI 71
Figure 59: 300 μm SOI experimental results comparison with fixed support model, at room temperature with pressures from 0 to 1000 PSI 72
Figure 60: 300 μm SOI experimental results comparison with adjusted support model, at room temperature with pressures from 0 to 1000 PSI 72
Figure 61: 400 μm SOI experimental results comparison with fixed support model, at room temperature with pressures from 0 to 1000 PSI 73
Figure 62: 400 μm SOI experimental results comparison with adjusted model, at room temperature with pressures from 0 to 1000 PSI 73
Figure 63: 300 μm SOI sensor characterization plot, average of trials 2-4 74
Figure 64: Linearity visualization 77
Figure 65: Vernier dimension visualization © 1995 IEEE 90

List of Tables

Table I: Summary of SE103 dimensions 21
Table II: SOIMUMPs layer thickness [32] 23
Table III: SOIMUMPs feature restrictions [32] 23
Table IV: Membrane performance design summary 26
Table V: FEA mesh convergence study for PoC membrane simulated at 1000 PSI 29
Table VI: Optical fiber specification comparison [38] [39] 39
Table VII: Refractive index of silicon at 830nm, as a function of temperature [46] 47
Table VIII: 304 SS coefficient of thermal expansion as a function of temperature [45] 52
Table IX: Comparison of predicted and experimentally observed sensitivity 75
Table X: Comparison of predicted and experimentally observed dynamic range 76
Table XI: Experimental grade of linearity 77
Table XII: Cantilever length calculation results 88

Chapter 1
Introduction

Fiber optic pressure sensors are an emerging technology in MEMS (Micro Electro-Mechanical Systems), the implementation of which enables new approaches to device design which can fundamentally change the limitations of sensing in industrial, transportation and medical applications [1]–[3]. These devices present a sensing modality that is able to interact with harsh environments while mitigating complications incurred through direct physical contact with the medium of interest, such as high temperature or abrasion of the sensor. Although there are many implementations of fiber optics for this purpose, Fabry-Perot interferometry is the primary focus of this work. These devices use light to detect fluid pressure through demodulating the deflection of a sensitive membrane.

Pressure sensing in plastic injection molding is critical to manufacturing process control, where inadequate pressure can result in low quality products while an excess may damage equipment and put workers at risk of injury during an accident [4]. Current industrial piezoresistive sensors are severely limited by the impact of temperature on their behaviour, denying manufacturers valuable in-process data. These sensors infer the pressure in the machine's barrel through membrane deflection, causing detectable resistivity changes in piezoresistive elements. Transfer fluids, such as mercury and silicone oil, are often used to protect the membrane from direct exposure to the plastic melt or to facilitate remote sensing. However, destabilization of the sensing elements (i.e. doped polysilicon films) and degradation or instability of the transfer fluids (e.g. silicone transfer fluids operate up to 300°C) make these devices incompatible with high temperature environments. In silicon components, mechanical destabilization occurs between 600 and 800°C, but electrical issues can begin as low as 150°C [5]. Mercury was historically used as the primary transfer fluid in these sensors, but it is now restricted by the Canadian Environmental Protection Act, 1999, Products Containing Mercury Regulations SOR/2015-254. In order to expand process characterization capabilities, this project presents an optical system able to sense pressure, corrected for the effects of temperature while operating in a harsh environment.

Currently available fiber-optic based devices have limited use in harsh environments, with devices in literature designed for operation in either high temperature or high pressure environments, but very few are capable of both. Currently commercially available premier piezoresitive pressure sensing systems operate in temperatures of 350 °C and pressures from 0 to 10000 PSI, but have high failure rates at temperatures above 400ºC [6]. Implementation of a successful device requires a system that is

able to adjust for temperature aberration of readings, resist the harsh chemical and abrasive environment of the plastic melt, while providing a platform for high resolution sensing. In previous works at the SIMS lab (Sensors and Integrated Micro-Systems Laboratory): a first attempt has been carried out, demonstrating the Fabry-Perot principle operating in this application [7]. A proof-of-concept system is developed using the diaphragm of existing piezoresistive sensors (BCM sensor SE103-100bar-A-II-OB-G8-DW [8]), which are packaged with a supplied MorHeat product housing and used for representative pressure testing. Since the time of ordering, the SE103 data sheet available online has been changed and the geometry does not match the chips tested in this work; the original is available in Appendix A. In this previous work, the optical path is conceptualized and a ferrule is implemented for maintaining stability of the fiber tip. However, the acquired sensor results were since found to not represent Fabry-Perot interferometric behaviour, as laser light was not used to acquire the optical signal nor were the chips adequately secured to the housing. Building on the previous work, the work presented in this thesis presents an optical and mechanical system which is redesigned to address these problems. Both current and previous testing of the device remains well within the material limits, using optical interrogation to determine the membrane deflection. Experiments from the previous work are repeated with the improved system, resulting in successful testing of the proof-of-concept device. These results are used to inform material and geometry decisions when designing the prototype presented in this work.

Through the research and selection of materials used to produce the membrane and optical fiber, a prototype device is designed to be capable of operating in harsh environment conditions of 300°C and pressures from in excess of 1000 PSI. This creates a platform for development of sensors for higher temperatures which are not limited by the restrictions of piezoresistive devices. Considering the temperature limitations discussed above, experimental results from the proof-of-concept are used to select the appropriate geometry to optimize resolution of the prototype sensor. The behaviour of this device is predicted by integrating solid mechanics and material science to approximate the temperature response: correcting for thermal expansion and the dependence of material properties on temperature.

1.1 Motivation and Fields of Interest

Piezoresistive sensors are the primary method used for pressure measurement in a variety of applications, such as: manufacturing process control, surgical intravascular monitoring, and engine optimization [3], [9]. These sensors are susceptible to errors and operational limitations due to their

dependence on electrical signals, such as RF (Radio Frequency) field interference and exposure to high temperatures disrupting their functionality. With the limited development of extrinsic FP sensors, there has been little integration of material science for correcting thermal expansion or material properties as a function of temperature. However, these principles have been extensively examined in other fields, presenting an opportunity to generate a novel model for prediction of MEMS membrane thermo-mechanical behaviour.

Utilizing the stability of fiber optic sensors at high temperatures allows for data collection in environments which are not viable for piezo-based devices. Implementation of this technology will enable expansion of pressure sensors into industries or applications for which it was previously not possible to implement quantified process control. Compared to piezoresistive sensors, fiber optic sensors offer a number of benefits, such as [10], [11]:

- Increased sensitivity
- Electrical passivity
- Dielectric construction
- Viability in harsh environments, such as:
    - High voltage
    - Electrically noisy
    - High temperature
    - Corrosive
- Applicability to measure many other parameters
    - Acoustic, magnetic, temperature, rotation, etc.
- Compatibility with optical fiber telemetry (wireless) technology
- Geometric versatility (flexible, able to be easily maneuvered)

Piezoresistive devices operate based on changes in the resistance provided by their sensing elements due to changes in their geometry (metals) or resistivity (semiconductors) [12]. However, the operating temperature of metal piezoresistive devices is limited to ~130°C, so are not viable for the harsh environment applications examined in this project. Semiconductor devices resistivity is related changes in the number and mobility of free electrons caused by lattice deformation. In crystalline semiconductors, gauge factors in the longitudinal and transverse directions are affected by the type and amount of doping, with response strongly impacted by the alignment of applied stress to the

crystallographic directions. As such, these devices are dependent on the stability of the doped material for their reliable operation.

1.2 Thesis Objectives and Organization

The objective of this thesis is to combine principles of solid mechanics and material science to develop a predictive model for high temperature membrane behaviour. Through integration of membrane deflection equations and finite element analysis with thermal expansion and temperature aberration of material properties, a multivariable approach is used to account for the impact of temperature on membrane-based pressure sensors. This model is used to design and fabricate an interferometric Fabry-Perot pressure sensor capable of operating at 300 °C and in excess of 1000 PSI. The presented system is modular and designed for easy alignment of the optical fiber with the membrane. Due to the removal of electronic components from the sensing area, the limitations on operating temperature result only from the mechanical limits of the materials selected.

Chapter 1 introduces the existing technologies used in harsh environment pressure sensing, with a focus on the motivations of creating the presented device. A short comparison of the capabilities of optical and piezoresistive technologies is presented, demonstrating the contribution to industry available in this project. Chapter 2 describes the theoretical background of the device, primarily discussing the operation of the Fabry-Perot interferometric principle as it applies to pressure sensing. In addition, sections are included detailing the implementation of thermal compensation and determining of material properties using microfabricated testing devices. Chapter 3 presents a literature review of the capabilities currently available in pressure sensing technologies. This explores the fabrication and sensing modalities most commonly used in state-of-the-art sensors. Chapter 4 describes the design and fabrication of the device membranes. This includes an analytical and FEA (Finite Element Analysis) examination of the expected membrane behaviour and a discussion of mechanical design principles applied in the system. This chapter describes both the Proof of Concept and a total of three different SOIMUMPs (Silicon on Insulator Multi-User MEMS Processes) devices. Chapter 5 outlines the design and components of the optical system, alongside a description of their expected performance. Chapter 6 describes the integration of the MEMS devices and the optical components into a packaging using CNC machined housing components, as well as an analytical and FEA model of the impacts of thermal expansion and temperature-dependence of material properties on the sensor's behaviour. Chapter 7 presents the experimental results acquired from the system with all four membrane types to verify its operation at high temperature and high pressure. An adjusted

mechanical model is developed to fit the experimental data is presented. In addition, a discussion of the behaviour characterization is presented. Finally, Chapter 8 describes the conclusions, contributions, future work and alternative applications of this device.

Chapter 2
Background

2.1 Fabry-Perot Interferometry

Fabry-Perot interferometers operate based on the formation of optical fringes through superposition of phase modulated beams of light [13]. These originate from an extended/diffuse source, which is focused onto an etalon (pair of partially-silvered mirrors) [14]. Within this cavity, the beam undergoes multiple internal reflections and transmissions, each resulting in a parallel outgoing beam. Cavities are classified as either extrinsic, where a supporting structure is used to form the second surface of the etalon, or intrinsic, where the cavity is created within the fiber structure [13]. When operating in transmission, beams may then be focused by a lens onto a single point on the screen; where the beams interfere either constructively or destructively, depending on their phase and path difference. This process occurs independently for each angle of incidence, generating an array of fringes with intensity varying due to the path difference between the interfering beams. Bright spots occur at the modes of the etalon, where constructive inference results in resonance of the rays. In order for this interference to occur, the examined light must be coherent (identical waves, with constant phase difference) and monochromatic (identical wavelength). A ray diagram depicting the system is shown below in Figure 1, with an example fringe field in Figure 2.

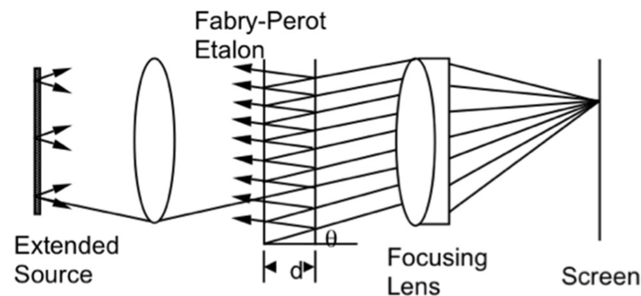

Figure 1: Fabry-Perot ray diagram, reprinted with permission from [14]

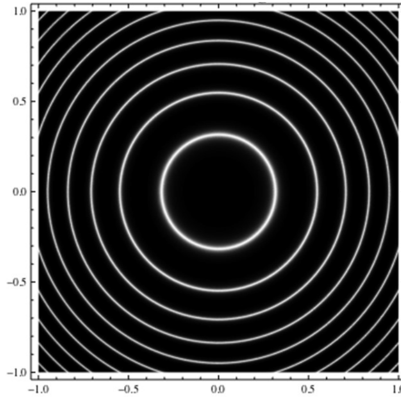

Figure 2: Fringe field with R=0.8, reprinted with permission from [14]

The governing equations of this phenomenon are given below: through the manipulation of parameters, this concept can be functionalized for sensing of deflection. The occurrence of fringe intensity maxima are found using Equation 1.

$$2nd\cos(\theta) = m\lambda \quad (1)$$

Where: n is the refractive index of the medium between the plates of the etalon, d is the distance between the plates, θ is the angle of incidence, m is the mode number and λ is the wavelength of the light. However, as the incident angle is limited to less than 90 degrees within an optical system, the periodic ambiguity of the cosine function is negated.

The modes of the etalon can be calculated using this equation to determine the incident angles that generate maxima. Through modulation of either the wavelength, or the distance between the etalon plates, the location of resonate modes can be modified and thus detected. This is the operating principle of pressure sensors using Fabry-Perot interferometry, which determine the deflection of the sensing membrane via the modification of this distance between etalon plates. In systems with a large distance between the etalon plates, relative to the wavelength, there exist a multitude of solutions to Equation 1and thus many viable modes of resonance. In optical fiber applications, the incident angles are limited by the acceptance angle of the fiber which can be calculated using the numerical aperture: which is defined as the sine of the acceptance angle, this calculation will be described in detail in later chapters. The admissible solutions to this equation will create a set of maxima for each etalon distance – however, this does not predict the intensity of the modes, or the intensity of their sum. Assuming that any angle below 90 degrees is acceptable, the number of viable modes increases by one for each half-wavelength increase in cavity distance - demonstrated in Figure 3.

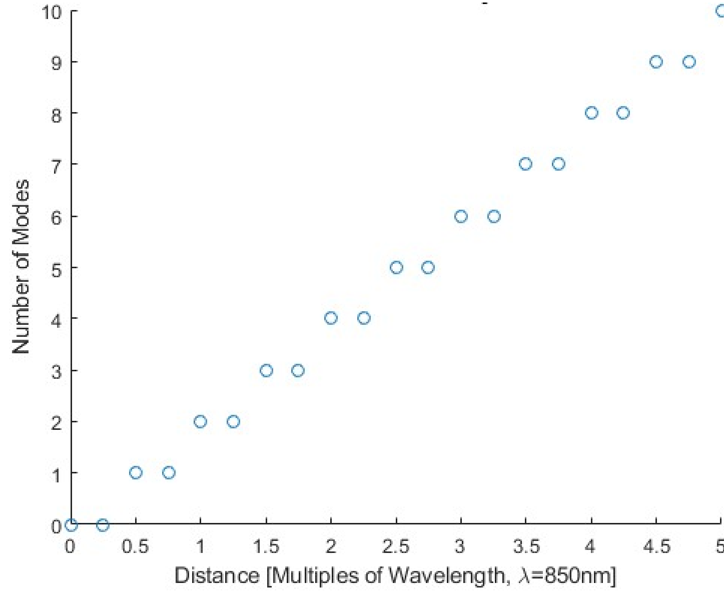

Figure 3: Number of reflected modes vs. cavity distance in a Fabry-Perot device

The reflected intensity of the device is predicted by averaging the interference behaviour of the electric field, as given by Equations 2 and 3 [1] [15] [16]. This Airy interference function is the principle model for the prediction of optical behaviour in Fabry-Perot pressure sensors and is used extensively in both the design and experimental validation of the device presented in this work. Derivation of this model is described in Hill's work, the final equation of which can be simplified into the form utilized here [16].

$$\frac{I_R}{I_o} = \frac{R_1+R_2-2\cdot\sqrt{R_1R_2}cos\phi}{1+R_2R_1-2\cdot\sqrt{R_1R_2}\cos\phi} \tag{2}$$

$$\phi = \frac{4\pi nL}{\lambda} \tag{3}$$

$$R = \left(\frac{n_i-n_t}{n_i+n_t}\right)^2 \tag{4}$$

Where: I_R is the reflected intensity, I_o is the initial intensity, R_1 and R_2 give the normal reflectivity of the etalon surfaces, ϕ is the round-trip phase shift of the primary mode, n is the refractive index of the medium between the etalon plates, L is the distance between the etalon plates, λ is the wavelength of the light, n_i is the index of refraction of the incident medium, and n_t is the index of refraction of the transmitted medium.

2.2 Reflection Cavity and Membrane Synthesis

Utilizing the theory discussed above to determine information about a system requires that the device is able to directly control or detect at least one variable in the governing equations as an input parameter. In pressure sensors, modification of the reflection cavity length is the primary methodology utilized and is applied in this project. A controllable optical cavity of the device can be created through various methods of fabrication, micromachining and in-fiber implementation being the most common. This is carried out by either creating an additional structure which interfaces with the optical system (extrinsic structure), or modification of the optical fiber itself to achieve functionalization (intrinsic structure), depending on the material requirements for the application.

In extrinsic systems, the etalon reflection cavity planes are composed of a thin film membrane and the surface of an optical fiber, as shown below in Figure 4 [17]. This arrangement allows for the light to behave in a similar manner to the theoretical system; where the parameter, L, from Equation 3 is defined by the gap between the two surfaces and varies with the pressure on the thin film. For the purposes of analysis, it is assumed that the deflections of the membrane are small and it remains parallel to the end of the fiber at all times. Coatings can be used to increase reflectivity of the membrane and fiber, which in turn increases the potential resolving power of the sensor.

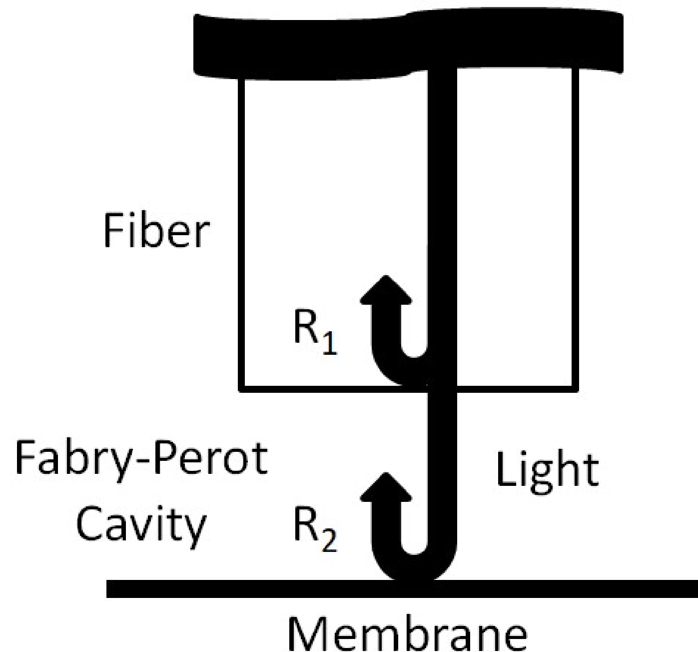

Figure 4: Fabry-Perot pressure sensor optical cavity

2.2.1 Signal Demodulation

Pressure of the system is determined by relating the intensity expression described in Section 2.1 to the mechanical response of the membrane. Through rearrangement and substitution of Equations 2 and 3, an expression for pressure in terms of material properties and optical intensity can be found, as follows. First, an Equation 2 is rearranged to find an expression for phase as a function of intensity as shown in Equation 5.

$$\phi = \cos^{-1}\left(\frac{I+IR_2R_1-R_1-R_2}{2I\sqrt{R_1R_2}-2\sqrt{R_1R_2}}\right) \tag{5}$$

Recall that L is defined by the cavity distance of the etalon, which modulates the deflection of the membrane. Substituting Equation 3 into Equation 5 and rearranging for L yields an expression of the cavity distance as a function of the intensity as shown in Equation 6:

$$L = \frac{\lambda}{4\pi}\cos^{-1}\left(\frac{I+IR_2R_1-R_1-R_2}{2I\sqrt{R_1R_2}-2\sqrt{R_1R_2}}\right) \tag{6}$$

For the purposes of this work, a square membrane is used – the deflection of which is defined by the thin film approximation as shown in Equation 7, which is valid for deflections smaller than 25% of the membrane thickness [15]:

$$\delta = \frac{P\alpha^4(1-v^2)}{4.2Et^3} \tag{7}$$

Where: δ is the orthogonal deflection of the membrane, P is the applied pressure, α is half of the membrane side-length, v is the Poisson's ratio, E is the elastic modulus and t is the thickness of the membrane.

By combining Equations 6 and 7 and rearranging, an expression for pressure is obtained in terms of the optical intensity. The final demodulation equation is given by Equation 8:

$$P = \frac{4.2Et^3\lambda}{4\pi\alpha^4(1-v^2)}\cos^{-1}\left(\frac{I+IR_2R_1-R_1-R_2}{2I\sqrt{R_1R_2}-2\sqrt{R_1R_2}}\right) \tag{8}$$

The behaviour of a membrane is approximated by a rectangular plate with all edges fixed as it is exposed to uniform loading: defined by Roark analytically as follows in Equations 9, 10 and 11 [18].

$$\sigma_{max} = -\frac{0.3078Pb^2}{t^2} \tag{9}$$

$$\sigma_{center} = -\frac{0.1386Pb^2}{t^2} \tag{10}$$

$$\delta_{max} = -\frac{0.0138Pb^4}{Et^3} \quad (11)$$

Where: σ is the membrane stress, δ is membrane deflection, P is distributed load given in $\frac{\text{Force}}{\text{Area}}$, b is the membrane side length t is membrane thickness and E is elastic modulus of the membrane material.

Should a circular membrane be used, the derivation presented above is modified by substitution of Equation 12, where R is the radius of the membrane [19].

$$\delta = \frac{3PR^4(1-v)}{16Et^3} \quad (12)$$

In addition to mechanical demodulation, the thermal behaviour of the sensor is considered through correcting for changes in material properties, thermal expansion and residual stresses as a function of temperature. As temperature increases, it is expected that the mechanical softening of the membrane and reduction of the cavity distance as the materials expand will result in erroneous pressure response data, giving higher pressure readings than the true value. In the case that the coefficient of thermal expansion of the membrane is greater than that of the substrate, this effect is expected to be further amplified by residual stresses - decreasing the membrane's stiffness through application of compressive axial loading to the system. These impacts will be further examined through analytical and finite element analysis in Chapter 4.

Chapter 3
Literature Review

Fabry-Perot pressure sensors are established in the literature for low temperatures and pressures, but are still emerging into the harsh environment space. In this section, previous works are presented and contrasted to the developed sensor – alongside an overview of manufacturing and signal collection techniques which have previously found success in the field. Existing work has been carried out on both single-material and SOI sensor compositions, the latter of which introduces CTE-mismatch errors at high temperatures which has available limited temperature ranges and must be considered when developing a predictive model. However, the majority of SOI sensors discussed in literature operate based on piezoresistive elements, which have temperature ranges limited to 500°C [20].

3.1 Fabrication of Membranes and Sensors

Fabrication of Fabry Perot pressure sensors is characterized into two general morphologies, referred to as extrinsic or intrinsic sensors. These categories indicate whether the sensor is fabricated through integration of the optical fiber with an external system, in the case of extrinsic sensors; or if the fiber is directly modified to introduce sensing capabilities, as is the case of intrinsic sensors.

3.1.1 Extrinsic Morphology

The primary fabrication method utilized in harsh environment applications is semiconductor micromachining, due to the favourable mechanical properties of these materials. This fabrication methodology is commonly used throughout pressure sensing applications and permits formation of materials such as silicon, silicon carbide, gallium arsenide, etc.; to compose the membrane and cavity through series of deposition and etching to generate the desired geometry [17], [21], [22]. The resulting device is bonded to an optical fiber, either directly or through integration of a larger housing system. Alignment of the fiber and membrane is critical in this step, as the operation of the system requires that the reflective surfaces of the etalon formed at this interface are parallel. This methodology permits the use of highly reflective mirrors, which can obtain high finesse interference signals. Additionally, this methodology is relatively simple, not requiring high cost equipment. However, extrinsic sensors often have low coupling efficiency, necessitate careful alignment (as mentioned above) and require supporting packaging (which can present additional issues) [13].

Pulliam et al. (2002) created an extrinsic Fabry-Perot using sapphire fiber adhesive fixed to a micromachined silicon substrate with silicon carbide bonded membrane; this is representative of extrinsic Fabry-Perot pressure sensors and is shown in Figure 5 [17]. This device is capable of operating up to 600°C, 750 kPa. Static pressure fluctuation testing is carried out in a turbine engine system and compared to piezoresistive sensor data. Despite significant apparent noise, uncalibrated fiber optic sensors demonstrate a clear correlation to the piezo-data and performed as expected with a high degree of repeatability. In this work, the impact of thermal drift on sensor behaviour is identified, but not quantified or predicted analytically; however, temperature compensation is mentioned without discussion of an implementation methodology.

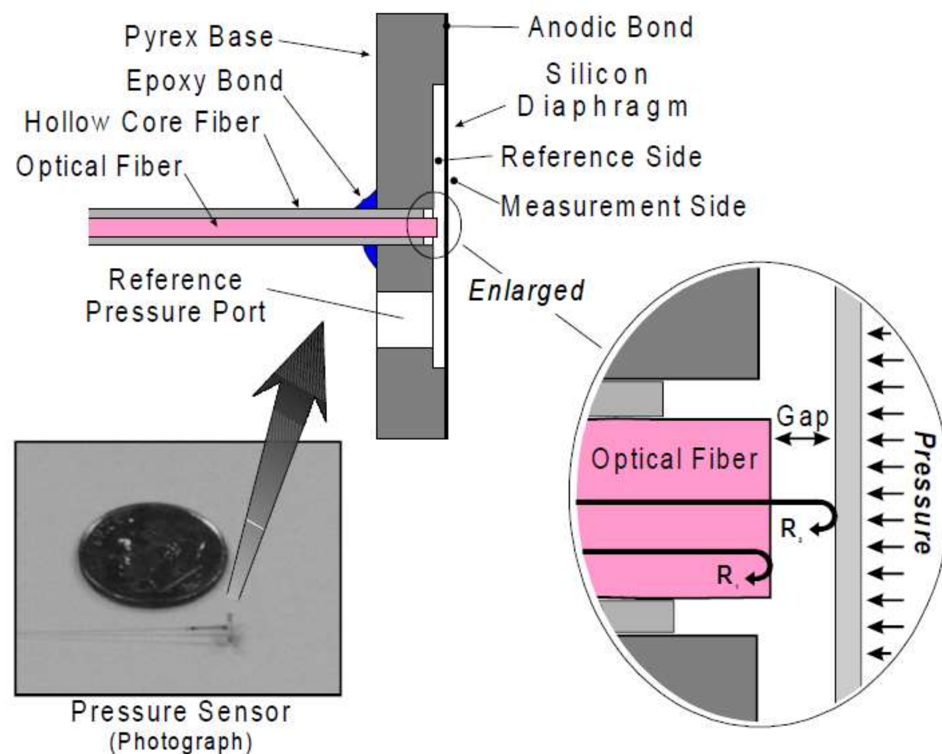

Figure 5: Example of extrinsic Fabry-Perot device morphology – credited to W. J. Pulliam, P. M. Russler, and R. S. Fielder, "High-temperature high-bandwidth fiber optic MEMS pressure-sensor technology for turbine engine component testing," in *Environmental and Industrial Sensing*, 2002, vol. 4578, pp. 229–238. [17]

Fang et al. (2016) developed a broadband Fabry-Perot pressure sensor, which is fabricated by anodically bonding a silicon micromachined membrane to a Pyrex glass substrate [23]. Light is

introduced by an optical fiber to reflect from the sputtered gold reflective surface on the back surface of the silicon membrane, thus generating a Fabry-Perot cavity. The sensing principle is based on detecting the shift in the selected reflected wavelength of interest (1550 nm in this paper) as the cavity length changes with pressure and temperature. Testing is carried out at constant temperature in a heated gas cylinder with four trials over the range of 20 – 300°C, at pressures from 0 – 600 kPa (87 PSI) in 100 kPa increments. A linear decrease in the primary reflected wavelength is observed over the tested pressure ranges, which is correlated to sensitivity on the order of pm/kPa. Decreases in sensitivity as temperature increases are observed when comparing the four temperature trials, with the sensor being most responsive at 20°C. A temperature response trial is also carried out at constant zero pressure, demonstrating a thermal drift as the reflected wavelength increases with temperature. Similar to the work presented by Pulliam, thermal drift is identified and demonstrated but not predicted using analytical model.

In a 2018 work, Jia et al. present a high temperature batch-fabricated CO2 laser fused device, which provides a low cost and highly repeatable fabrication process. Micromachined Pyrex glass wafers are anodically bonded to gold-plated silicon wafers using batch-fabrication to form the sensor head, and then fused to a single-mode fiber using CO2 laser to create the Fabry-Perot cavity. This sensor is integrated with a fiber Bragg grating, permitting data collection and compensation while operating in high temperature environments. Taking advantage of temperature decoupling, experimental results demonstrate maximum pressure reading errors of <1.05% while operating in pressures of 0–0.5 MPa (72 PSI) and temperatures of 20°C–350°C, with maximum nonlinearity of 0.4% [24]. This paper considers the change of material properties with temperature but does not consider the impact of thermal expansion on error and sensor response.

Similar work produced by Liu et al. (2018) utilized a thin circular ceramic membrane to determine pressure, with a pressure range up to 160 kPa, but a compensated temperature range of 20-300°C with sensitivity of 0.205 nm/kPa [25]. In another, Wang (2008) achieved pressure ranges of 0-30 MPa, between 18 and 300°C, with an accuracy of 0.03MPa using a multiplexed pressure and temperature sensor [26]. However, this structure is immersed in the liquid and cannot be used for the turbulent flow experienced in the presented work

In all these presented works, there is evidence of extrinsic pressure sensors most commonly operating with compensation in temperatures of 300°C but limited to pressures of 100 PSI. In this

thesis, this pressure range will be expanded to 1000 PSI and a comparison of the mechanical behaviours of anisotropic and DRIE etched membranes is carried out on SOI constructions.

3.1.2 Intrinsic Morphology

Through modification of the fiber itself, functionalization the system can be achieved without the need to fabricate a separate membrane. These methods, which form an intrinsic Fabry-Perot cavity, can be accomplished in a variety of manners, such as: micromachining of the fiber, fiber Bragg gratings (FBGs), chemical etching, and thin film deposition [13]. By forgoing the need for packaging, intrinsic sensors feature extremely low form factors, which excel in fields such as medicine and immersed fluids; however, the cost of implementation varies considerably based on the methodology utilized and the materials may have poor mechanical properties which limit their applicability to harsh environments.

In one example, the fiber is dip etched in HF to form the optical cavity; this is accomplished by utilizing the fact that the core of the fiber is made up of germanium doped material, which etches faster than its un-doped cladding [11]. Upon creation of the cavity, the fiber is dipped into a polymer solution (P-1190A in dimethyl formamide), forming a membrane which spans the opening. The properties of this membrane depend on the concentration and drying speed of the solution. A schematic of this device is shown below in Figure 6, which is representative of the general morphology of intrinsic Fabry-Perot pressure sensors.

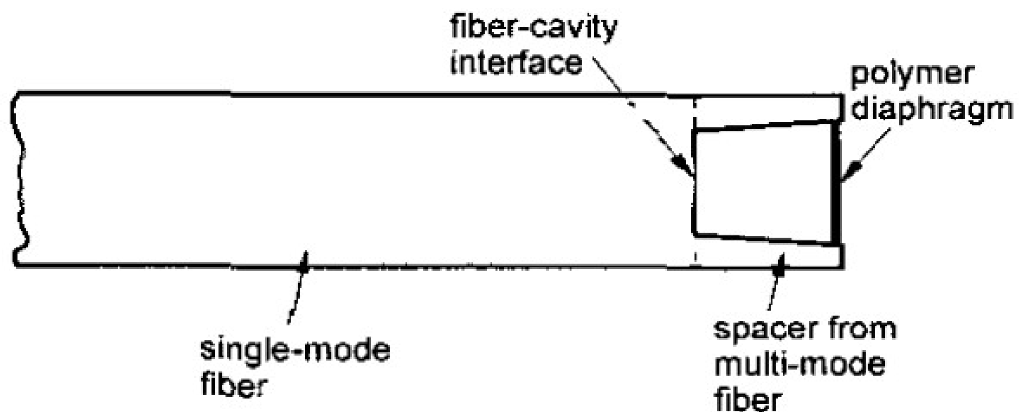

Figure 6: Schematic of intrinsic Fabry-Perot pressure sensor © 2002 IEEE [11]

In 2013, Zhang et al. present a sensing head which is formed using a laser micromachined Fabry-Perot air cavity and a fused-silica diaphragm. The outer surface of the diaphragm is thinned and roughened using a femtosecond laser, with minimum thicknesses of 2.6 μm. Experimental trials yield

a sensitivity of 2.8×10^{-4} nm/Pa and resolution of 180 Pa in pressures up to 60 kPa. At temperatures up to 700°C, a linear response to temperature is observed, with low pressure-temperature cross-sensitivity of 15.86 Pa/°C. However, these values do not include temperature compensation and errors of ~2% are observed between the calculated and measured pressure values in autogenic water pressure testing up to 200°C [27].

Wu et al. (2011) report forming a FPI cavity using a commercially available fusion splicer to splice a solid-core photonic crystal fiber to a standard single-mode fiber. Using wavelength shift as the sensing modality, this sensor generates excellent harsh environment experimental measurements in pressures up to 40 MPa (5801 PSI) and temperatures up to 700 °C, with sensitivities of ~5.8 pm/MPa and ∼13 pm/°C, respectively. Thermal expansion and changes in refractive index are approximated analytically, which show good agreement with the experimental linear fitted slope data [28].

These in-fiber sensors present large variation in available temperature and pressure ranges due to the variety of material and fabrication techniques. The presented works offer much higher temperatures and pressures than the extrinsic morphologies, but their fragility makes them difficult to apply to turbulent flow applications.

3.2 Signal Collection

Signal from the device can be collected through the measurement of a number of different optical parameters, each of which presents the information available from the system through significantly different means. Two such possibilities are discussed in detail in the following sections.

3.2.1 Linear Range Detection

Linear range detection utilizes the linear region of the sensor response profile to measure the amplitude shift due to etalon deflection [29]. Path difference can be accurately captured using this method and high sensitivity is achieved, the linear operation region is shown in Figure 7. However, by utilizing a narrow band of source wavelengths, ambiguity is present in the signal due to the periodic nature of the signal, as observed in the response data.

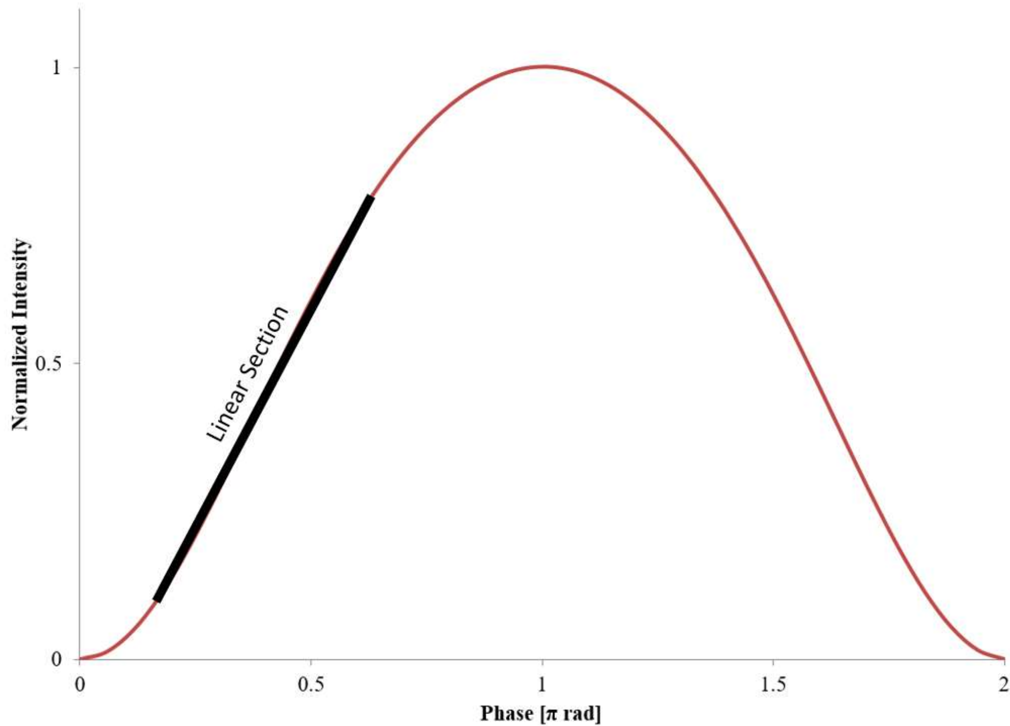

Figure 7: Visualization of linear range

In addition, there may be an amplitude loss visible in the data, as shown in Figure 8 [17]. The overall shape occurs due to two phenomena: the periodic nature of the interference of light, and the decrease in intensity due to diffusion over the absolute distance between the collection surface and the reflection surface. A photodiode provides an inexpensive solution to measure the total absolute intensity but is not able to correct for the ambiguity in the signal. By contrast, Charge Coupled Devices (CCD) also gather position information and convert it into voltage by collecting and mapping the charge incident on the collector [30]. Although CCDs provides excellent resolution, the components are quite expensive and requires a complicated demodulation algorithm which utilizes the fringe pattern to account for the periodic ambiguity [31].

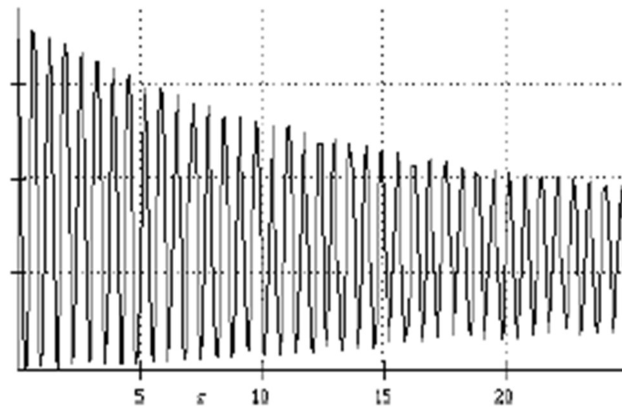

Figure 8: Optical response intensity variation visualization – credited to W. J. Pulliam, P. M. Russler, and R. S. Fielder, "High-temperature high-bandwidth fiber optic MEMS pressure-sensor technology for turbine engine component testing," in *Environmental and Industrial Sensing*, 2002, vol. 4578, pp. 229–238. [17]

3.2.2 Spectroscopy

Using a spectrometer, the system measures frequency shift in the reflected light as it passes through the etalon [11], [21]. As light phase passes through the etalon, the phase changes it experiences is dependent on the period of vibration of its wavelength. Consequently, different wavelengths will experience varying degrees of interference when they are recollected by the fiber, resulting in a shift of the intensity spectra. The deflection of the membrane is modulated through this intensity function as it changes with movement of the etalon cavity. By using a broad spectrum of incident light, this method does not depend on the specific fringe pattern generated by the etalon. By avoiding the periodicity ambiguity found in CCD collection, devices are permitted sensing wide pressure ranges without recalibration [11]. While this method simplifies the demodulation of the signal, it also results in a lower sensitivity when compared to linear range detection.

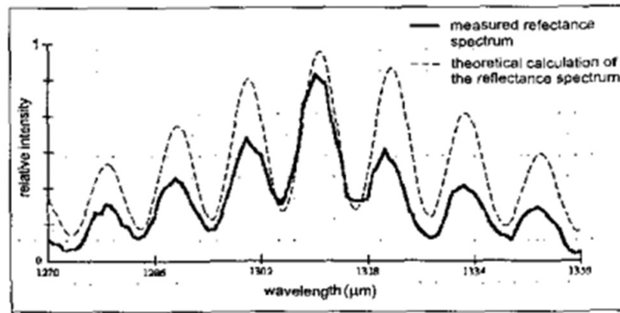

Figure 9: Spectrometer signal response example © 2002 IEEE [11]

In a 2006 article, Li et al. present an extrinsic diaphragm fabricated using Si micromachining, which measures shifts in the respected optical spectrum in order to determine the applied pressure. Using this method, the minimum detectable change in pressure was 0.99 kPa, with a sensitivity of 10.07 nm of spectral shift per MPa over a range of 0.2-1.0 MPa. However, temperature dependency was not examined in this work, so it cannot be compared to linear range sensors [21].

Chapter 4
Membrane Design and Fabrication

The system design is carried out through a combination of analytical and finite element methods, with a focus on the thermo-mechanical behaviour of the membrane. Geometry is calculated in order to optimize operating range, and sensitivity of the device to pressure.

Two membrane morphologies are examined in this study: an existing die purchased from BCM sensors (SE103-100bar-A-II-OB-G8-DW [8]), and a custom-fabricated die using SOIMUMPS. The dimensions of the custom membrane design are based on examination of the SE103 die, to ensure that similar performance metrics are achieved and their results can be compared. Dimensions and morphology of the SE103 PoC die, as provided by the manufacturer, are shown in Figure 10; note that no information with regards to the thickness or size of the membrane is provided. The cavity is sealed with a glass constraint, which requires that a hole is drilled in order to functionalize the SE103 die through insertion of the fiber optic sensor.

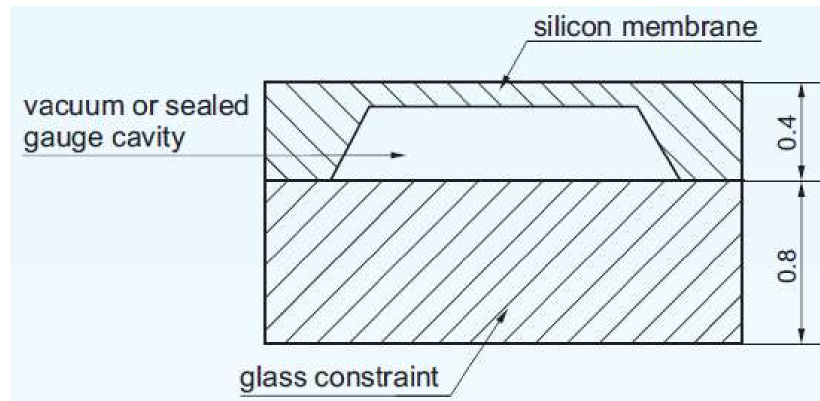

Figure 10: SE103 spec sheet dimensions (given in mm) [8]

The remaining dimensions of the SE103 die are determined through visual inspection and destructive testing. A drilled die is first examined by inspecting the back-side of the chip under a microscope to determine the membrane width, as shown in Figure 11. This die is then fractured using a diamond blade and examined under a microscope to find the membrane thickness, as well as confirm the width and etch angle; this is shown below in Figure 12. Finally, the extracted dimensions are summarized in Table I.

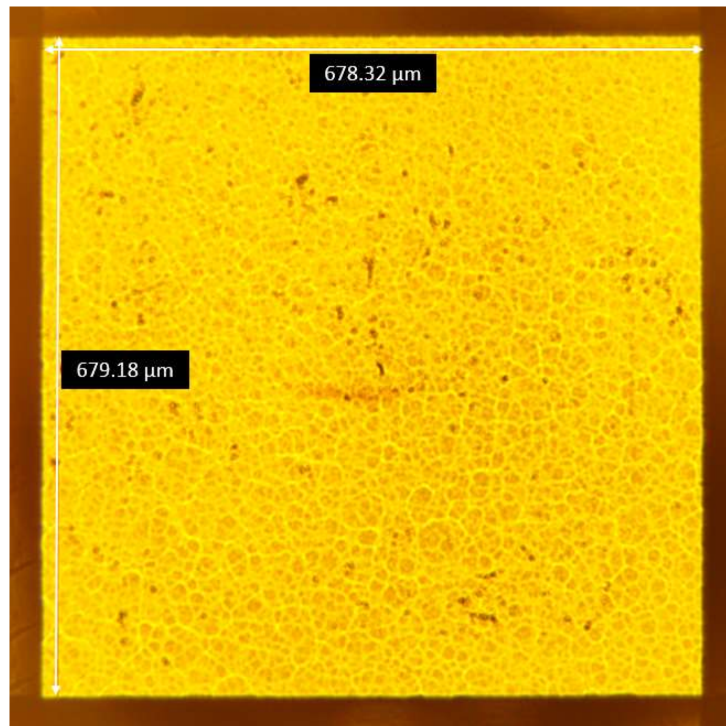

Figure 11: SE103 membrane width measurement

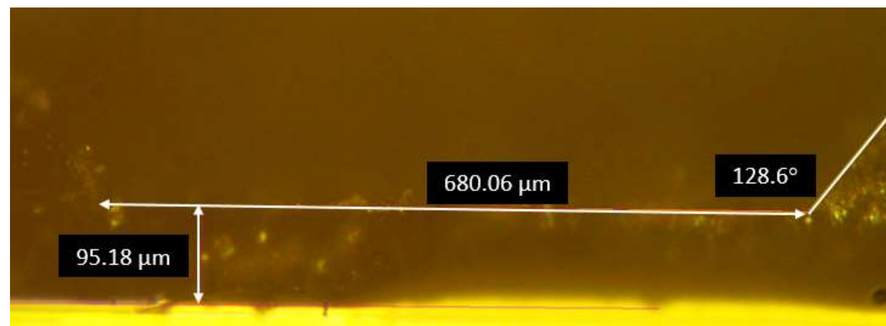

Figure 12: SE103 PoC membrane dimensions – destructive testing

Table I: Summary of SE103 dimensions

Silicon Wafer Thickness (µm)	400
Glass Constraint Thickness (µm)	800
Membrane Thickness (µm)	95.18
Membrane Width (µm)	680.08
Membrane Etch Angle (°)	128.60

4.1 SOIMUMPs Design

SOIMUMPs fabrication, provided by MEMSCAP, is utilized to produce the custom prototype dies. This provides a reliable and consistent device platform, through taking advantage of an established and characterized methodology. The chips are manufactured from a SOI (Silicon on Insulator) wafer, which is comprised of two layers of single crystal silicon with an insulating layer of silicon dioxide between them.

Fabrication is carried out through first depositing the pad metal using a liftoff process to form the fine metal features of the chip. Then the chip's silicon layer is pattered and DRIE etched to form the mechanical structures of the device. A similar process, referred to as the trench cut, is carried out on the substrate (also referred to the handle) layer which allows through-hole structures to be formed. The exposed oxide layer is then removed, providing access to the back side of the device layer. Finally, coarse metal features are formed using a shadow-masked process, which blankets exposed areas of the device using E-Beam evaporated metal. A schematic impact of each step on the final geometry of each layer is shown below in Figure 13. The SOI membranes used for this project are formed using a square trench cut of the substrate layer, the size of which determines the membrane side length of the final device. Device layer thickness options of 10 or 25 μm are offered, which defines the final thickness of the membrane for the purposes of this analysis. The thicknesses of each layer are shown in Table II below. The full fabrication details used to produce the dies described in this project are described in SOIMUMPs Design Handbook Revision 8 [32].

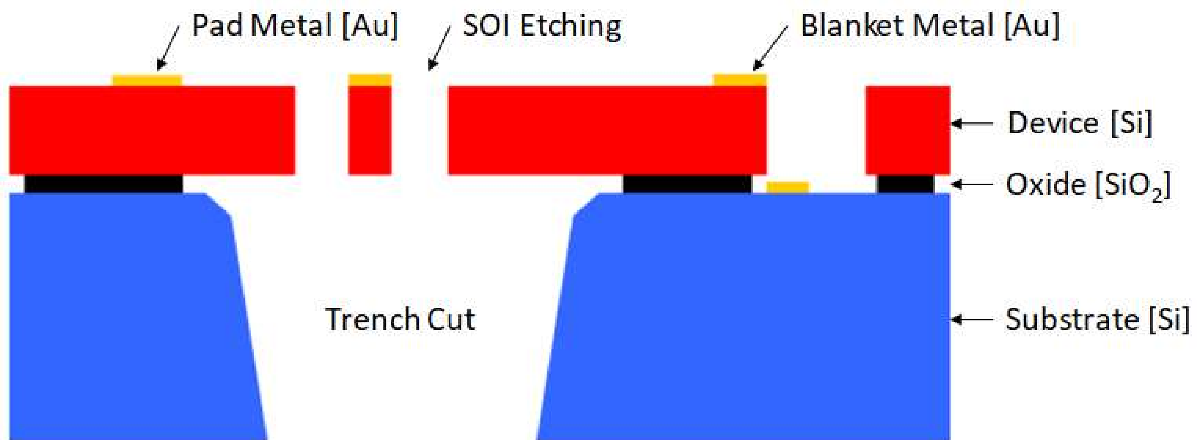

Figure 13: SOIMUMPs fabrication schematic, adapted from [32]

Table II: SOIMUMPs layer thickness [32]

Layer	10 µm Thickness (µm)	25 µm Thickness (µm)
Device (Si)	10 ± 1	25 ± 1
Oxide (SiO_2)	1 ± 0.05	2 ± 0.1
Handle (Si)	400 ± 5	400 ± 5

When submitting for SOIMUMPs fabrication, design rules (as outlined in the handbook) must be followed to ensure that the resulting chips are properly produced. These rules place limitations on the possible geometry of the prototype chips and must be considered in their design and analysis. The most significant limitations are summarized below in Table III. The “Center to Center” tolerance indicates the top-to-bottom alignment of any features in the layer; this tolerance may result in geometries being offset from their intended position. “Edge to Edge” tolerance accounts for boundary variations in the geometry profile, such as the etching profile of the through holes in the Substrate layer. These through holes also require that no released devices are included on tested membrane chips, as they would compromise the integrity of the fluid barrier. In addition, all geometries present in the PADMETAL layer must be enclosed by silicon on all edges by at least 3 microns, to ensure stability of the metal. Finally, implementation of “dimple” features reduces the likelihood of stiction in closely-spaced, long, narrow beams, by reducing the available surface area during release process.

Table III: SOIMUMPs feature restrictions [32]

Layer	Minimum Feature (µm)	Required Spacing (µm)	Center to Center Tolerance (µm)	Edge to Edge Tolerance (µm)
SOI (Si)	2, if orthogonal	2	-	-
Trench	200	200	±5	+50
Pad Metal	3	3	±3	±3
Blanket Metal	100	100	±35	±40

In a standard SOIMUMPS order, four unique chip designs can be produced in sets of fifteen pieces by utilizing the sub-dicing options provided. This presents the opportunity to create chips of three different membrane side lengths, in addition to one which includes material characterization devices.

These characterization devices (detailed in Appendix B) are used to determine the elastic modulus and residual stress present in each set of membranes, which may vary depending on their specific fabrication conditions – such as the local temperature and chemical makeup at the specific location on the wafer. Selection of the membrane side lengths is presented in Section 4.2, alongside an analysis of their expected behaviour. As a consequence of the limitations of the fabrication method, particularly in the feature size of the Trench layer, a minimum membrane side length of 200 μm is established. The masks submitted to MEMSCAP for fabrication are shown below in Figure 14. The full size of the delivered chips is 11.15mm x 11.15mm, but the design area is restricted to 9mm x 9mm due to the masking process – this is shown below in Figure 15.

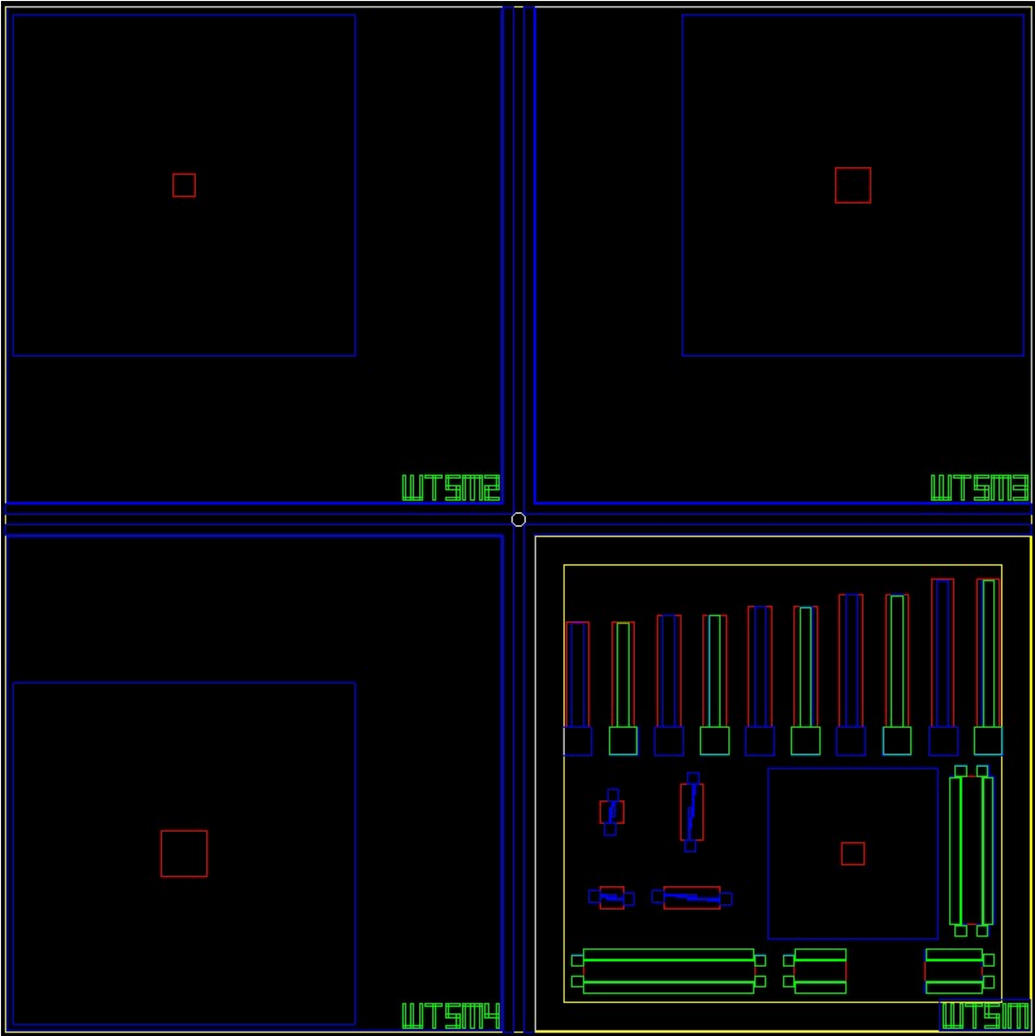

Figure 14: SOIMUMPs chip design masks

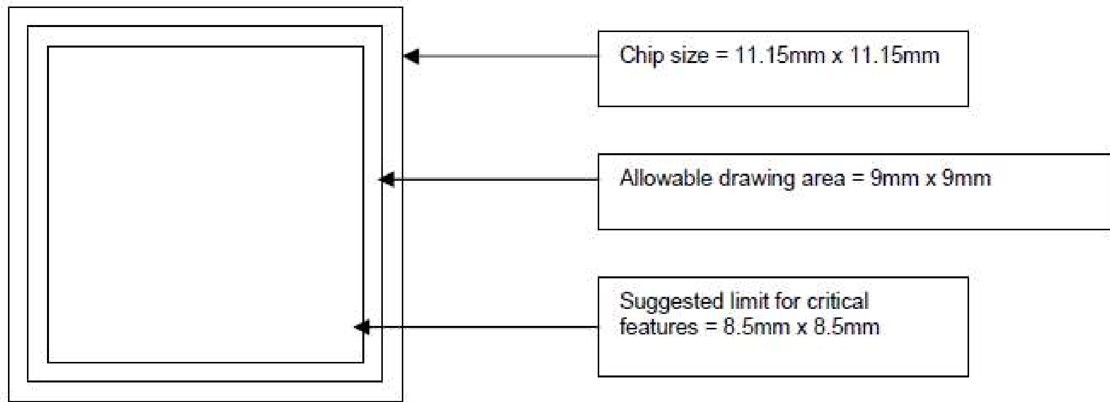

Figure 15: Design area visualization [32]

4.2 Design Analysis

Utilizing the dimensions determined in the sections above, the following sections describe the expected mechanical behaviour of the PoC membrane as predicted using finite element and analytical methodologies.

4.2.1 Analytical Method

The membrane response is predicted analytically using the equations described in Section 2.2.1. . Calculated displacement is used to determine the resulting cavity distance by subtraction from the initial distance of the cavity at zero applied pressure, shown in Equation 13. Initial cavity distance, given by L, is defined as the distance between the end surface of the optical fiber and the surface of the membrane. As the device is operating in a plate bending behaviour geometry, the elastic modulus is taken as 170 GPa at room temperature, as per Hopcroft's 2010 study [33]. This is corroborated as 167.7 GPa at 25°C, as determined using the temperature dependent equation in section 6.3.1 [34].

$$L_{cavity} = L_{initial} - \delta \quad (13)$$

The resulting intensity of the reflected light is approximated by substituting cavity distance into the path difference relation as follows in Equation 14. This approximation only considers the theoretical optical behaviour of the reflection cavity, assuming the surfaces are perfectly parallel and no other losses are occurring; this does not account for rays that are not collected by the fiber or coupling inefficiencies.

$$\phi = \frac{4\pi n L_{cavity}}{\lambda} \quad (14)$$

Failure pressure of the membrane is determined by calculating the applied pressure at which the maximum stress exceeds the yield stress of silicon. Using Roark's expression for maximum stress and rearranging for pressure, the applied failure load is given by Equation 15, where average fracture strength at room temperature is 3.33 GPa [35].

$$P_{failure} = \frac{\sigma_{max} t^2}{0.3078 \ ^2} \quad (15)$$

The results of the analytically estimated membrane performance are summarized below in Table IV for both the PoC device, as well as various combinations of custom membrane thicknesses and widths. It is observed that a custom membrane with thickness of 10μm has comparably much lower failure pressure than the 25μm option and is not able to meet the goal of detecting pressures approaching 10000 PSI. As such, the more durable 25μm thickness option is selected for further investigation and development of the custom membrane. The mechanical sensitivity of the sensor to an applied pressure is approximated by calculating the per-unit displacement response. Through which it is also observed that as the side length increases in the custom membrane, higher sensitivity is achieved in exchange for a lower failure pressure. Consequently, devices are designed to present two directions of performance: lower pressure range with high sensitivity, or high pressure range with reduced sensitivity.

Table IV: Membrane performance design summary

	Thickness (μm)	**Side Length (μm)**	**Failure Pressure (PSI)**	**Sensitivity (nm/PSI)**
PoC Device	94	681	27509	0.139
Custom 10 - 200	10	200	3534	0.685
Custom 10 - 300	10	300	1571	3.47
Custom 10 - 400	10	400	884	10.96
Custom 25 - 200	25	200	22088	0.0435
Custom 25 - 300	25	300	9817	0.220

Custom 25 - 400	25	400	5522	0.696

Visualization of the expected membrane behaviour is carried out by graphing the relationships described above with respect to pressure using Matlab. The calculated maximum displacement, cavity distance, stress response relative to yield and ideal intensity response to pressures up to 1000 PSI are compared for the PoC and custom membranes with widths of 200-450µm in steps of 50µm. Intensity response graphs for PoC and 300µm width are shown in Figure 16 and Figure 17, respectively; further characterization for all sensor designs can be found in Appendix C. It is observed that over the 1000 PSI range, the PoC membrane intensity remains fairly linear and does not significantly demonstrate periodicity of the response – assuming that the initial cavity distance is set such that initial intensity is at its minimum. By contrast, the 300µm custom membrane demonstrates greater sensitivity to applied pressure and the characteristic sinusoidal trend is observed in the intensity response. However, in both cases, the membrane does not approach failure over the examined pressure range when compared to a yield strength of 3000 MPa.

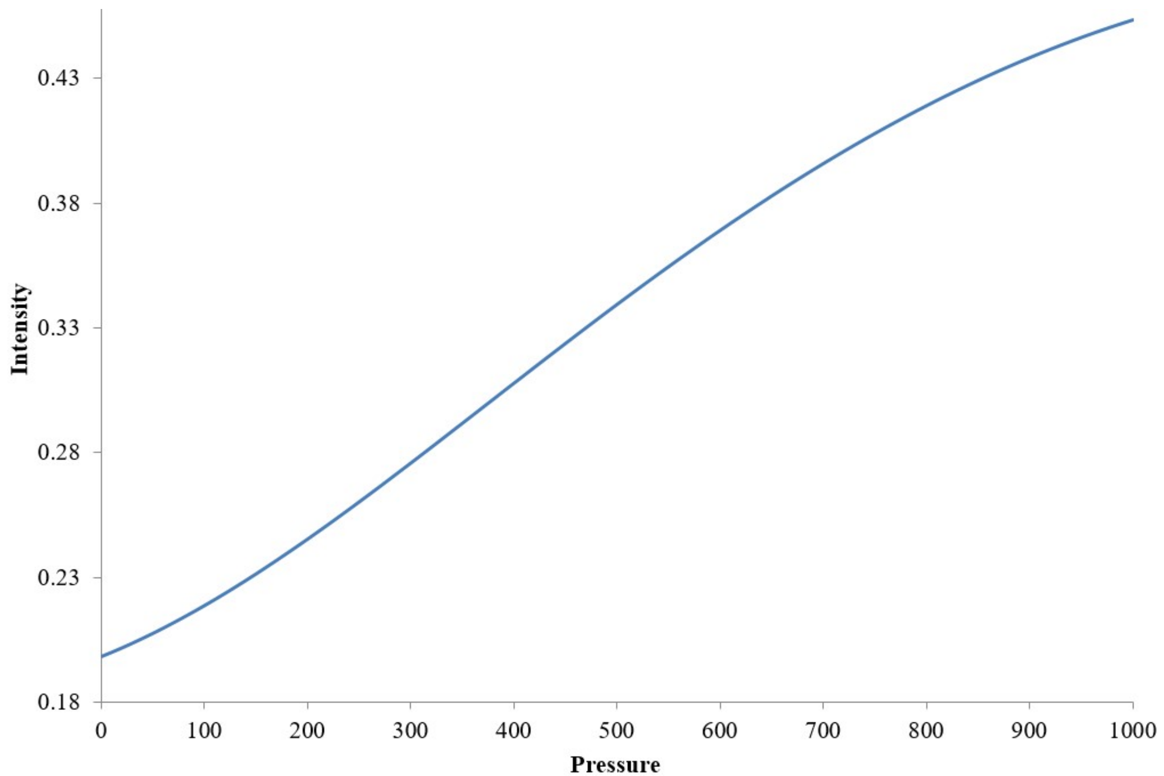

Figure 16: Predicted PoC fixed assumption model intensity

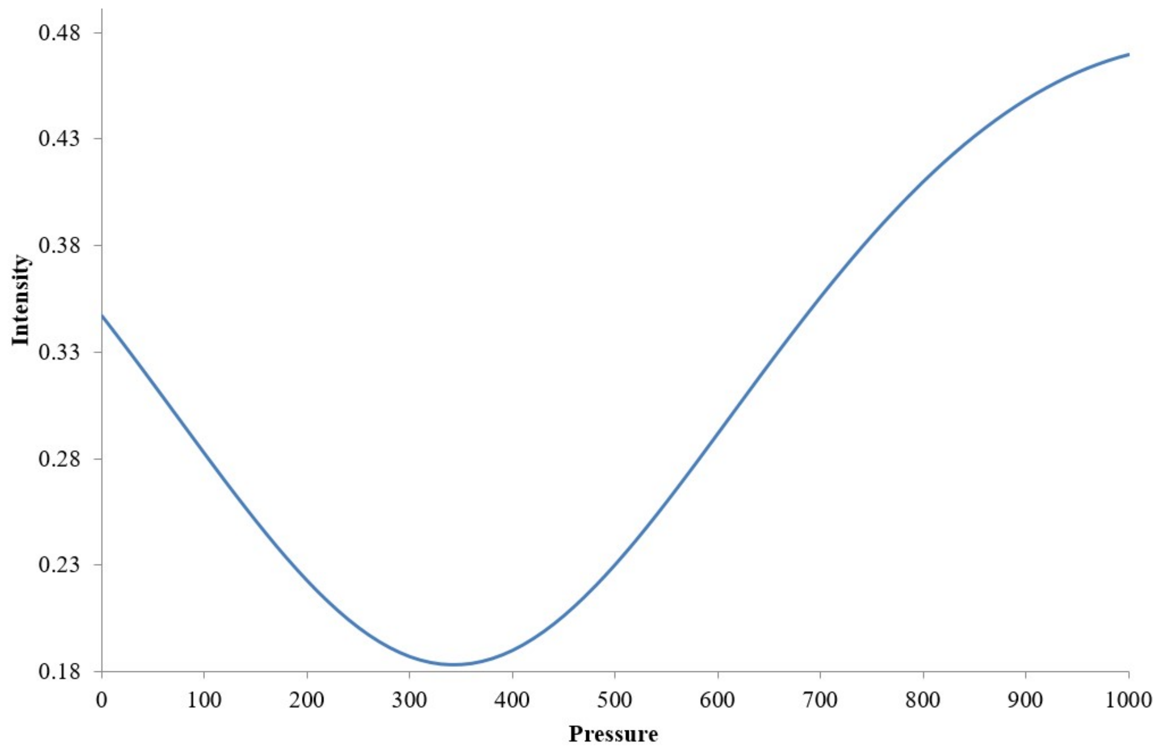

Figure 17: Predicted custom SOI membrane intensity, with 25µm thickness and 300µm width

4.2.2 Finite Element Method

Coventorware finite element modeling is used to verify the analytical prediction of the membrane's response to pressure. This model includes the sensing membrane, as well as the surrounding silicon supporting material. It is assumed to be fixed in all directions at its bottom surface, reflecting the housing surface which the chip rests on; fixing the device in z; and the epoxy used to secure its movement; fixing the device in x and y. Pressure is applied to the entirety of the top surface, including both the membrane and the supporting material, as will be the case in the final application. The housing assembly will be described in more detail in Section 6.1. Parabolic mapped bricks are selected for meshing, which creates sections of higher mesh density based on the partitioning of the model. A mesh convergence study is performed to ensure reliability of the FEA results. Through comparison of the maximum predicted membrane displacement, a relationship between the number of elements and the convergence of the model result is determined: shown below in Table V and Figure 18. The final meshed model using element size 30 is shown below in Figure 19.

Table V: FEA mesh convergence study for PoC membrane simulated at 1000 PSI

Element size	Number of Elements	Maximum displacement (μm)	Time to complete (hr:min:sec)
100	4000	0.4383	0:00:19
50	27520	0.4405	0:03:00
40	60200	0.4465	0:09:15
30	152196	0.4477	0:45:30
25	256000	Did not converge	Did not converge

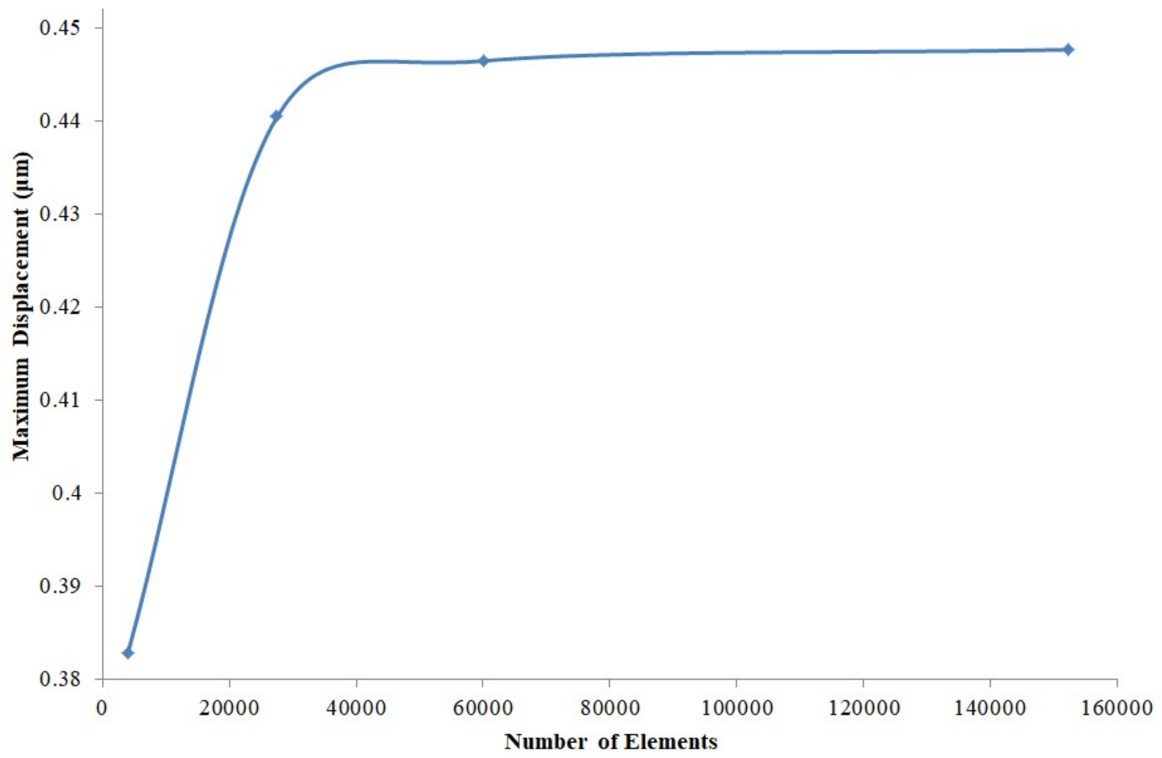

Figure 18: FEA mesh convergence graph for PoC membrane simulated at 1000 PSI

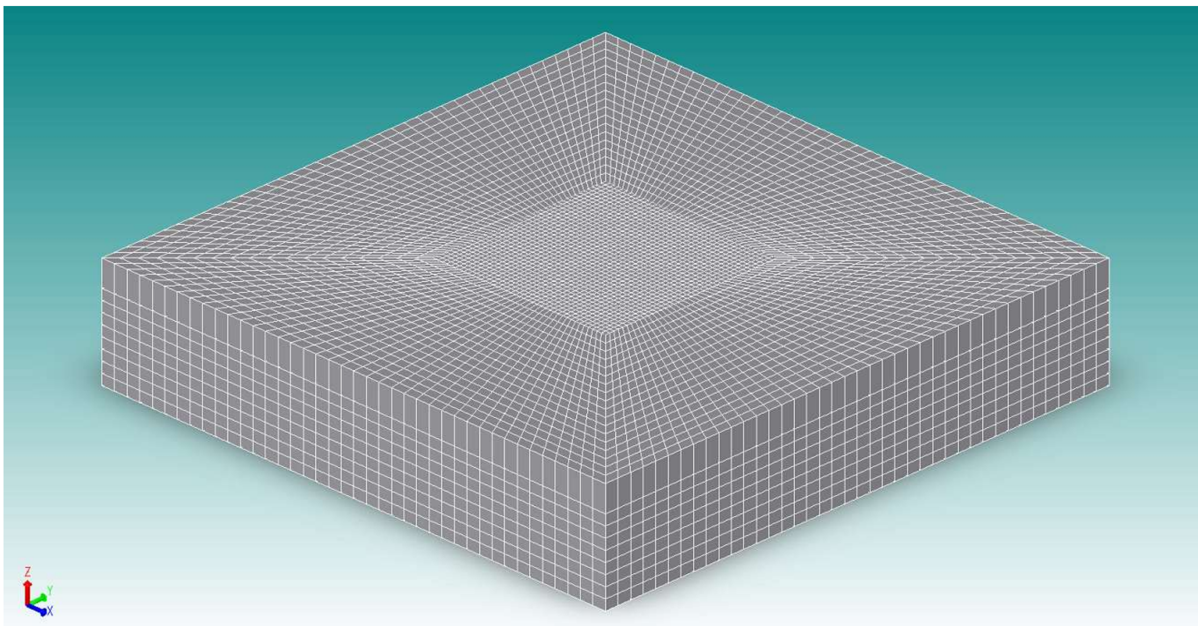

Figure 19: PoC mapped bricks meshed model

Predicted maximum displacement is found to be significantly higher than the fixed support analytical model; where the FEA and fixed model predict values of 0.4477 and 0.143 μm, respectively at 1000 PSI. Through examining the FEA displacement results (Figure 20 and Figure 21), it is clear that deformation is present in the supporting structure of the membrane which indicates non-ideal membrane support. This results in significant softening of the sensor's response to pressure and changes in the loading conditions as the supports deform, which can manifest in load rotation at high deflection and irregularities due to varying thickness.

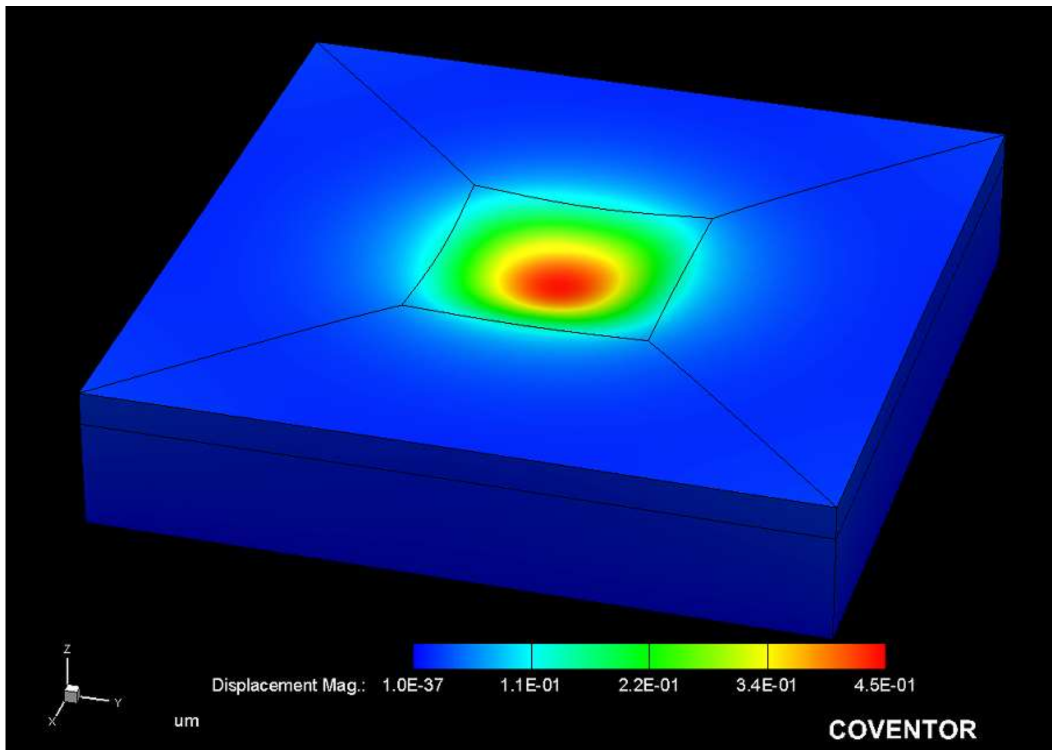

Figure 20: PoC device FEA displacement results at 1000 PSI, top side

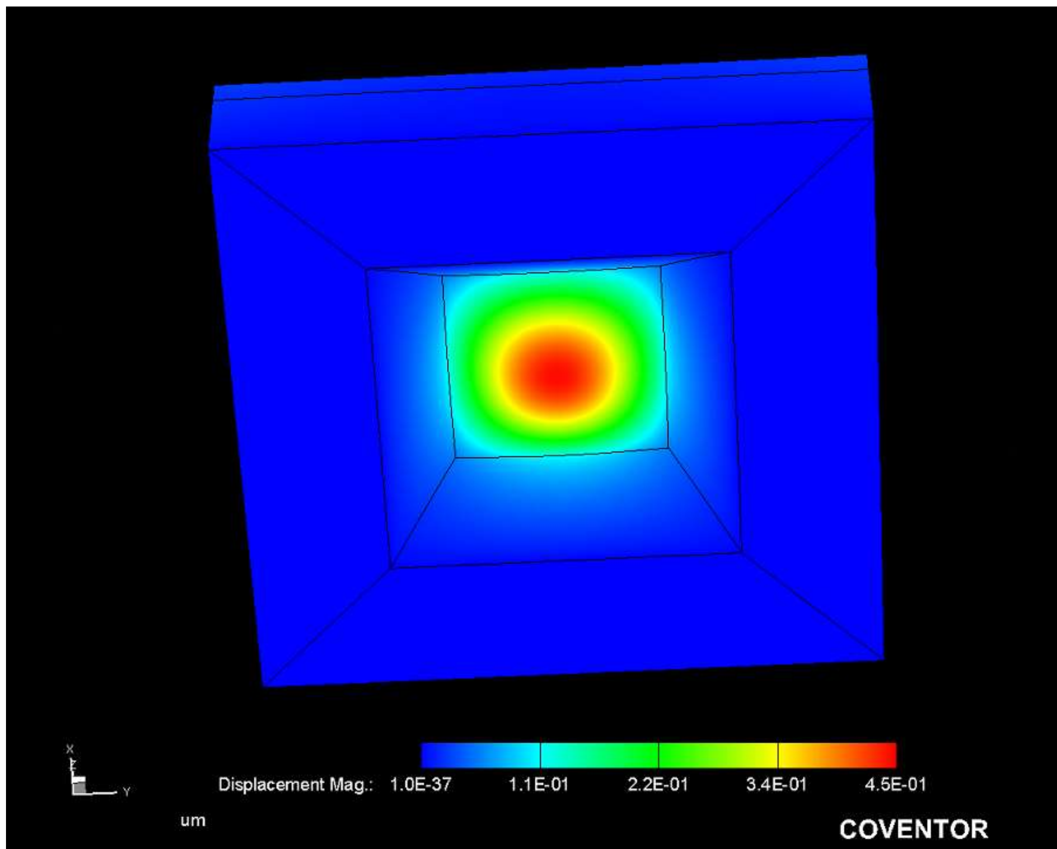

Figure 21: PoC device FEA displacement results at 1000 PSI, bottom side

A predicted von Mesis stress profile of the device is visualized in the FEA model presented below in Figure 22 and Figure 23, where stress concentrations are shown to occur at the center of the membrane edges. This behaviour is in accordance with the expected stress profile of a square membrane operating under distributed load. However, the FEA model predicts a maximum stress of 1600 MPa, compared to an estimated 100 MPa using the fixed support analytical model. This result suggests a significantly greater risk of exceeding the 3000 MPa yield strength of silicon than expected using analytical methods.

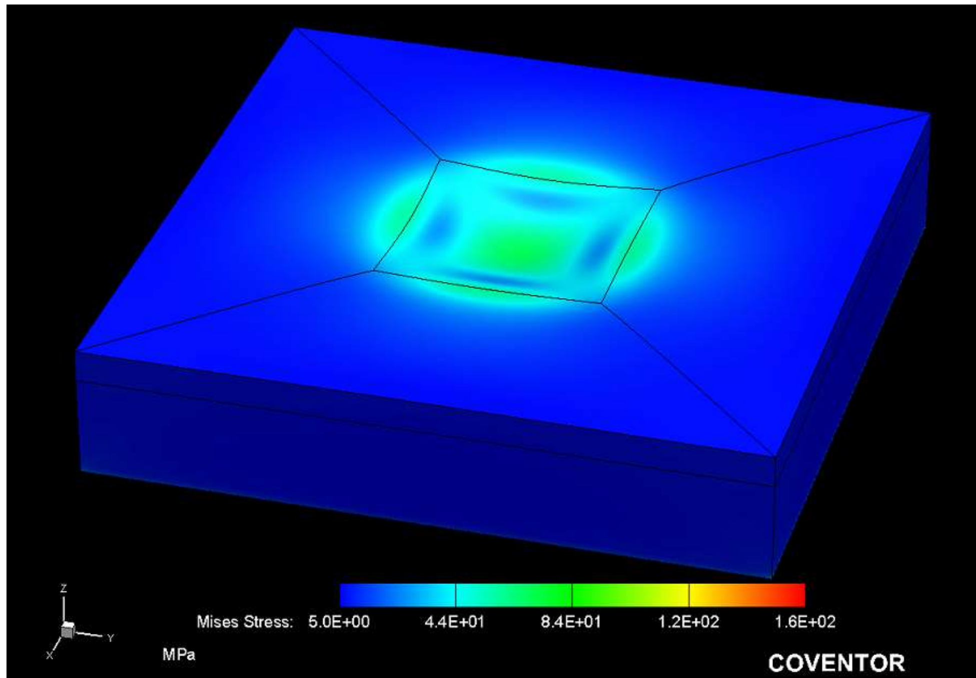

Figure 22: PoC membrane von Mises stress visualization at 1000 PSI, top side

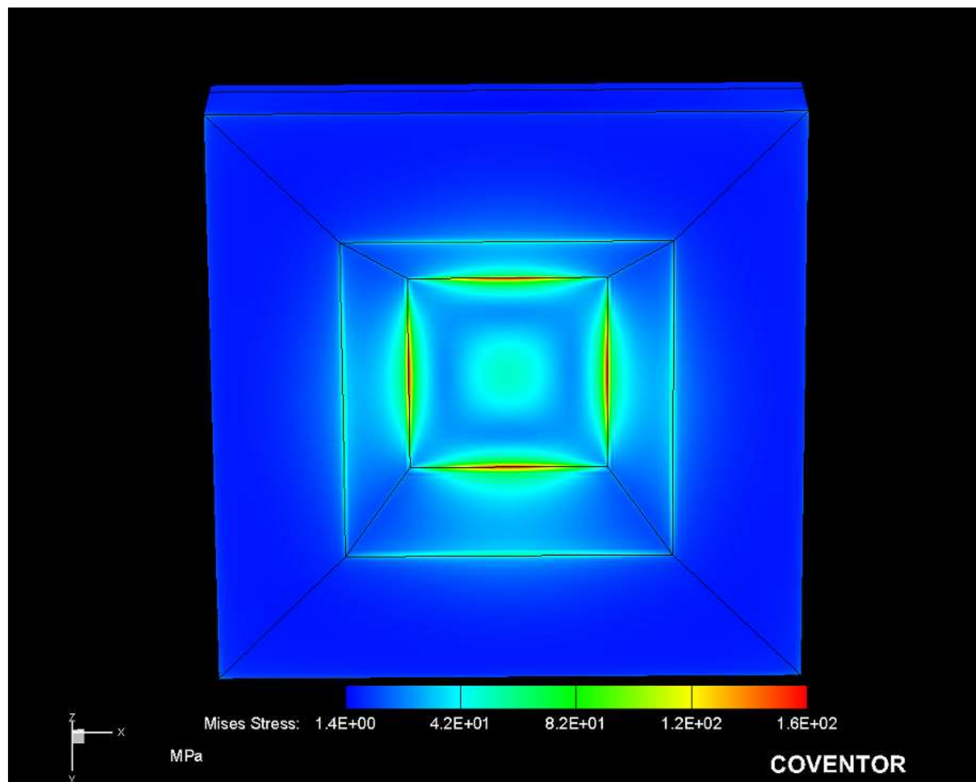

Figure 23: PoC membrane von Mises stress visualization at 1000 PSI, bottom side

The observed mismatch between the analytical and FEA models suggests that the non-ideal support behaviour will result in higher membrane stresses and deformation than analytically predicted. This will manifest in higher experimental sensitivity to pressure and earlier failure of the device than expected from the fixed support model. It is expected that membranes which are very thin relative to their support material would have reduced influence on the deformation on the supports than observed in this FEA model. Consequently, thin membranes may not encounter the non-ideal deformation to the extent presented in this work. This may explain why the low pressure membranes discussed in literature showed better agreement with the fixed support analytical model.

4.3 As-fabricated Custom SOI Inspection

Once the fabricated chips are received, they are analyzed under an optical microscope to verify the tolerance of the membrane side length and thickness, as well as examine the angle of the etching below the membrane. These parameters are critical to the operation of the sensor, as small variations in the geometry of the membrane can significantly impact its behaviour. Due to the use of DRIE (Deep Reactive Ion Etching), the etching cavity has a lofted geometry with a larger side length on the membrane side, compared to the exposed surface; this suggests that it is possible that simply measuring the opening in the exposed cavity surface is not truly representative of the membrane side length. As shown below in Figure 24 and Figure 25, the as-fabricated membrane and cavity dimensions show very little deviation from the designed values; however, due to the destructive nature of this test, only one chip was examined in this manner.

By examining the behaviour of devices designed to measure the material properties of a chip, the membrane deflection can be better predicted by using the as-fabricated material values, rather than those available from literature. Resonant cantilevers are included in order to determine the elastic modulus, as well as Vernier gauges to determine the residual stress, and a set of devices designed by Osterberg and Senturia (referred to as M-TEST) which are able to measure both parameters. The purpose of these devices and their governing equations are described in Appendix B.

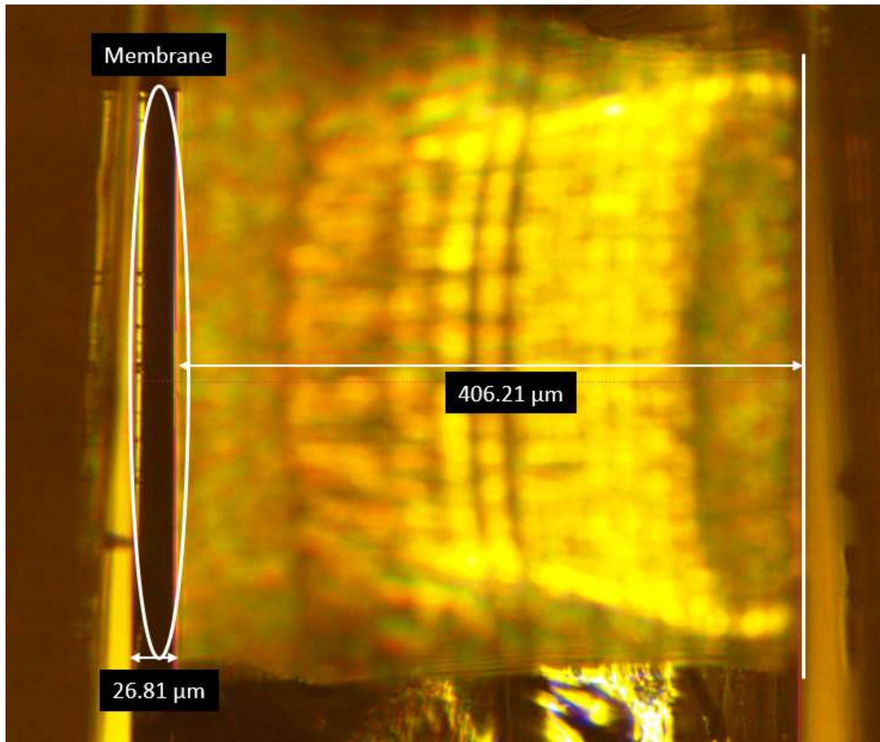

Figure 24: As-fabricated SOIMUMPs chip membrane dimensions

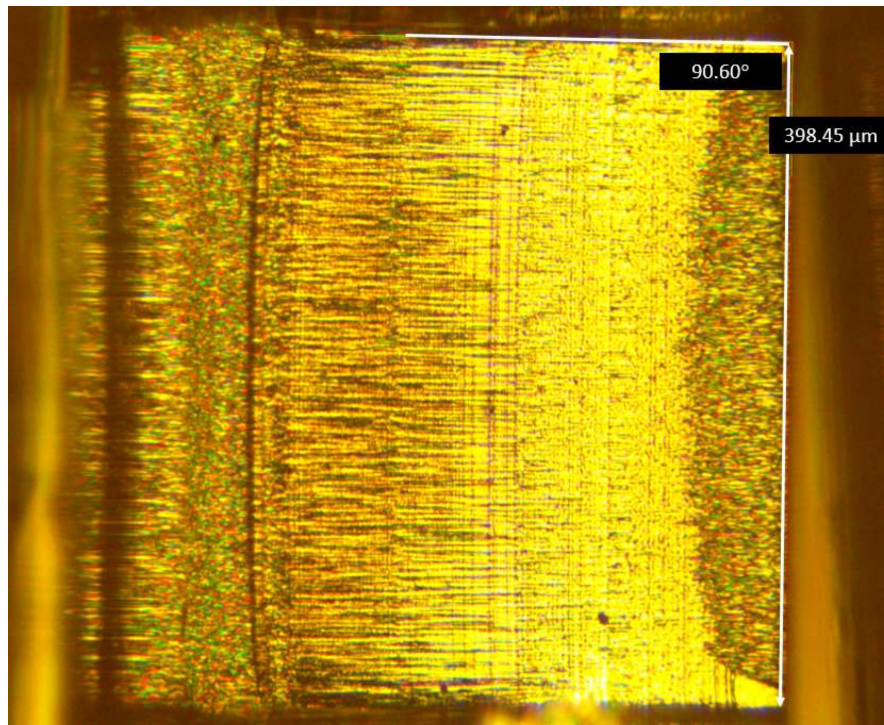

Figure 25: As-fabricated SOIMUMPs etch cavity dimensions

Chapter 5
Optical System

5.1 Optical Path

In this application, the light is directed through an optical fiber which allows for transportation through a flexible medium from the source to the membrane and finally reflected back to the detector. This permits sensitive detection components to remain separated from the harsh sensing environment, while also precluding the need for the use of transfer fluids or mediums. Light is generated at the source, which may have a narrow or broad wavelength range depending on the signal collection method used and the required fidelity. In the case of this device, a narrow band is selected to reduce signal noise during interference. Once coupled into the fiber, the light is then transmitted to the reflection cavity where the beam is first reflected by the end of the optical fiber, followed by the membrane. The beams then undergo multiple internal reflections through the etalon formed between the surface of the fiber and membrane; the resulting signal is recollected by the fiber, where the path difference results in the light reflected from the fiber interfering with the light recollected from the membrane cavity. This signal returns to the coupler to be redirected to the detector, resulting in a loss of intensity as it is divided between the source and acquisition paths. The light is then projected onto the optical signal collector (photodetector), such as a CCD (Charge-Coupled Device) or a photodiode, which detects the incident intensity. Finally, this is passed through data acquisition and processing, where demodulation of light/charge information is used to calculate deflection (and applied pressure) of the membrane. A visualization of this path is shown in Figure 26.

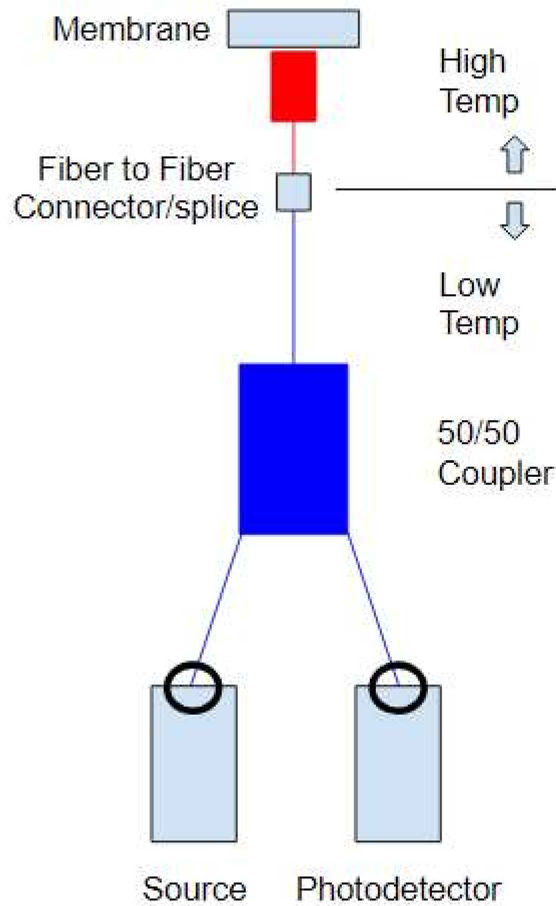

Figure 26: Optical path design

The sensing end of the fiber is stabilized through attachment of a ferrule, ensuring that the alignment and position of the tip can be predicted by providing a larger geometry for manipulation. For testing at temperatures below 85°C, a Thorlabs CFML21L10 cannula is selected. For higher temperatures, a custom connector is formed to have similar geometry to that of the Thorlabs cannula, making use of the same stainless steel ferrule component to support the fiber tip. In this way, the use and testing of a variety of combinations of adhesives and fibers can be carried out. These combinations may not be commercially available, thus expanding the possible operating range of the system. The high and low temperature variations are shown below in Figure 27. The epoxy used for assembly of the fibers is EPO-TEK 353ND, which has a maximum operating temperature of 350 ºC [36].

Figure 27: Fiber probe tip - Top: Low temperature option, Thorlabs CFML21L10 Bottom: High temperature option, Thorlabs ferrule and custom machined support

Comparing the geometry of the ferrule tip and the etched membrane cavity (as determined in Chapter 4), the minimum PoC sensor cavity length is estimated according to Figure 28, below. This yields an initial distance of 0.131mm, which decreases according to the deflection of the membrane as pressure is applied.

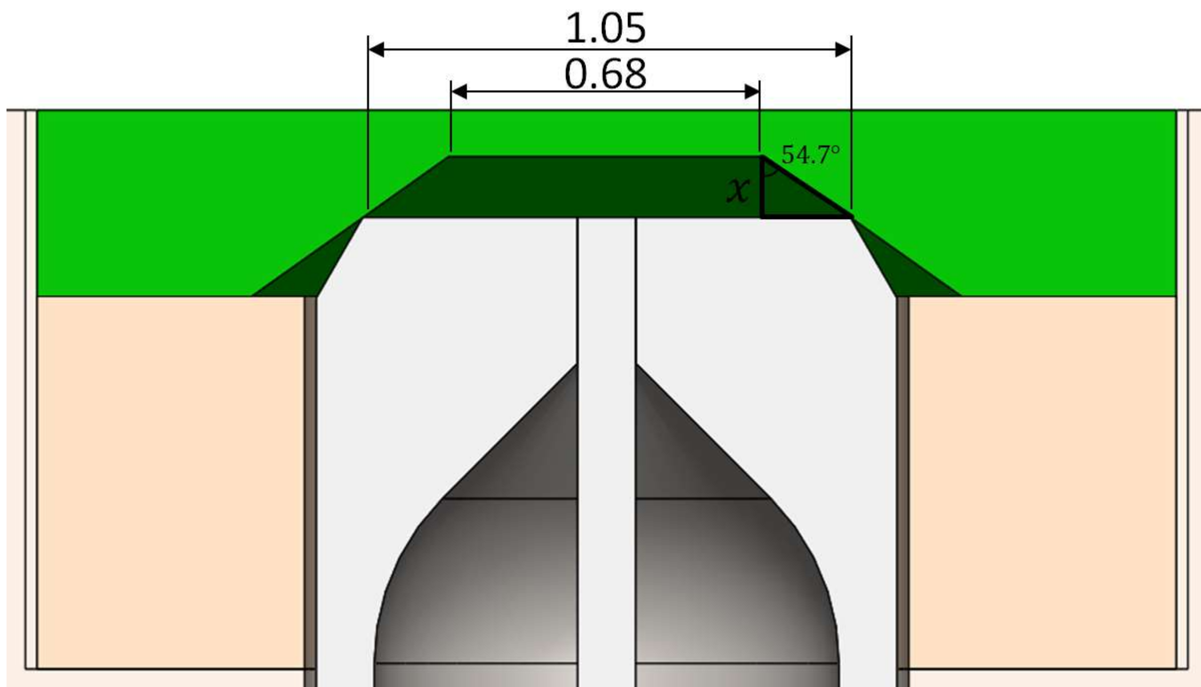

Figure 28: PoC sensor cavity size visualization

5.2 Optical Components

The optical system components are selected to provide operation both at room temperature and within harsh environment applications. An initial prototype is produced using on-hand resources available in

the lab, which is then used to inform selection of the high temperature specifications. The following parts are included in the full assembly and are detailed below:

- Optical fiber, coupled 2:1
- Ferrule for fiber support
  - SFLC127-10
    - Ø1.25 mm, 6.4 mm, Ø127 µm bore size, stainless steel
- Optical Signal Interrogator (OSI)
  - Contains photodetector and relevant electronics for signal collection
- Laser Light Emitting Diode (LED)
  - TT Electronics OPV314AT [37]
    - Total coupled power of 600 µW into a 50/125 µm fiber, tested when operating at currents of 7 mA
- SMA and ST connectors (depending on required connection for OSI and LED)

A low temperature prototype is ordered from Thorlabs using FG105LCA fibers which are formed into a 2:1 coupler; this same model is then functionalized for high temperature by splicing a length of UM22-100 optical fiber to its end and is re-terminated with a custom stainless ferrule. Specifications of the fibers used are detailed in Table VI.

Table VI: Optical fiber specification comparison [38] [39]

	FG105LCA	**UM22-100**
Core Ø (µm)	105 Silica	100 Silica
Cladding Ø (µm)	125 F-Doped silica	110 Doped silica
Coating Ø (µm)	250 Acrylate	124 Polyimide
Max Operating Temp (°C)	85	300
Numerical Aperture	0.22	0.22
Wavelengths (nm)	400-2400	180 to 850

The optical fiber's numerical aperture is used to calculate the angle of acceptance according to Equation 16, resulting in an acceptance angle of ~12.7° for both of the fibers used in this work [40].

This value represents the maximum incident angle of light which will be transmitted through the fiber and determines the resulting dot size. As a result, cone of acceptance is produced with a limit angle equal to the arcsine of the fiber's numerical aperture.

$$NA = \frac{1}{n_o} \sqrt{n_{core}^2 - n_{cladding}^2} = \sin(\theta_{acc}) \quad (16)$$

Where: NA is the numerical aperture of the fiber, n_o is the refractive index of the surrounding medium, n_{core} is the refractive index of the fiber core, $n_{cladding}$ is the refractive index of the fiber cladding and θ_{acc} is the resulting acceptance angle of the fiber.

The dot size of the transmitted light is determined by the angle of acceptance. With a large dot size, an averaging effect is expected to occur to the reading where a significant quantity of light is reflected from portions of the membrane experiencing relatively low deflection. Consequently, improved resolution is achieved through the use of a smaller dot which is able to optimally interrogate only the high deflection portion. In addition, reflected rays near the edge of the dot are not able to be collected due to geometric constraints. This results in a radius of collected light that is returned to the fiber, which is a function of cavity distance and acceptance angle, as shown in Figure 29. However, the intensity over the dot profile is not consistent in multimode fibers; this precludes the ability to predict the intensity loss due to uncollected rays, unless the intensity profile can be characterized.

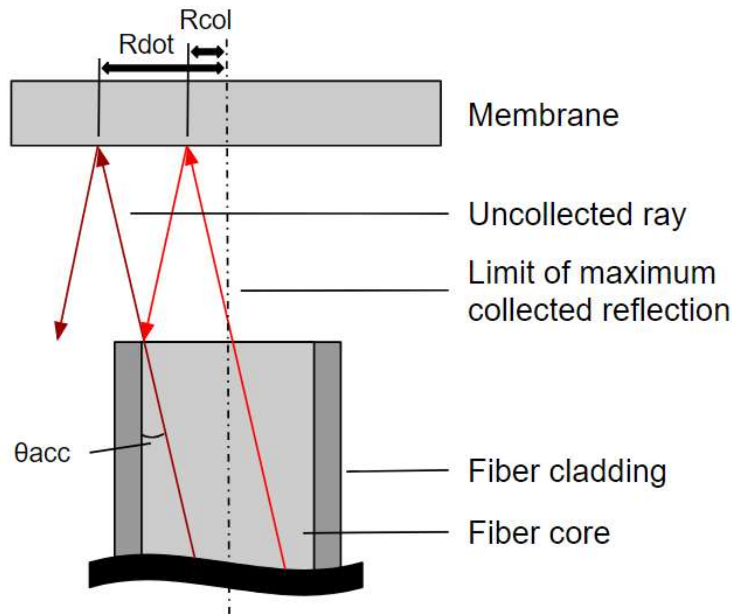

Figure 29: Visualization of maximum collected reflection radius

The OSI (Optical Signal Interrogator) consists of a light source, a photodetector, pertinent electronics and an Arduino to demodulate the signal. This device is described in [41] and is calibrated and customized to provide optimized response at the required interrogation wavelength (~ 850 nm). This device is integrated with the TT electronics OPF480 photodetector, featuring a responsivity of 0.55 A/W at an operating voltage of 5.0V and 80 degree field of view, when collected using a 50/125 μm fiber and wavelength of 850nm [42].

Functionality testing is carried out on the optical system as follows, to verify it is operating as expected:

1. Using a flashlight, pass light through the end of the connector – it should be visible at the other end of the optical fiber
    a. Should be repeated for all three prongs of the assembly, to verify optical integrity
2. Test probe reflection against mirror with source and photodetector – ensure probe is orthogonal to the surface
    a. Expect signal response of approximately 300 to 500 mV
3. Repeat mirror test with loose silicon membrane (not epoxied into housing), again ensure probe is orthogonal to membrane surface
    a. Expect signal response of approximately 80 to 150 mV

Chapter 6
Packaging and Thermal Impact on Sensor Response

6.1 Packaging

In order to support the sensor die, a stainless-steel housing is designed which integrates into MorHeat's existing equipment. This housing (shown below in Figure 30) provides a robust packaging for securing the location and alignment of the sensor components, ensuring that a reliable signal is obtained from the sensor. A tight-fitting seat is used to locate the die and secured with the same EPO-TEK 353 epoxy used to assemble the optical fibers. This geometry is designed to arrest any movement of the die with respect to the tip of the fiber, as the accurate prediction of the location and cavity distance is critical to sensor's operation. The housing also includes MorHeat's proprietary 45° chamfer seal to ensure the fluid under test is adequately contained without leakage. Fabrication drawings for this component are available in Appendix E.

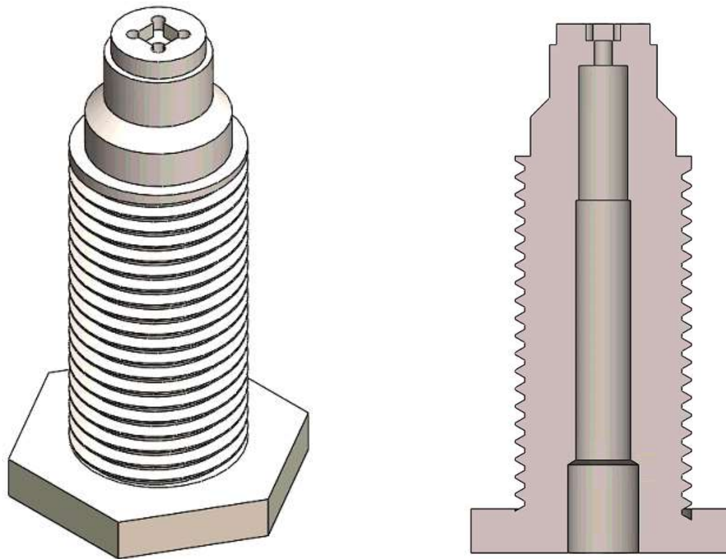

Figure 30: Housing component – Left: Isometric view Right: Cross-sectional view

The fiber tip is secured in the housing using a fiber locator, which mechanically positions the ferrule and eliminates additional space in the cavity by forcing the ferrule to be fully inserted in the housing. This locating component (shown in Figure 32) is threaded into the back-side of the housing and features a slot permitting the fiber to pass through; the full assembly is shown in Figure 31. Manufacturing drawings for the fiber locator can be found in Appendix F.

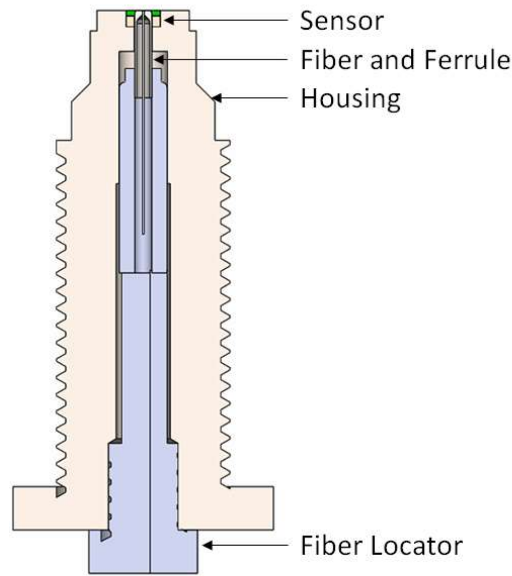

Figure 31: Packaging assembly cross-section view

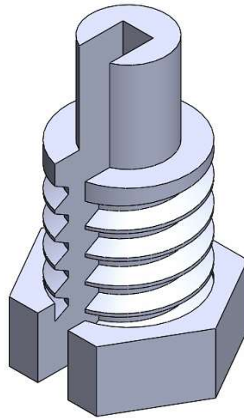

Figure 32: Fiber locator - Isometric view

A gas vent must be provided on the reverse side of the membrane in order to permit gases to escape into the ambient environment as temperature increases in the system; if this is not provided, these gases will pressurize in the FP cavity, resisting deflection of the membrane, which would need to be compensated for in the demodulation of sensor data to ensure results are not compromised [29].

Although it is not viable for harsh environments, Xu et al. (2012) present a nanothick silver membrane which yielded a very high sensitivity of 70.5nm/kPa over a pressure range of 0-50 kPa using a ceramic ferrule and silver-ammonia plating fabrication [43]. Two sources of temperature error are identified: thermal expansion of the sensor and pressure changes due to expansion of the gas

trapped inside the cavity. It is estimated that the observed thermal error is primarily due to this trapped gas, as thermal expansion accounted for 8% of the calculated cavity changes. However, no analytical model is provided to compare and this does not consider the deformation of the membrane during its expansion, or the softening of the materials. Reducing the cavity length is expected to reduce the sensitivity to changes in temperature.

6.1.1 Failure Condition - Thread Shearing

The primary expected failure condition of the housing is high pressures resulting in shearing of the insertion threads. Failure stress is predicted using the internal thread strength formula given by Equation 17 [44].

$$F = S_u A_{ts} \tag{17}$$

Where F is the force applied to the threads, given by the product of pressure and area, S_u is shear strength of the tapped material which is defined as $0.5\sigma_{yield}$, where $\sigma_{yield-304SS} = 215$ MPa [45]

In this case, the sheared material is the section of threading that overlaps between the insertion threads of the housing and the internal threads of the pressure chamber. This is defined as in Equation 18 and the terminology is visualized in Figure 33.

$$A_{ts} = \pi n L_e D_{smin}\left[\frac{1}{2n} + 0.57735\,(D_{smin} - E_{nmax})\right] \tag{18}$$

$$A_{ts} = cross - sectional\ area\ of\ sheared\ material$$
$$Where:$$
$$n = Number\ of\ threads\ per\ inch = 20$$
$$L_e = Length\ of\ thread\ engagement = 1"$$
$$D_{smin} = minimum\ major\ diameter\ of\ external\ threads = 0.46"$$
$$E_{nmax} = maximum\ pitch\ diameter\ of\ internal\ threads = \frac{0.49" + 0.45"}{2} = 0.47"$$

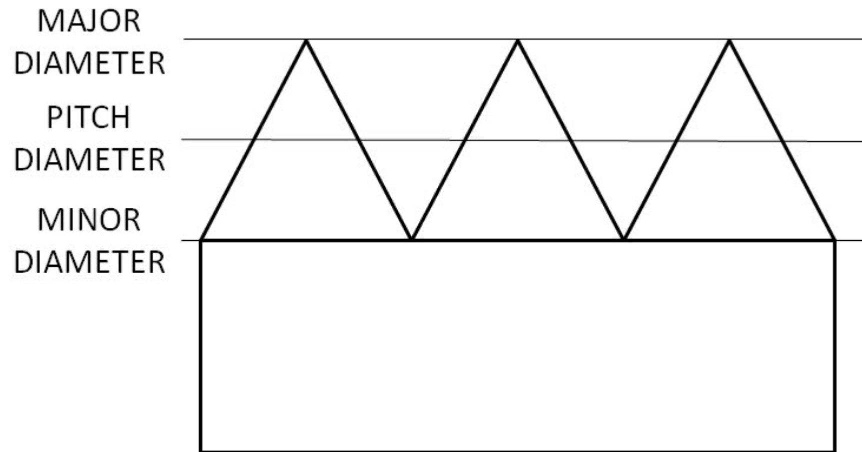

Figure 33: Thread diameter terminology visualization

Through rearranging the internal thread strength formula and substituting values for the system geometry, the maximum applied pressure for failure is calculated as shown in Equations 19 and 20.

$$P_{failure}A_{exposed} = S_u A_{ts} \tag{19}$$

$$P_{failure} = \frac{0.5\sigma_{yield}A_{ts}}{\pi r_{housing}^2} = 14774\ PSI \tag{20}$$

6.2 Full System Functionality Testing

Once the system is fully assembled, the basic functionality is tested before exposure to high pressures. This process is to verify that reflection signals are being properly collected and that damage does not occur to the device when full scale testing begins, such as contamination of the membrane or fiber due to leakage.

1. Reflection test off assembled membrane, using the same technique as the optical system reflection test but instead insert the fiber into the housing with epoxied die to ensure it is able to collect a reflected signal
    a. Expect response in the range of 80 to 150 mV
2. Air pressure testing up to 90 PSI, with Teflon tape. Primary goal is to identify leaking through the membrane and a small intensity response to pressure
    a. If air is leaking through the threads, apply more Teflon tape to isolate the membrane cavity

b. If leaking occurs through the membrane cavity, more adhesive must be applied

   i. This can be identified by removing the optical fiber and covering the opening in the back of the housing where the fiber is inserted. If there is an audible change due to any escaping air, the adhesive has not created a good seal around the membrane. A completely sealed membrane can also be verified through visual inspection, as shown below in Figure 34.

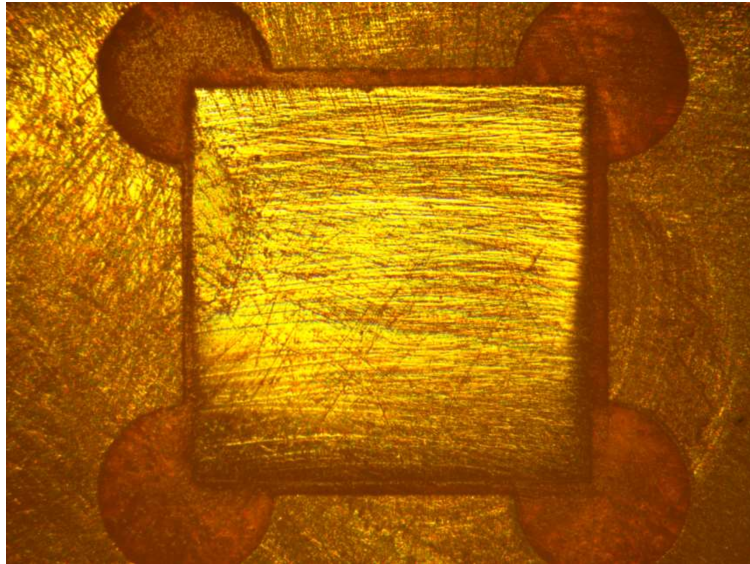

Figure 34: Membrane and adhesive integrity verification

3. Oil pressure testing up to 200 PSI, without Teflon tape. Primary goal is to identify leaking through the threads and a small intensity response to pressure.

   a. If oil leaks through the threads, ensure that the housing is securely tightened into the testing chamber. In the case that leaking persists, verify the housing geometry against the manufacturing drawing and that no burrs are present which may prevent the 45° chamfer from sealing.

6.3 Temperature Dependence of Material Properties

Through integrating values and relationships acquired from literature into the above relationships, the impact of temperature-dependence on material properties is compensated in the sensor behaviour. This aberration is apparent in both the mechanical and optical properties of the constituent materials,

which can result in significant errors in the acquired pressure data of the sensing elements and must be accounted for in order to produce a device capable of high accuracy.

6.3.1 Silicon Membrane

As the primary component of the sensor involved in data collection from the medium, accurate approximations of the membrane properties are critical to the functionality of the device. Due to the asymmetry of the crystal structure, single crystal silicon structures have an anisotropic elastic modulus. As such, the elastic response of such a material depends on the direction of applied stress to the structure – with each major crystallographic direction responding with a different elastic modulus. However, in the case of a membrane loading is not applied in a single crystal direction, so an averaged elastic modulus is used to predict the deflection behaviour to an applied stress. This averaged elastic modulus as a function of temperature as shown in Equation 21 [34]:

$$E(T) = 167.98x10^{9} - 1.167x10^{7}T + 1757.9T^{2}[Pa] \quad (21)$$

$$25°C \leq T \leq 600°C$$

This equation yields calculated values of 167.7 GPa and 161.6GPa at 25 and 600°C, respectively – resulting in an estimated 3.6% decrease in the elastic modulus at elevated temperatures. These values are compared to those acquired by Tsuchiya, where the averaged Young's modulus was determined to be 163.2 GPa at room temperature and 151.8 GPa at 600°C, resulting in a decrease of 7.0% compared to room temperature [35]. Although this presents a lower overall elastic modulus, the trend and magnitude of decrease is similar. Hopcroft describes how silicon crystal experiences uniform thermal expansion and changes in elasticity in all directions; using values from previous works, temperature coefficient of elasticity is calculated to be -64 ppm/°C at 25°C and -75 ppm/°C 125°C [33].

Limited information is available in literature on the impact of temperature on the index of refraction of silicon, but some studies have been completed by Vuye at a wavelength of 830nm. Their experimental results are summarized below in Table VII, where a percentage change of 1.77% is observed between 20 and 300°C.

Table VII: Refractive index of silicon at 830nm, as a function of temperature [46]

Temperature (°C)	Refractive index
20	3.678

100	3.695
150	3.709
200	3.721
250	3.731
300	3.743

By graphing the relationship between wavelength and index of refraction, as shown below in Figure 35, it is observed that there is a significant reduction in the apparent slope at high wavelengths. As such, the available behaviour data of silicon at 830nm is taken to be a close approximation of that at 850nm, which will be used for the correction of acquired sensor response.

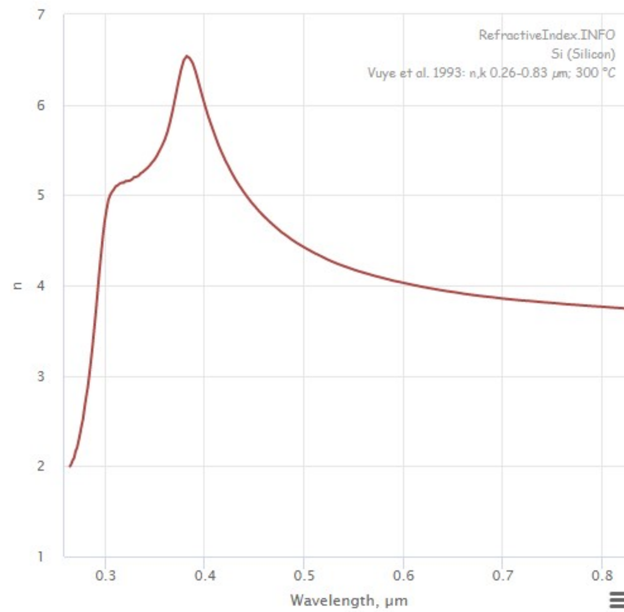

Figure 35: Silicon refractive index with respect to wavelength at 300°C [47]

Finally, the thermal expansion coefficient of single crystal is examined. Again, there is limited data available for the dependence of this property on temperature, but an expression is available for the response in the <110> and <111> directions, as given in Equation 22 [48]

$$\alpha(T) = -5.35x10^{-6}e^{-6.83x10^{-4}T} + 7.81x10^{-6} \quad (22)$$

$$0°C \leq T \leq 600°C$$

6.3.2 Silicon Dioxide

Silicon dioxide, or silica, acts as both the main material of the optical fiber and insulating layer of the custom SOI membrane in this system - non-crystalline, fused silica is used as the primary material for optical fibers and MEMS applications; crystalline silicon dioxide is referred to as quartz. As such, any variance in the index of refraction of this material will have a significant impact on the behaviour of the sensor through changes in the reflection behaviour of the Fabry-Perot cavity. The refractive index of fused silica operating at 850 nm is 1.4525 at 20°C, but temperature-dependent data of its behaviour is not available in literature [49]. As such, the closest available reference (633nm) is examined as a function of temperature per Equation 23, with temperature given in Kelvin [50]. Calculated values yield that the refractive index varies from 1.473 at 20°C to 1.477 at 300°C, for a percentage change of 0.13% - significantly less than that of silicon.

$$n = 1.47269 + 7.09780x10^{-6}T \tag{23}$$

Unlike silicon, the elastic modulus of silica increases with rising temperature. This trend is predicted according to Equation 24, from -50 to 1000°C [51]. These findings are corroborated by [52], which states that elastic modulus increases with temperature until a maximum occurs at 1175°C. Substituting a room temperature value of 73 GPa into Equation 24, yields an increase to 74.47GPa at 300°C, resulting in a relative change of 2% [52], [53].

$$Relative\ elastic\ modulus\ ratio = \left(\frac{E}{E_o}\right) = 1 + 6.7x10^{-5}\Delta T \tag{24}$$

$$Where\ \Delta T = T - 25°C$$

The observed thermal expansion coefficient of silica is constant at 0.5μm/°C from 25 to 1000°C [54]. The continuous random network observed in vitreous (glass-like) silica results in low thermal expansion, as changes of volume must result from changes in silicon-oxygen distance. However, due to the high strength of the oxide, any changes that do occur will be small.

6.4 Thermal Expansion of Components

6.4.1 Analytical Position Error Due to Packaging

As the components expand due to a rise in temperature, a compounding position error will occur based on the geometry of the system. Due to the high sensitivity of optical systems, it is critical to account for this aberration, as displacements on the order of nanometers can significantly impact the signal response; the components considered are shown below in Figure 36 and Figure 37.

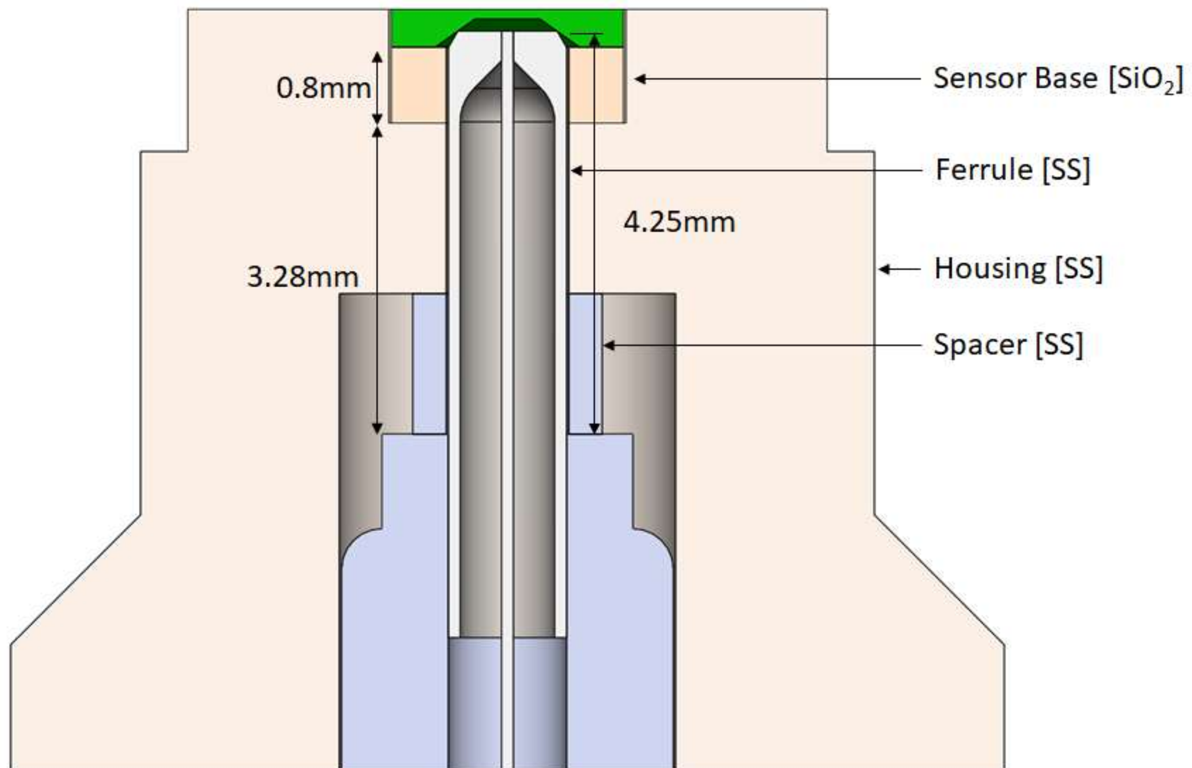

Figure 36: PoC thermal expansion component visualization

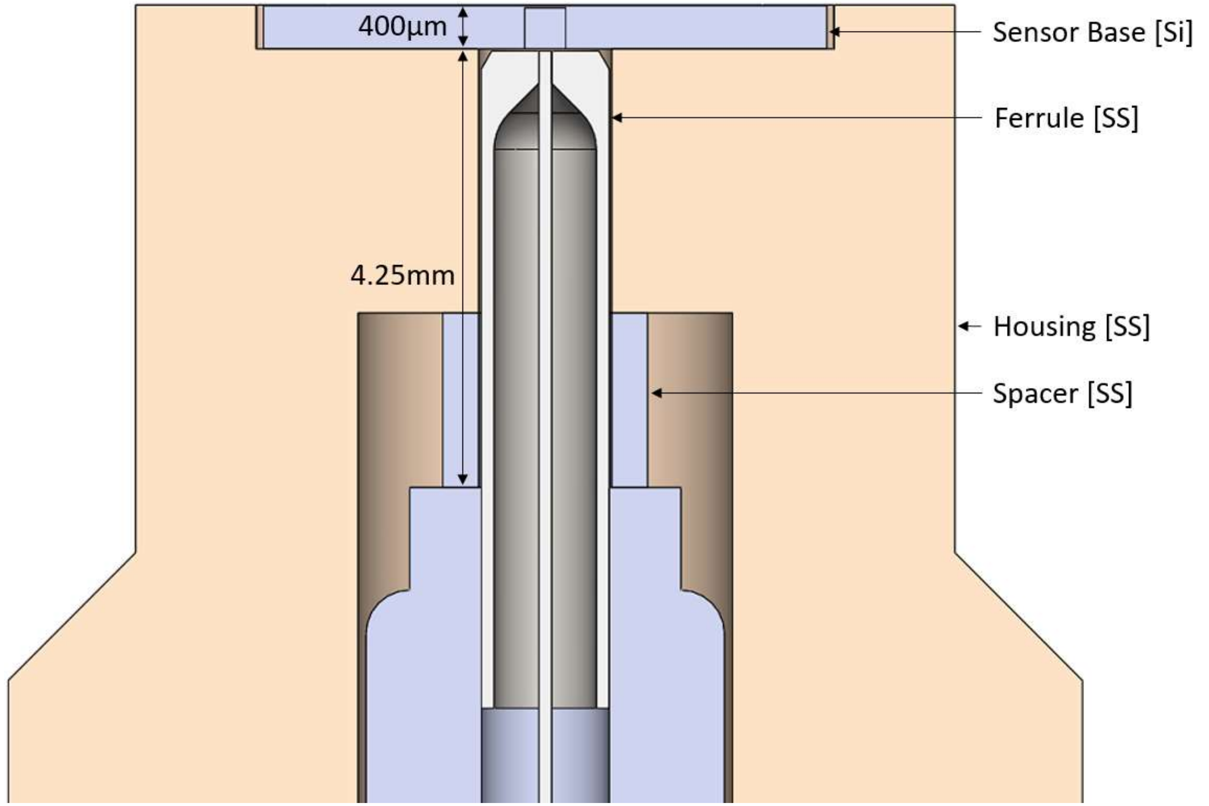

Figure 37: SOI thermal expansion component visualization

Thermal strain is used to approximate these dimensional changes, developed in Equations 25-29; this assumes that no friction is present and that the fiber is anchored at single point to the packaging. In this calculation, a positive displacement indicates reduction in cavity size. The thermal expansion coefficients for silica and silicon are estimated according to the expressions from Section 5.2, and that of stainless steel is shown below in Table VIII.

$$\varepsilon_{th} = \frac{\Delta L_{th}}{L_o} = \Delta T \alpha \tag{25}$$

$$\Delta L_{th} = \Delta T \alpha L_o \tag{26}$$

$$\Delta L_{PoC} = \left| \alpha_{SS}(L_{ferrule} - L_{housing} - L_{spacer}) - \alpha_{SiO_2} L_{oxide} \right| \Delta T \tag{27}$$

$$\Delta L_{SOI} = \left| \alpha_{SS}(L_{ferrule} - L_{housing} - L_{spacer}) - \alpha_{Si} L_{handle} - \alpha_{SiO_2} L_{oxide} \right| \Delta T \tag{28}$$

$$\Delta T = T_{operational} - T_{curing} = 300 - 20\ ^{\circ}C \tag{29}$$

Table VIII: 304 SS coefficient of thermal expansion as a function of temperature [45]

Temperature [°C]	Coefficient of Thermal Expansion [μm/m°C]
20	17.3
250	17.8
500	18.7

The overall analytical thermal impact on sensor response is quantified by combining the contributions from material property temperature dependence and thermal expansion. The resulting thermal impact on the path difference is determined by the superposition of the membrane deflection (Equation 7) with the thermal expansion deflection (Equations 27 and 28 – for the PoC and SOI membranes, respectively), where the material properties are taken as functions of temperature as defined in Section 6.3. The maximum displacement experienced by the membrane at 1000 PSI and 300 ºC is visualized for the PoC and 400μm SOI designs in Figure 38 and Figure 39, respectively. In both the PoC and 400μm SOI cases, the impact of thermal expansion is shown to cause significant aberrations. This causes changes in the expected cavity distance by 1 and 0.4 times the wavelength, respectively. It is observed that the impact of material property changes with temperature are negligible compared to thermal expansion displacement on the cavity distance. However, the change of material properties will impact the sensitivity of the sensors through softening of the elastic modulus and small changes to the refractive indices. Detailed visualization of the temperature influence on the metrics discussed in Section 4.2 can be found in Appendix D.

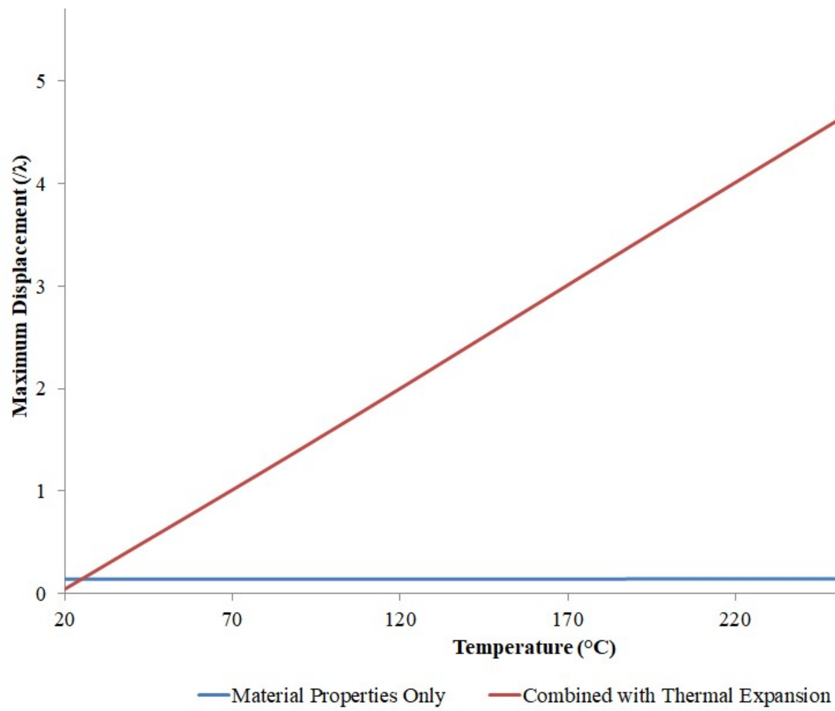

Figure 38: 1000 PSI PoC maximum displacement dependence on Temperature

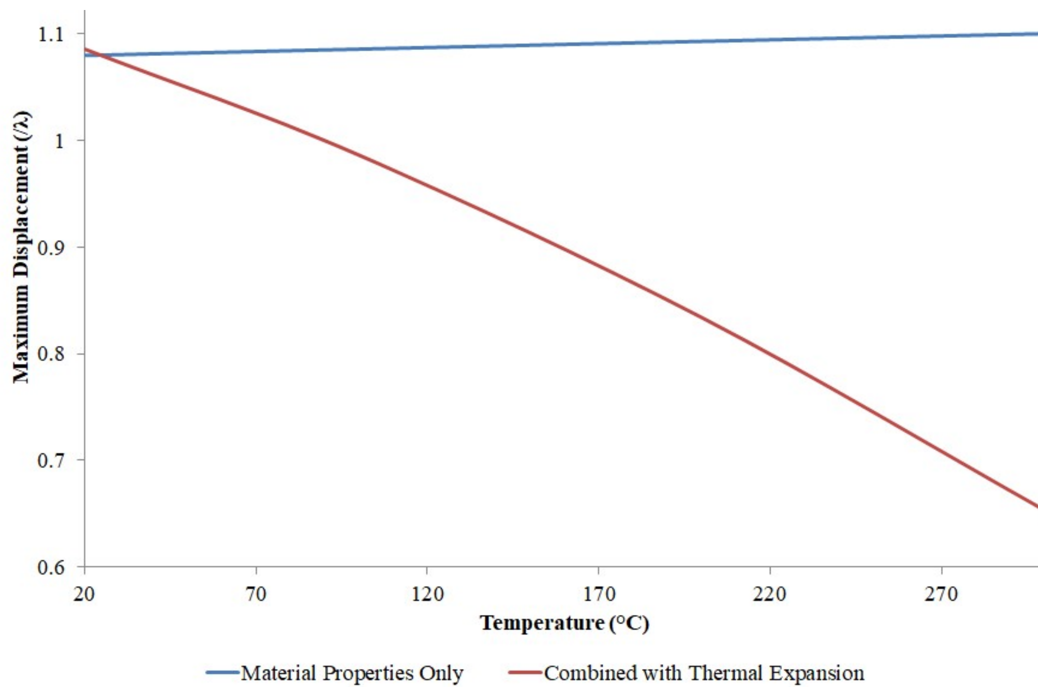

Figure 39: 1000 PSI 400 µm SOI maximum displacement dependence on Temperature

6.4.2 Device Expansion

Building on the finite element model developed in Section 4.2.2, the impact of thermal expansion on the PoC membrane behaviour is examined. First, the device is simulated without applied pressure at 100°C to investigate the impact of temperature on the resulting shape and how it might affect the stimulus response. Figure 40 and Figure 41 show that as temperature increases, the chip will expand upwards and outwards from the fixed base of the support. It is shown that the membrane will deform significantly away from the probe tip and bulges above the chip surface. This will result in stretching of the membrane, thus increasing its effective elastic modulus and decreasing the deflection response to pressure. In addition, the deflection induced by this expansion sets a bias on the initial position that compounds with the thermal expansion of the housing to modify the position of the tip of the probe relative to the membrane. Maximum deflection at the center of the unloaded membrane is calculated to be 0.32 μm, causing a collected intensity signal phase change of ~1 radian compared to the room temperature condition.

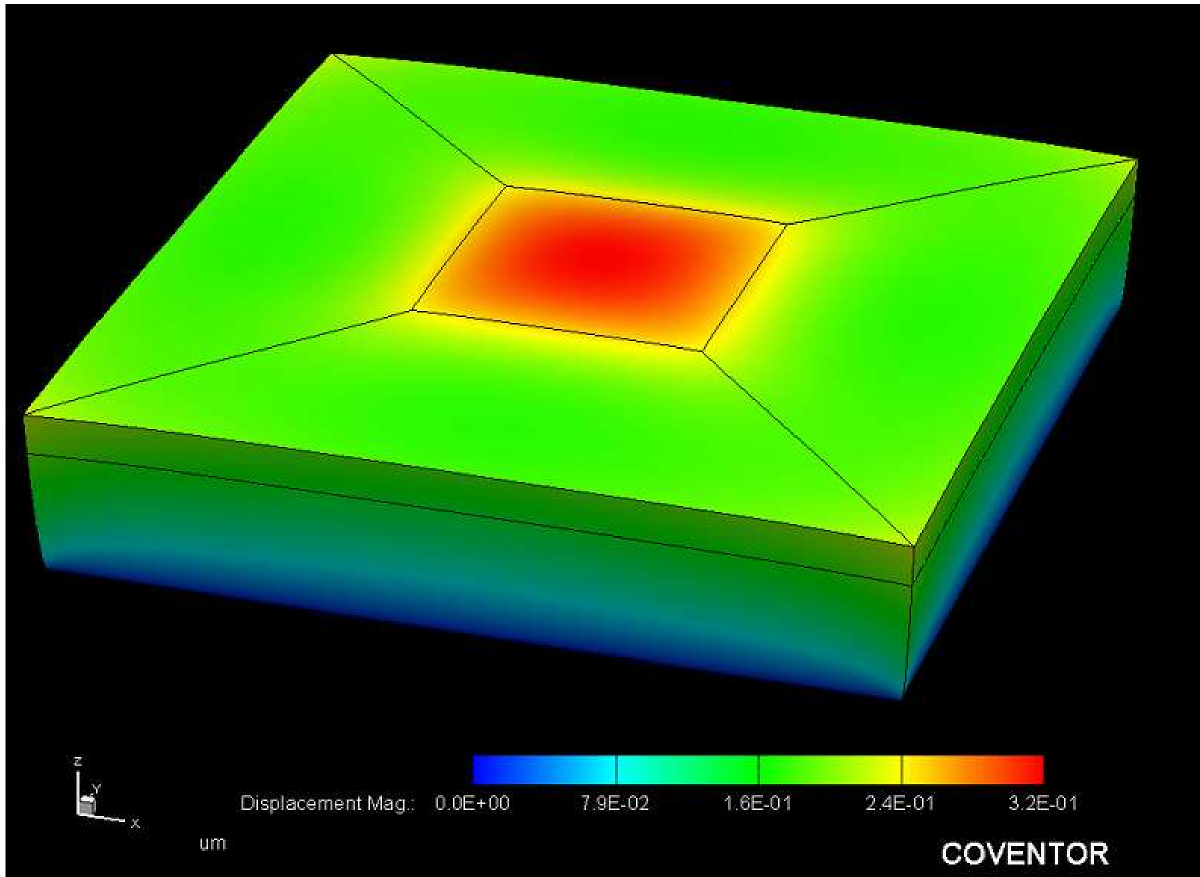

Figure 40: PoC FEA no applied pressure, 100°C – isometric view

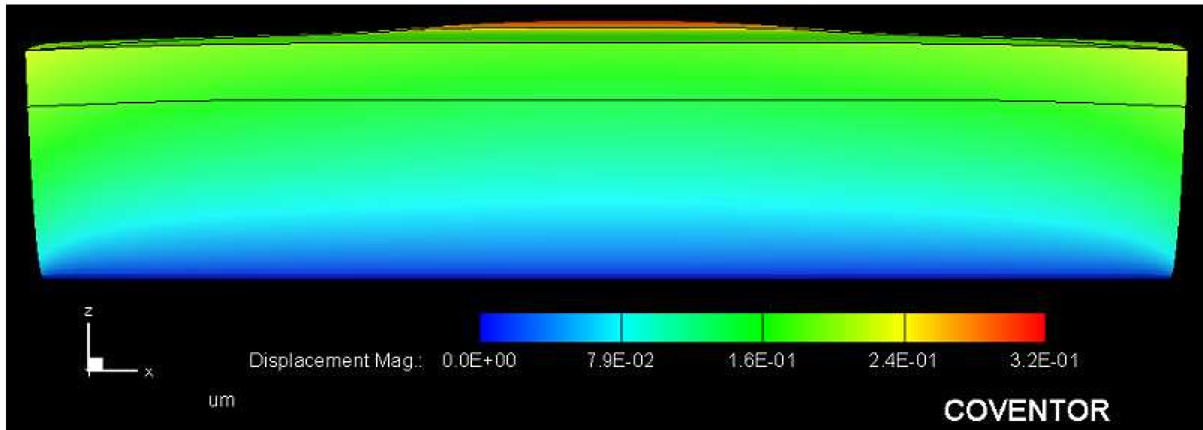

Figure 41: PoC FEA no applied pressure, 100°C - side view

The temperature and mechanical models are combined to determine the interaction of temperature and pressure on the PoC membrane at 100°C and 1000 PSI. In Figure 42 and Figure 43, the predicted maximum displacement is shown to be 0.11 μm at the center of the membrane, which is significantly lower than the 0.4477 predicted by the mechanical model. This displacement does not directly correlate to the phase change of the reflected light, due to the deformation of the supporting structure. The edges of the membrane are elevated away from the base of the chip, which will further offset the phase of the reflected intensity. This combination of deformation and membrane stretching results in significantly lower deflection that that predicted by the ideal analytical model of the sensor behaviour.

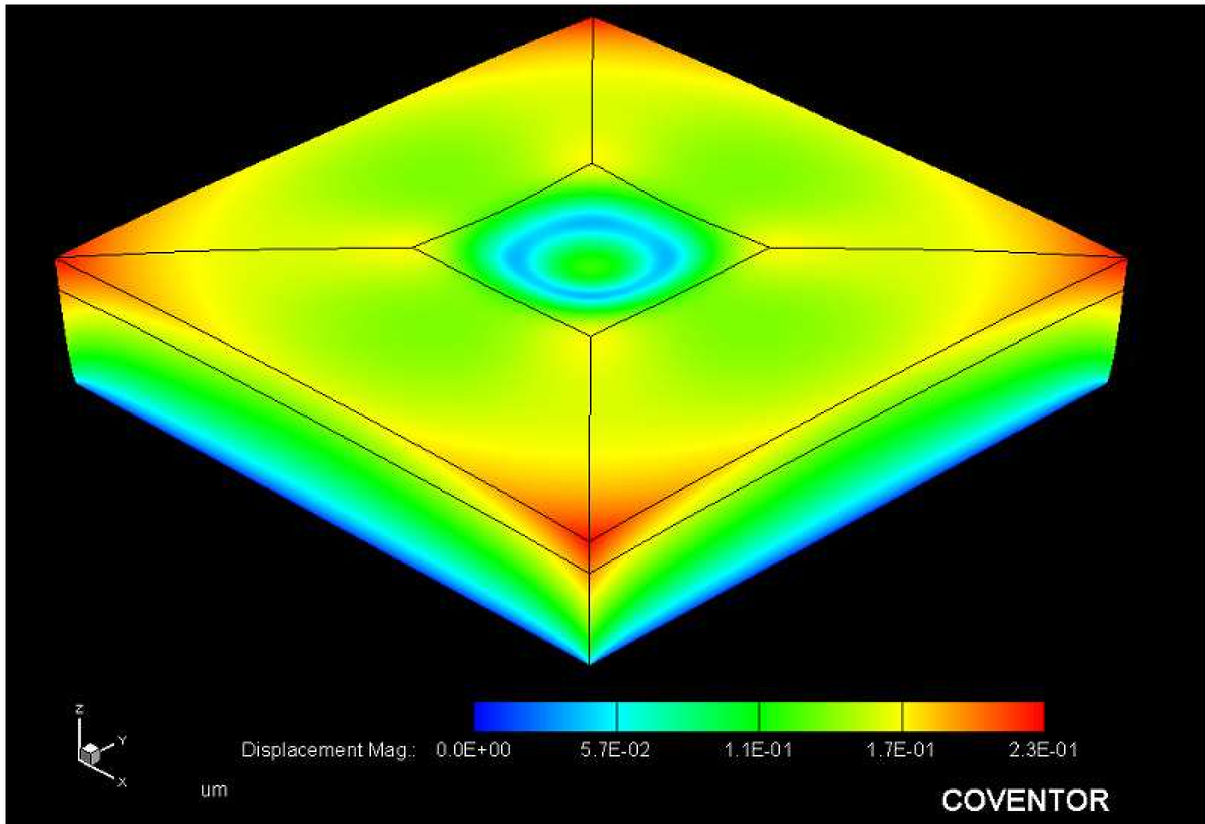

Figure 42: PoC FEA 1000 PSI 100°C - isometric view

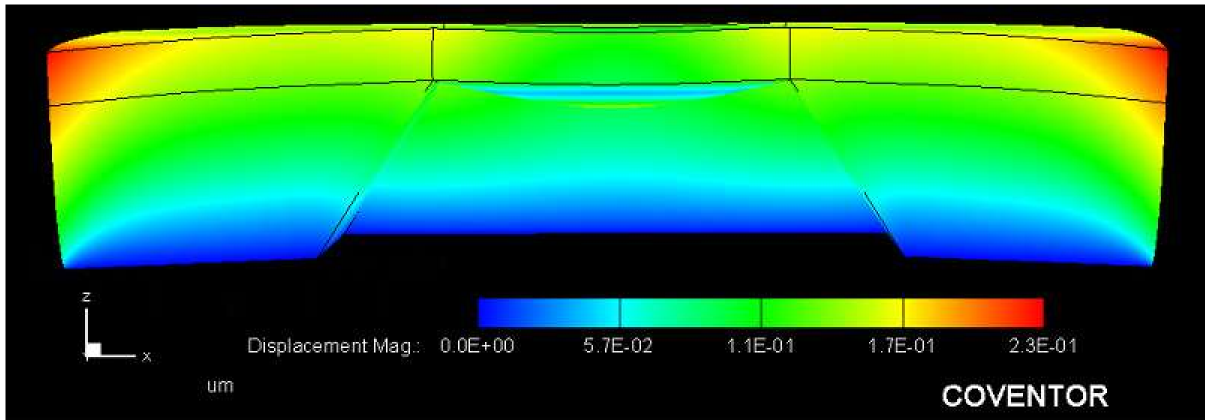

Figure 43: PoC FEA 1000 PSI 100°C – cross-sectional side view

Chapter 7
Experimental Results, Validation and Discussion

Experiments are carried out in the SIMS lab using a combination of standard lab equipment and a calibrator provided by our industrial partner. The average ambient conditions are measured to be 21°C, 15% humidity. The full experimental set-up is shown below in Figure 44. Throughout testing, it was found that small variations in the radius of the optical fiber would significantly impact the signal received by the system. As such, electrical tape is used to steady the optical fiber and electrical components in order to minimize vibrations, as shown in Figure 45. Radiuses of curvature in the optical line should be eliminated wherever possible and any bends that are required should be as gentle geometry permits. Voltage is supplied to the LED by the DC source through an electrical breadboard. A pressure and temperature calibration machine is provided by MorHeat, which contains a silicon hydraulic oil to apply pressure to the membrane through the threaded housing interface. A digital pressure gauge provides feedback of the currently applied pressure. This system is secured with anti-rotation clamp to arrest the movement of the calibration machine during application of pressure, to minimize vibration which can lead to error in the sensor response. As this device is implemented in an industrial system, a high amount of vibration in the system will need to be avoided or accommodated for. One option is damping the vibration though epoxying the optical probe into the packaging to ensure minimal relative movement. However, deformation may still occur in the mechanical structure of the probe or epoxy during vibration. Alternatively, pneumatic or active vibration damping could be used, but would need to be implemented in a manner as to not impact the pressure data acquisition. Further development will be required to isolate vibration in future stages of this project. Temperature is controlled by an external monitoring unit which provides resistance-heating directly to the housing interface. The experimental procedure is carried out as follows:

1. The optical line is connected to the LED and OSI, MatLab is set to collect the signal output and display the intensity response graph.
2. The LED is powered on using the DC source, setting the output limits to provide 1.994 V and 0.01Amps DC and allowed 30 minutes to warm up before experimental data is collected
3. Verify the integrity of the optical line by aiming the probe at a mirror, it is expected to collect a signal on the order of 200 to 300 mV.

4. Assemble the stainless steel housing with the calibration machine by threading it into the testing port. It is critical that this is tightened securely to ensure there is no leaking. Apply 200 PSI of pressure to verify that the seal is working correctly, retighten the housing if any oil escapes though the testing port. Return the pressure to 0 once the housing is sealed.

5. The device under test is fitted with the optical probe by insertion into the opening of the housing and referencing the MatLab output to see an increase in the reflected intensity, indicating that the signal is being collected by the probe. Once the probe is in position, apply 200 PSI of pressure to verify intensity response in the MatLab output. If no response is observed, this may indicate that the probe is not correctly inserted or there is a contaminant present on the surface of the membrane or probe tip. Return the pressure to 0 once completed.

    a. A small stainless steel spacer can be inserted with the optical probe to minimize risk of puncturing the membrane, so long that it does not negatively impact the signal integrity. If it is included, the probe is lightly inserted into the housing before it is tightened down and then the probe pushed into position once the housing is correctly sealed.

6. If elevated temperature is to be used in the test, the temperature control unit is turned on and set to the desired temperature. Once the readout indicates the correct temperature, refer to the MatLab output to verify that the intensity response is stabilized; this may take some time for the temperature to equalize.

7. Verify that the anti-rotation clamp is correctly in place; it should not allow the calibration machine to tilt or move when pressure is applied. The system is now ready for experimental testing.

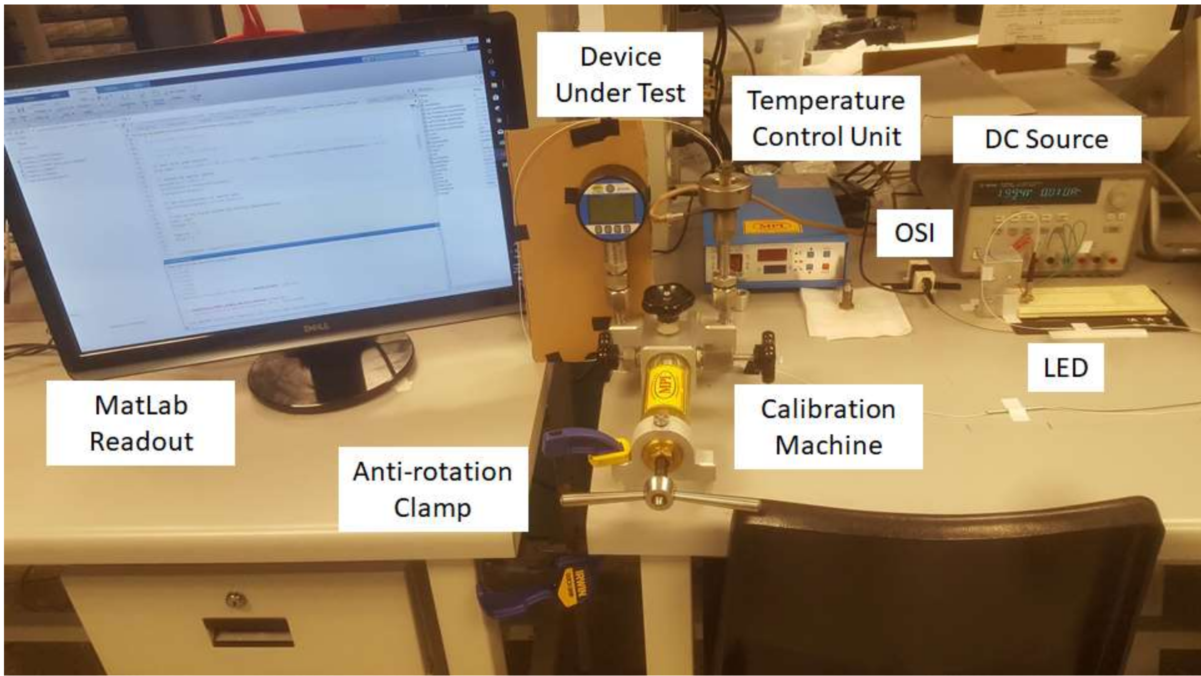

Figure 44: Experimental Set-up

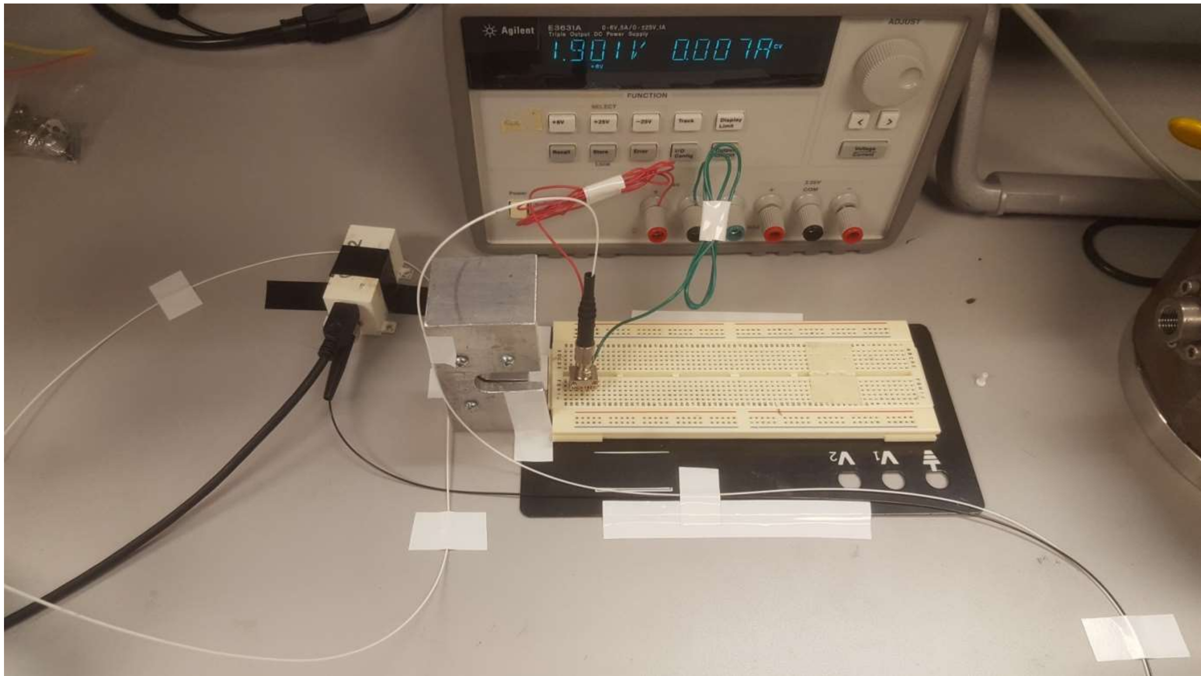

Figure 45: LED breadboard

7.1 Proof of Concept Trials

The PoC device is used as a starting point to verify the correct operation of the experimental system. These chips provided an expendable and high reflection intensity framework to test and troubleshoot testing methodologies in preparation for implementation of the SOI chips. A number of iterations of the packaging and testing procedure were evaluated using the PoC chips in development of the final methodology presented in this work. Two sets of room temperature trials were performed from 0 to 1000 PSI, the results are shown below in Figure 46 and Figure 47. These are collected using the same experimental set-up, but with two different PoC chips of the same design in order to reduce the impact of plasticity in the results. Variation in the intensity and phase between the trials indicates settling or small variations of the system during operation. This may include errors such as compression of the adhesive or movement of the fiber tip, which results in unaccounted-for variation in the cavity distance.

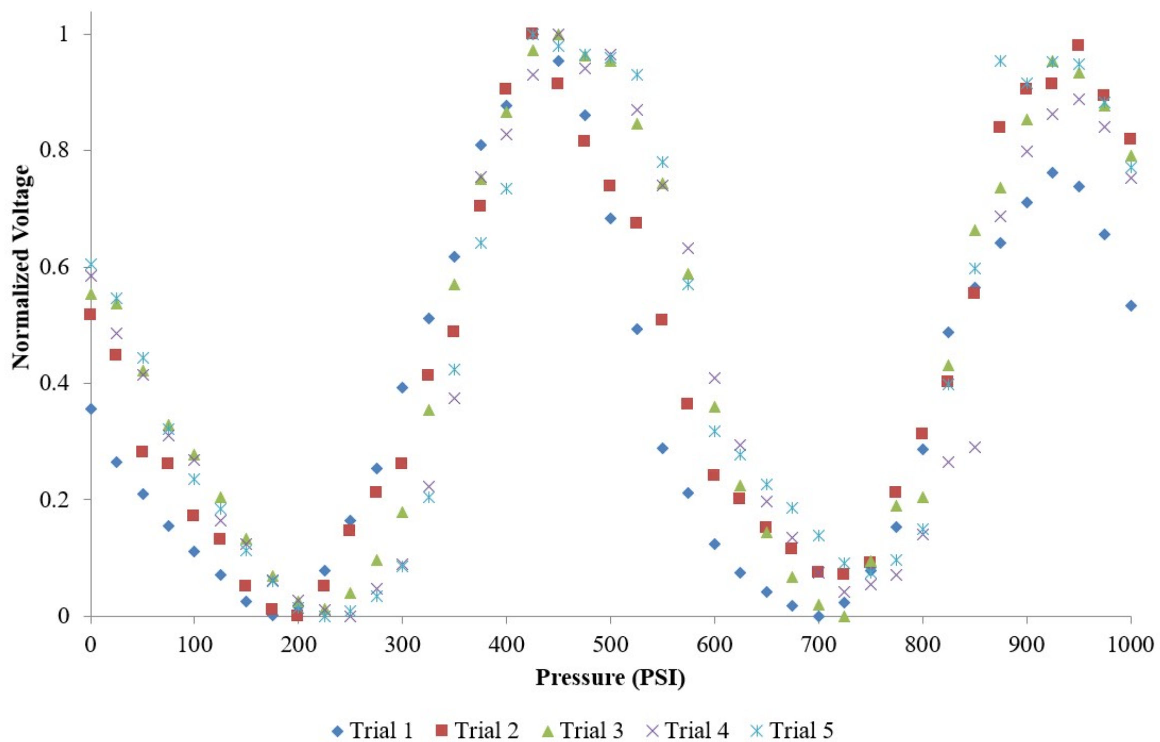

Figure 46: Normalized voltage response of chip 1 PoC from 0 to 1000 PSI in silicon oil, comparing results of five trials at 21°C

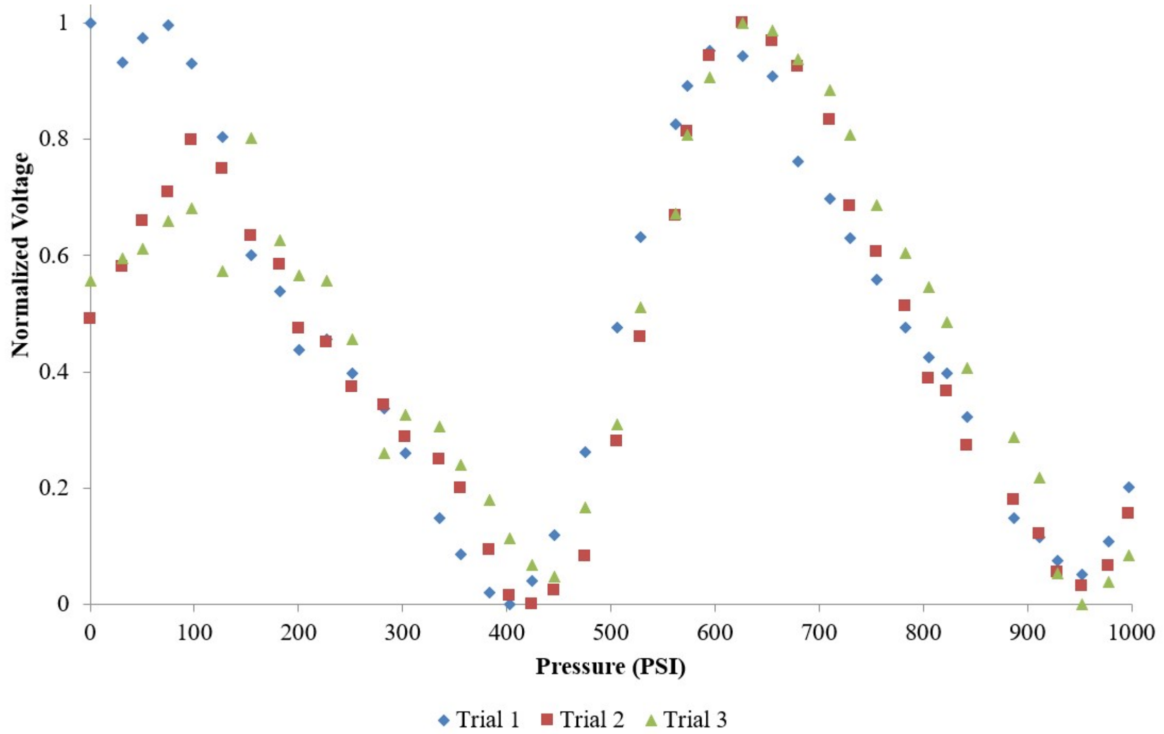

Figure 47: Normalized voltage response of chip 2 PoC from 0 to 1000 PSI in silicon oil, comparing results of three trials at 21°C

Pressure trials are repeated on the second chip at increasing temperatures from 20 to 100 °C, at pressures of 0 to 1000 PSI, the results of which are shown below in Figure 48. It is observed that increasing temperature seems to reduce the slope of the response to pressure, verifying the findings of the FEA model presented in Section 6.4.2. The "shell" geometry of the expanding membrane may also increase the light intensity by increasing the likelihood of orthogonal beam incidence as the light reflects off the surface of the membrane.

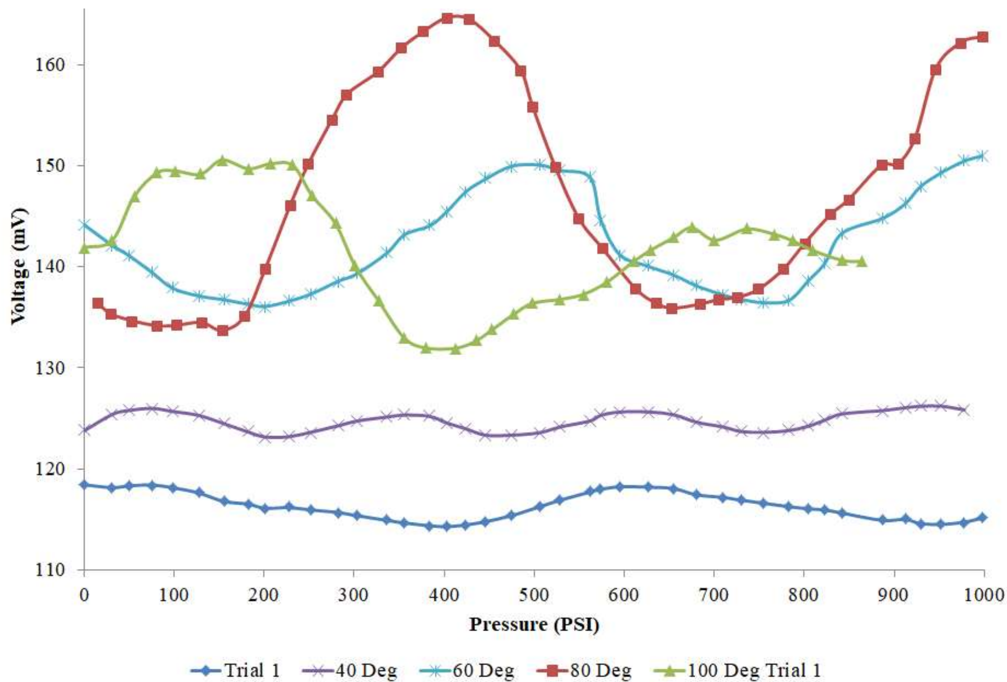

Figure 48: Voltage response of PoC chip 2 operation at various temperatures from 0 to 1000 PSI: 21, 40, 60, 80 and 100°C

However, the intensity of the high temperature probe is found to be too low and the fibers too fragile to complete testing up to 300°C. With extended time constraints, a new prototype unit would need to be fabricated to carry out further testing with temperatures above 100°C.

7.2 SOI Sensor Experimental Results

Each of the three fabricated SOI membranes are tested from 0 to 1000 PSI at room temperature over 5 trials and their signal responses recorded. In these trials, the settling effect discussed in the PoC experiments is more apparent in the response curves. Variation in the shape of the response graph between the trials is observed in all three sensors, where the sensitivity appears to change slightly with each trial. This behaviour occurred at significantly lower pressure than the expected yield strength, based on the values calculated in Section 4.2. It is expected that this behavior is caused by plasticity of the membrane and yielding in the oxide layer, which may cause changes in the membrane shape and support conditions. In some cases, the apparent plasticity resulted in significant variation of the response curve in later trials; trials in which this occurred are not compared on the calibration curves presented below.

The 200 µm membrane is the most rugged of the three fabricated in this work, offering the highest operating range but also the lowest sensitivity to applied pressure. As shown below in Figure 49, settling of the signal occurred between trials 1 and 2, while trials 3 and 4 showed strong repeatability. Due to its extended range, the fifth trial was performed from 0 to 3000 PSI trial to explore the limitations of the system performance. The response curve is shown below in Figure 50.

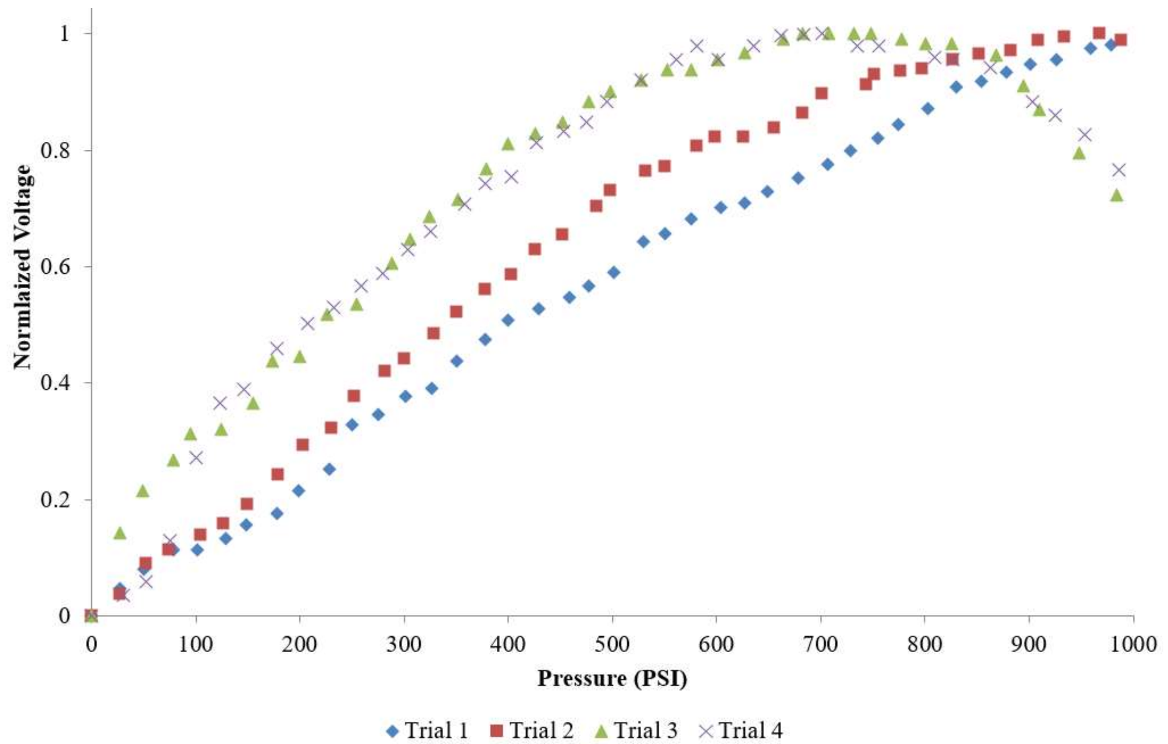

Figure 49: Normalized voltage response of 200 µm SOI from 0 to 1000 PSI in silicon oil, comparing results of four trials at 21°C

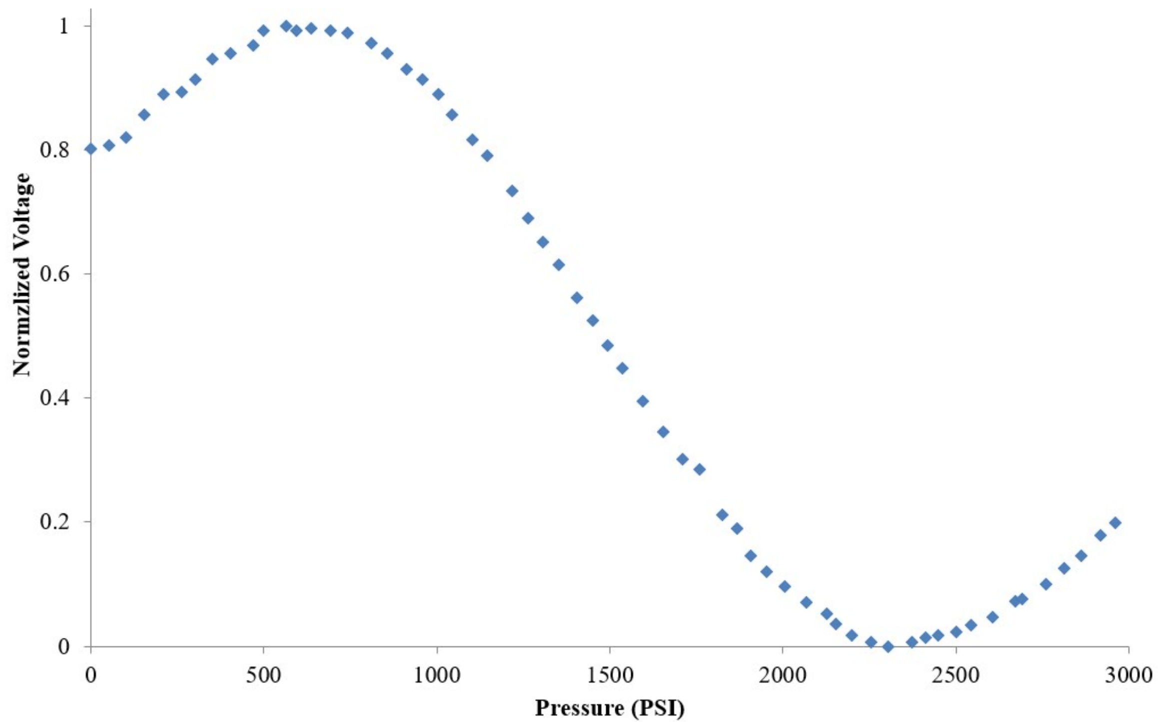

Figure 50: Voltage response of 200 µm SOI from 0 to 3000 PSI in silicon oil at 21°C

The 300 µm membrane shows a balance of medium sensitivity and ruggedness compared to the other two fabricated devices. Similarly to the 200 µm experiment, settling was observed to occur in trials 1 and 2, while trials 3 and 4 yield very similar response curves; a comparison of the experimental data is shown below in Figure 51. Significant variation in the response shape is observed in the fifth trial (shown in Figure 52), suggesting plasticity has occurred.

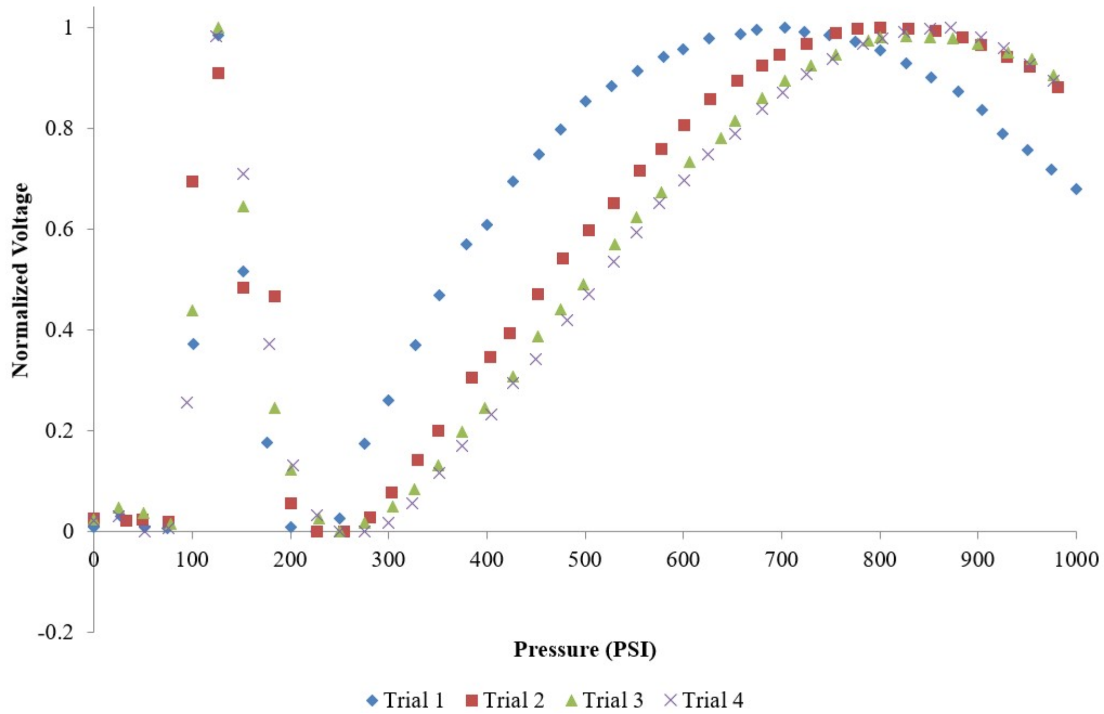

Figure 51: Normalized voltage response of 300 µm SOI from 0 to 1000 PSI in silicon oil, comparing results of four trials at 21°C

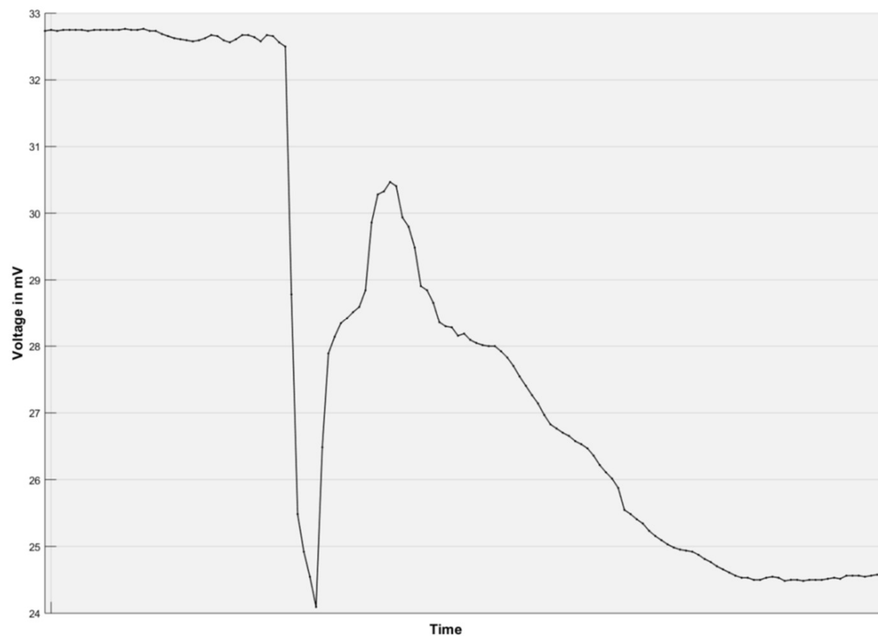

Figure 52: 300 µm SOI oil test trial 5 raw data 0 to 1000 PSI at room temperature – significant variation in the response trend suggests that plasticity occurred

The 400 micron SOI membrane is the most sensitive of the three fabricated devices, but is also the most fragile. This combination of attributes resulted in the sensor not being able to withstand the testing process, where plasticity occurred before the sensor fully settled and demonstrated strong repeatability. Trials one and two show this settling occurring, where the characteristic curves of the sensor response are shown below in Figure 53. However, plasticity is observed in trials 3 4 and 5, as noted by changes in the shape of the response trend shown in Figure 54.

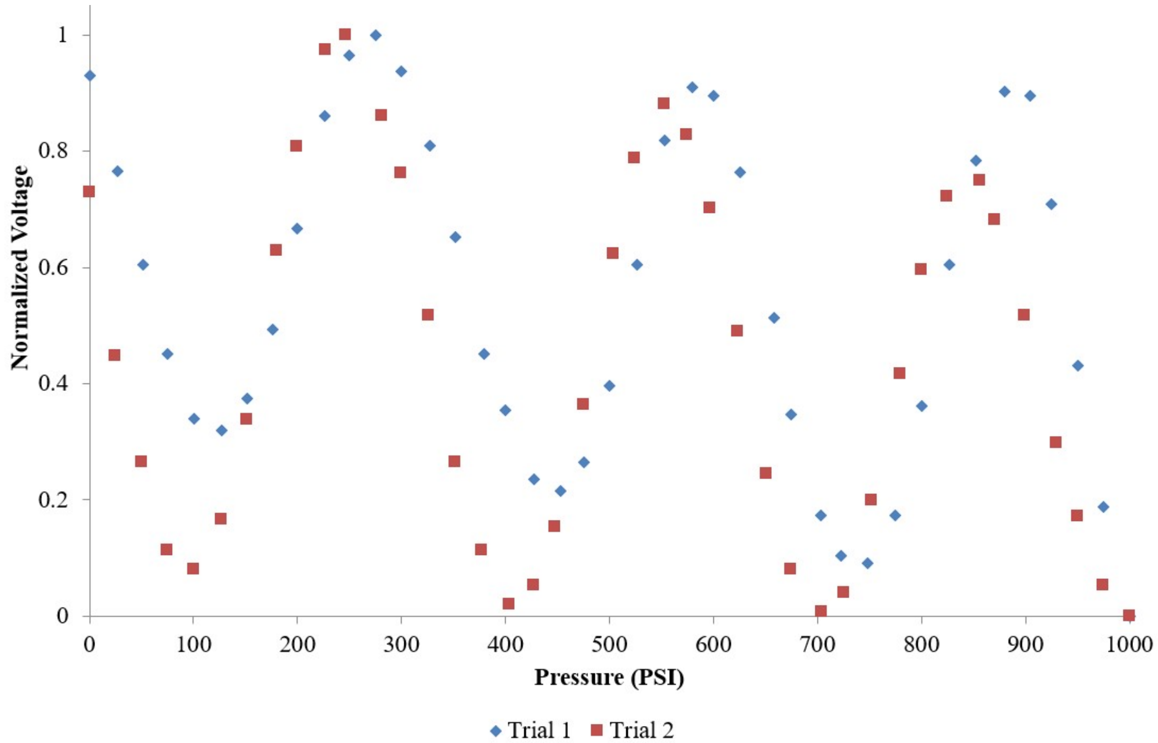

Figure 53: Normalized voltage response of 400 µm SOI from 0 to 1000 PSI in silicon oil, comparing results of two trials at 21°C

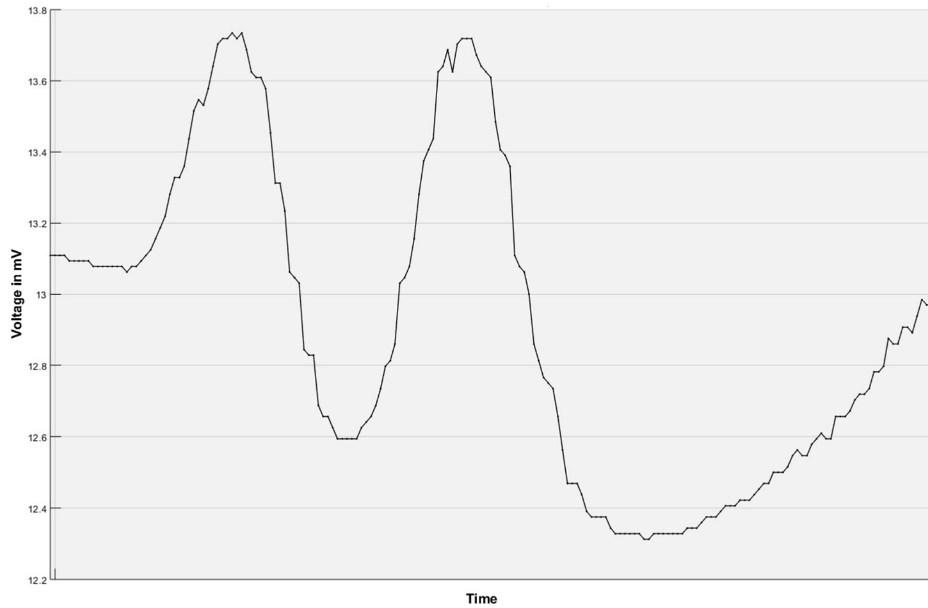

Figure 54: 400 µm SOI oil test trial 4 raw data 0 to 1000 PSI at room temperature – significant variation in the response trend suggests that plasticity occurred

7.3 Experimental Verification and Discussion

Comparing the experimental and analytical results, it appears that the fixed edge analytical model does not correctly predict the behaviour of the system for both the PoC and SOI membranes. In the FEA model, it is shown that the angle of the PoC anisotropic etched cavity results in deformation at the edges of the membrane and exhibits a non-ideal support condition. This manifests in the experimental data and FEA yielding results which are triple the predicted fully-fixed analytical displacement value. By instead using a simply supported edge condition (where the membrane edges are permitted to rotate, but not translate) the analytical model matches experimental data much more closely as shown below in Figure 55. This model, which Roark defines in Equations 30 and 31 (where variables are the same as Equation 11), produces similar results as the finite element model; predicting a maximum membrane displacement of 0.469 µm and 0.4477 µm at 1000 PSI, respectively [18].

$$\delta_{\text{max,SimplySupported}} = -\frac{0.0444Pb^4}{Et^3} \tag{30}$$

$$\sigma_{\text{max,SimplySupported}} = -\frac{0.2874Pb^2}{t^2} \tag{31}$$

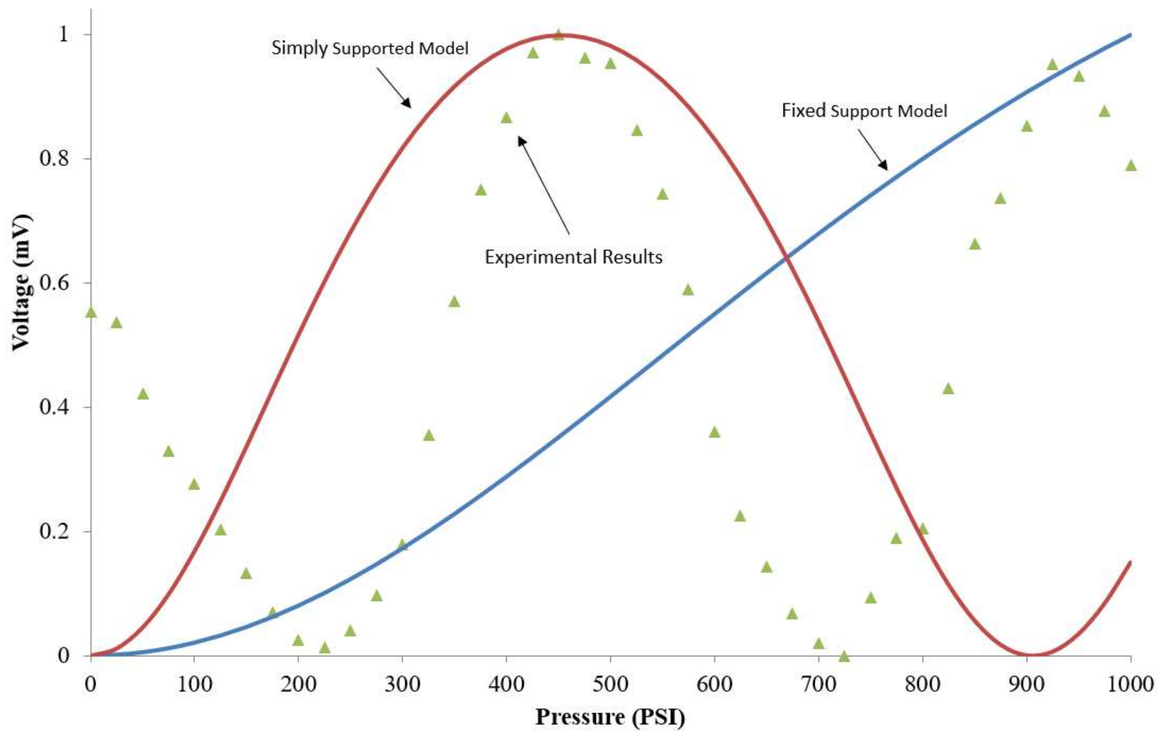

Figure 55: PoC experimental results comparison with fixed and simply supported models, at room temperature with pressures from 0 to 1000 PSI

Fitting of the experimental data and the model can be further improved by examining and adjusting the parameters of the equation. Comparing the fixed and simply supported models (Equations 11 and 30) presented by Roark, the difference in support is accounted for by adjusting the leading constant. Equation 30 is modified using this parameter to find an improved fit for the PoC experimental results according to Equation 32. Fitting is carried out using a least squares procedure error, where the error is minimized through variation of the leading constant and an additional phase constant used to align the sinusoids. A comparison with the experimental results is shown below in Figure 56.

$$\delta_{max,AdjustedPoC} = -\frac{0.0920P\ \ ^{4}}{Et^{3}} \tag{32}$$

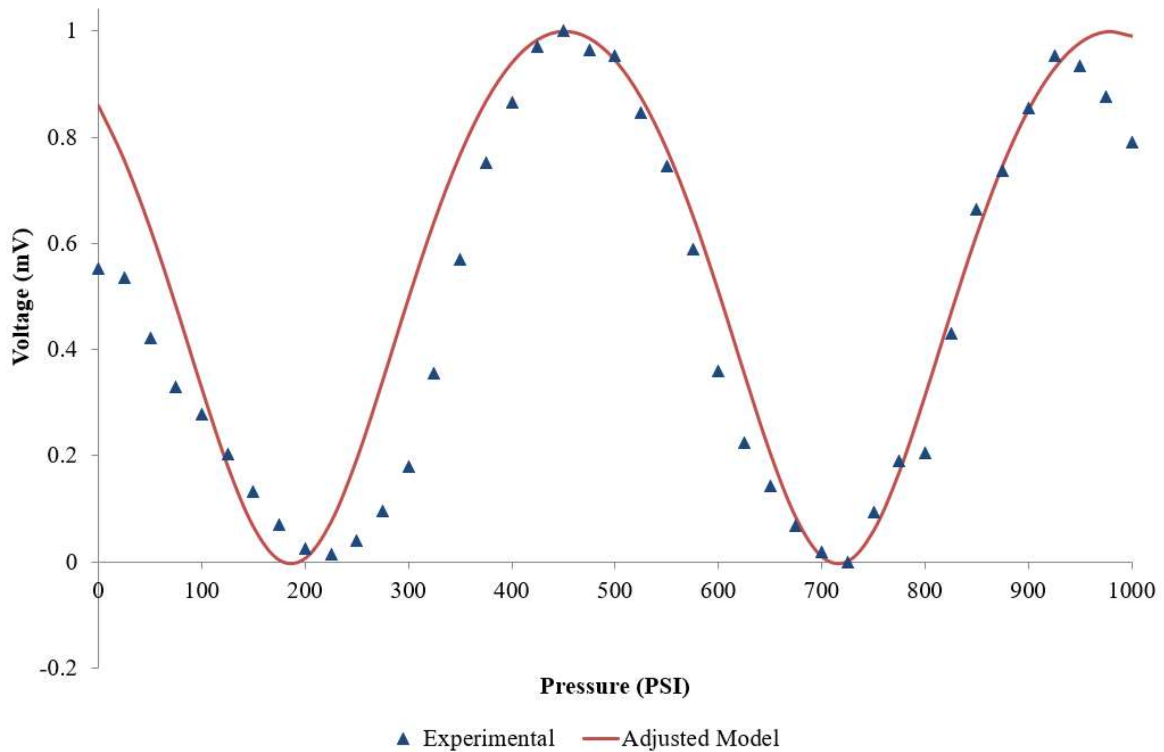

Figure 56: PoC experimental results comparison with adjusted model, at room temperature with pressures from 0 to 1000 PSI

Deviation from the experimental data is still observed, as the adjusted model maintains the ideal support assumption and predicts a linear response to pressure. This adjustment affects the slope of the predicted displacement response to pressure but not the shape or linearity of the trend - which would require curve fitting through changes to the thickness and width weighting, or implementation of additional terms. Consequently, the presented adjustments to the model only manifest in the period of the intensity response. Additionally, experimental factors result in changes to the collected optical intensity and are not accounted for in the analytical model; these may include settling of the device into the cavity as pressure is applied, epoxy deformation, or variation of the incident light.

A similar, but less significant variation of the experimental data compared to the fixed support analytical model is also observed in the SOI membrane response. It is expected that due to the difference in cross-section of DRIE compared to anisotropic etching, the sharp angles of DRIE appear to more accurately create a fully fixed support condition. The 200 µm high pressure trial from 0 to 3000 PSI is compared to the fixed support model in Figure 57, below.

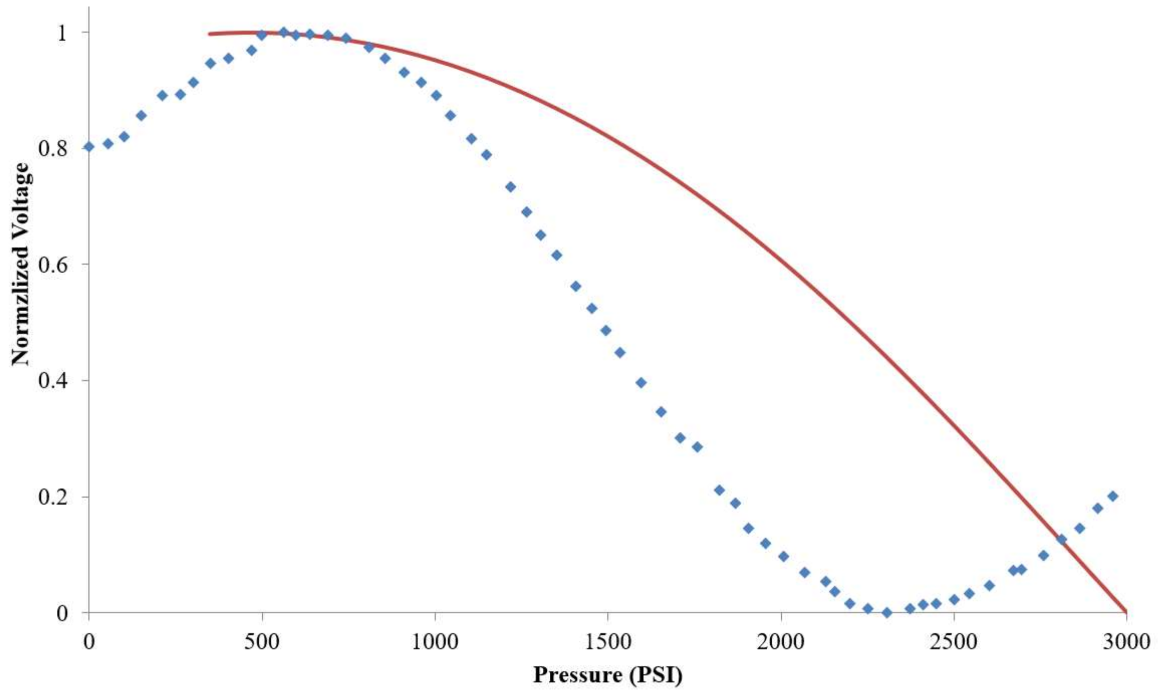

Figure 57: 200 µm SOI experimental results comparison with fixed support model, at room temperature with pressures from 0 to 3000 PSI

Using the same methodology as implemented for the PoC results, the coefficient of the fixed support model (Equation 11) is modified to better fit the experimental results. The adjusted form is given by Equation 33 and compared against the experimental data in Figure 58.

$$\delta_{max,Adjusted200\mu m} = -\frac{0.025 \quad {}^{4}}{Et^{3}} \tag{33}$$

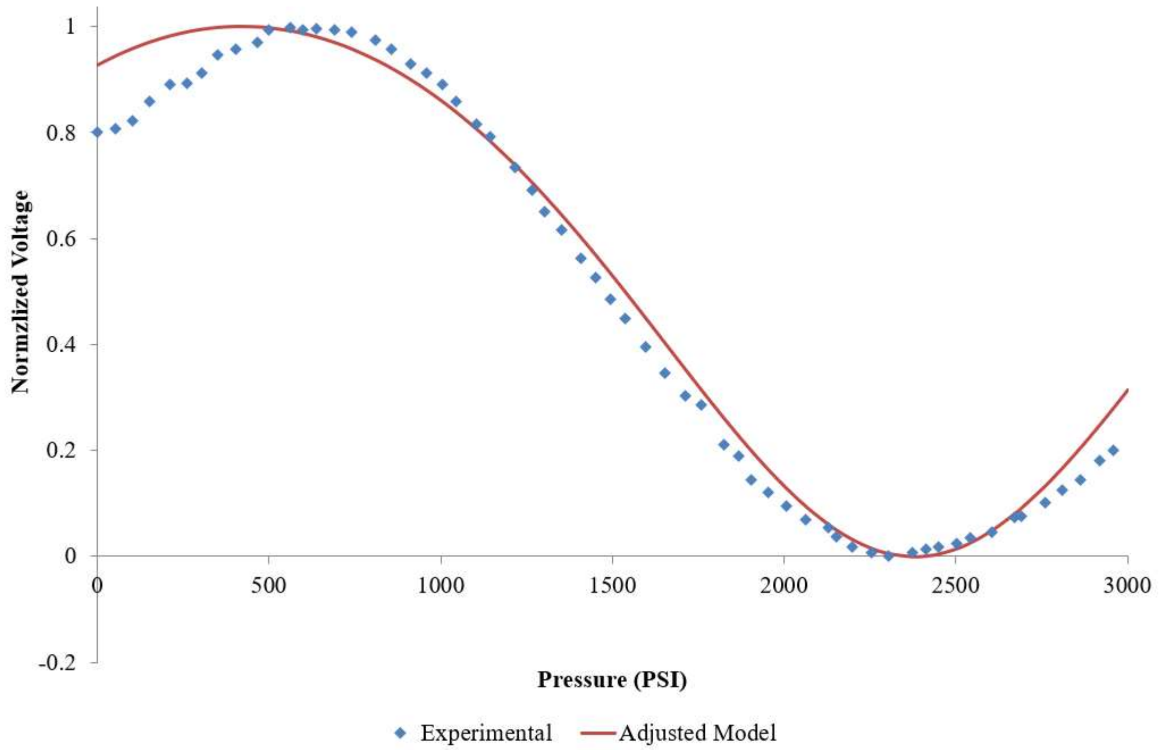

Figure 58: 200 µm SOI experimental results comparison with adjusted model, at room temperature with pressures from 0 to 3000 PSI

The same procedure is carried out for the 300 µm and 400 µm membranes, where the fixed support model is modified to improve its fit with the experimental data. The results of the 300 µm comparison are shown in Figure 59 and Figure 60, with the adjusted equation given by Equation 34. Likewise, the 200 µm comparison results are given by Figure 61 and Figure 62, with the adjusted equation given by Equation 35 .

$$\delta_{max,\,Adjusted300\mu m} = -\frac{0.0161P\ \ ^4}{Et^3} \tag{34}$$

$$\delta_{max,\,Adjusted400\mu m} = -\frac{0.0212P\ \ ^4}{Et^3} \tag{35}$$

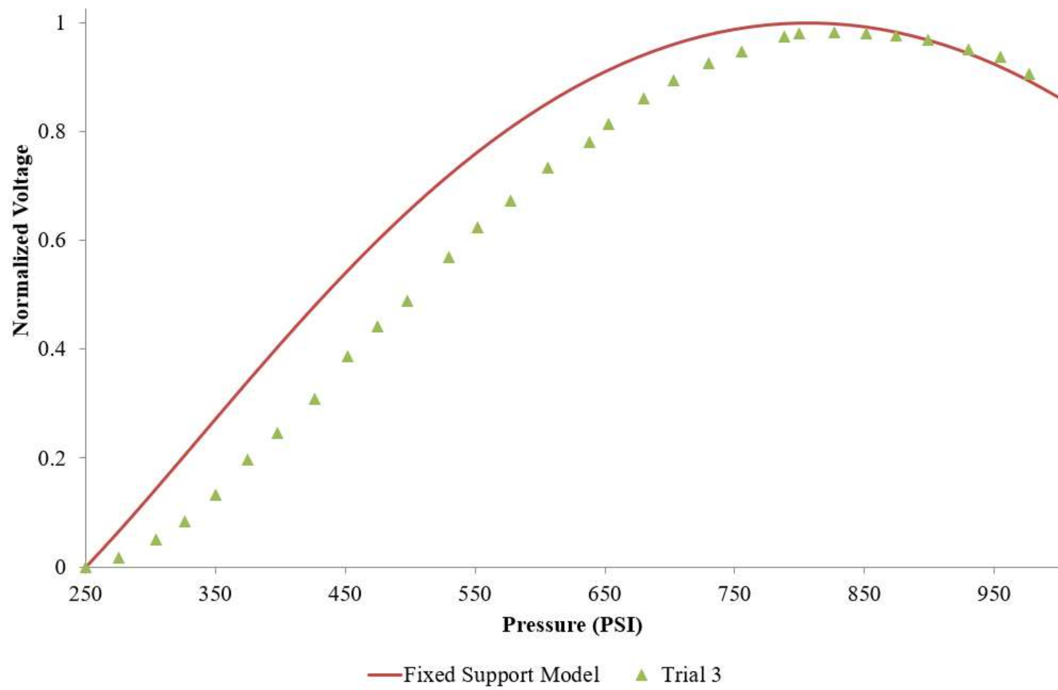

Figure 59: 300 µm SOI experimental results comparison with fixed support model, at room temperature with pressures from 0 to 1000 PSI

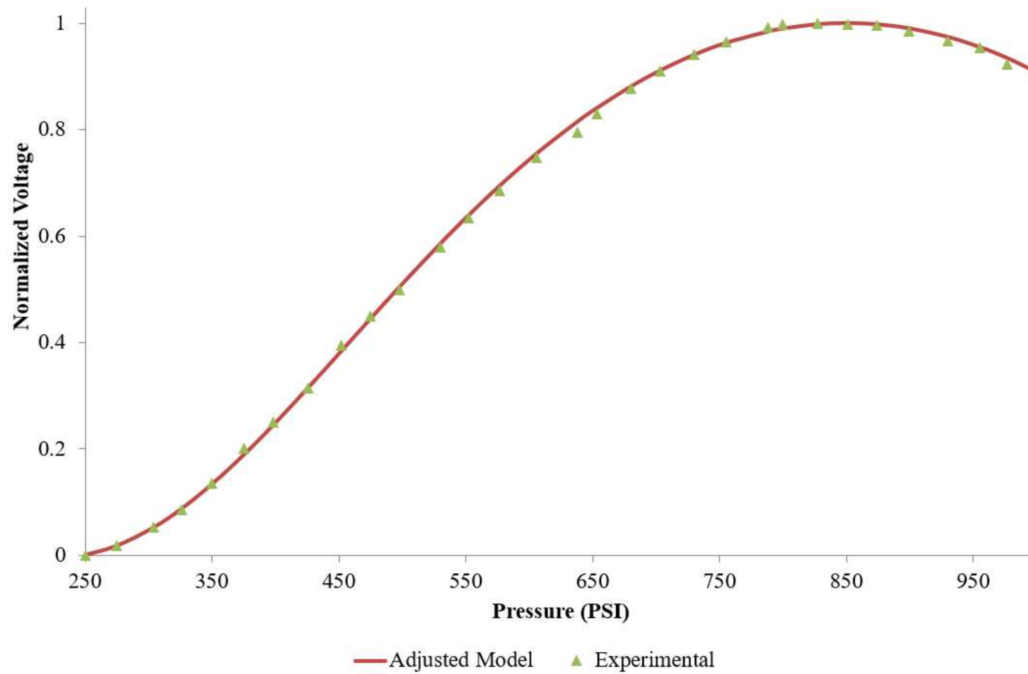

Figure 60: 300 µm SOI experimental results comparison with adjusted support model, at room temperature with pressures from 0 to 1000 PSI

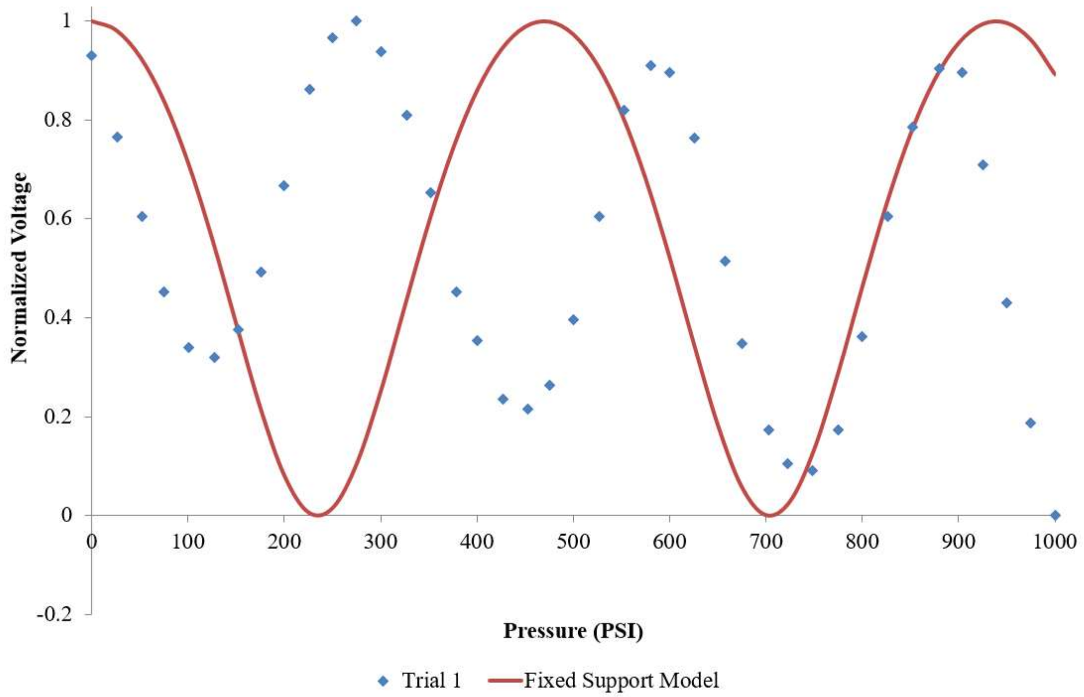

Figure 61: 400 µm SOI experimental results comparison with fixed support model, at room temperature with pressures from 0 to 1000 PSI

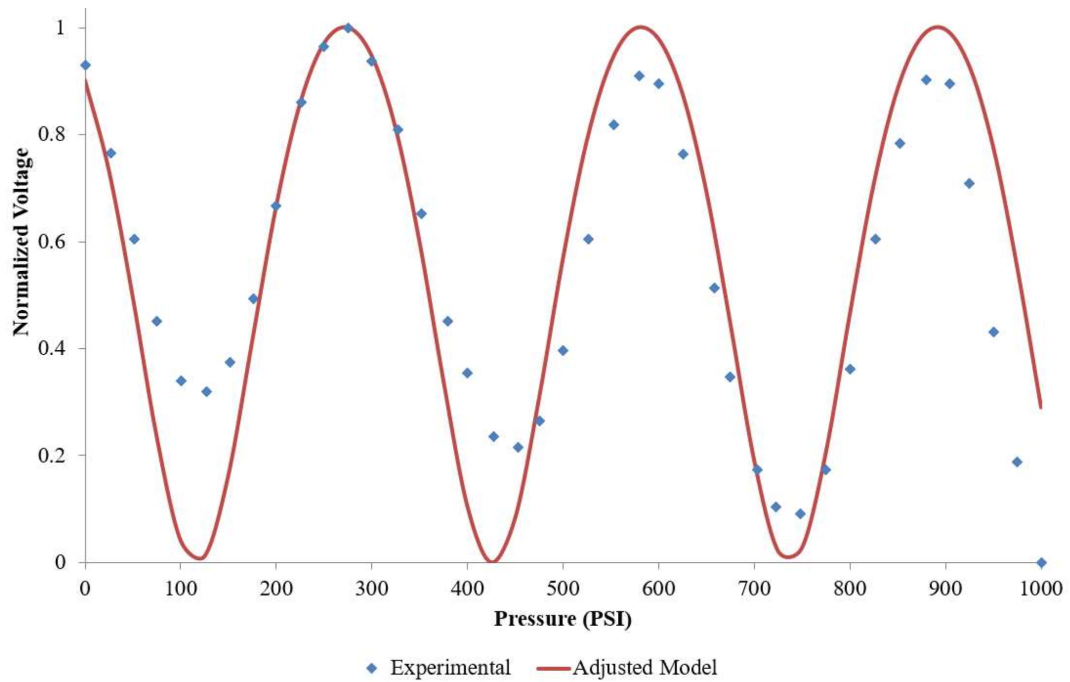

Figure 62: 400 µm SOI experimental results comparison with adjusted model, at room temperature with pressures from 0 to 1000 PSI

7.4 Sensor Behaviour Characterization

The behaviour of the sensors is characterized based on their performance in the linear operation region. For each sensor design, trials which yielded similar voltage trends are averaged and plotted against pressure to find a linear fit as shown below in Figure 63. This plot is the sample used for further analysis to determine the sensitivity, dynamic range and grade of linearity of the various sensor designs. The response time of the sensor is determined by the querying rate of the OSI and is set in the Arduino programming.

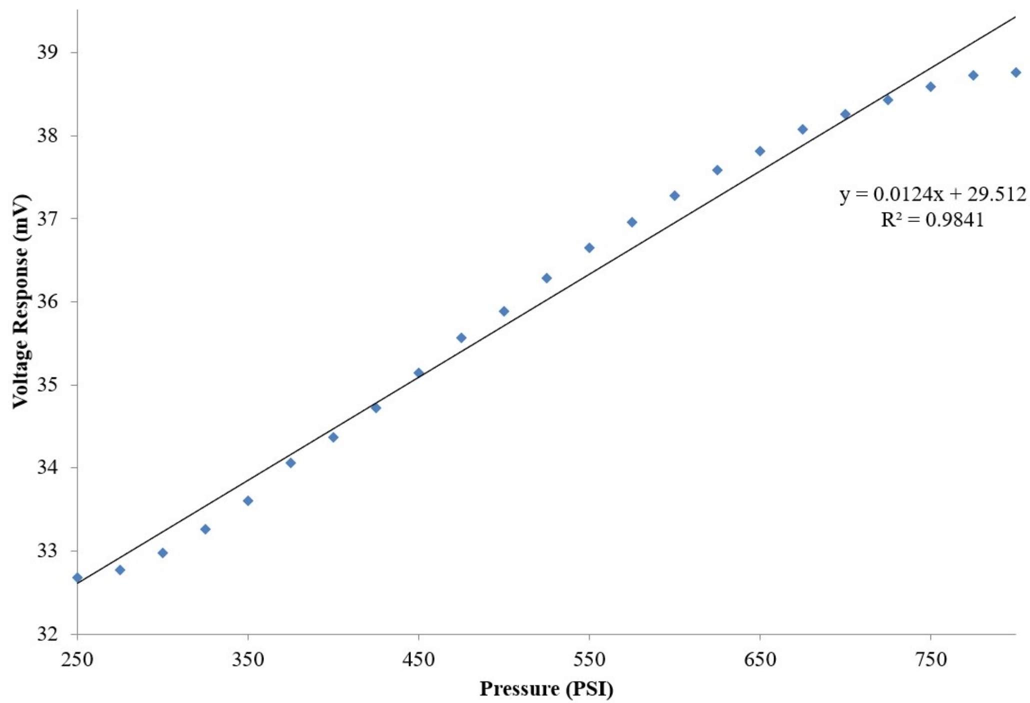

Figure 63: 300 µm SOI sensor characterization plot, average of trials 2-4

7.4.1 Sensitivity

The sensitivity for the devices considered in this analysis is defined by the membrane deformation response to an applied external pressure; this is analytically predicted by the unit deformation response based on Equation 7. Experimental resolution is limited by the smallest detectable intensity voltage response of the photodetector, which is rated to be 0.55 A/W. This exceeds the rated coupled power of the LED of 600 µW, but a response is still registered from the OSI. As such, use of more sophisticated optical equipment would be required to determine the exact output wattage change per unit PSI from the fiber during operation. Consequently, the sensitivity is approximated by recognizing

that "trough to peak" of the sinusoidal intensity function occurs with cavity distance change of ¼ wavelength and dividing by the change in applied pressure over that period, as expressed in Equation 36 below. The resulting approximate experimental sensitivity values are compared to the predicted analytical values (carried forward from Table IV in Section 4.2) below in Table IX.

$$Sensitivity = \frac{\frac{\lambda}{4}}{P(V_{LocalMax}) - P(V_{LocalMin})} \quad (36)$$

Table IX: Comparison of predicted and experimentally observed sensitivity

	Predicted (nm/PSI)	Experimental (nm/PSI)
PoC - Fixed	0.139	0.94
PoC – Simply Supported	0.454	
SOI – 200 µm	0.0577	0.124
SOI – 300 µm	0.292	0.36
SOI – 400 µm	0.922	1.4

Experimental results consistently demonstrate sensitivities higher than expected through their analytical analysis. This suggests that the elastic modulus is overestimated in the analytical model, or the as-fabricated membrane dimensions result in a softer response.

7.4.2 Dynamic Range

The dynamic range is defined as the linear section of the sensor response, which is selected to ensure a consistent change in the signal response to applied pressure. This is primarily determined by the sensing wavelength, which determines the amount of deflection that can occur before the sinusoidal signal response will begin to repeat. As such, the dynamic range is selected to enable the device to read unique values for each applied pressure of interest, thus avoiding the issue of sinusoidal ambiguity. Consequently, the initial position of the probe tip relative to the membrane is critical to ensure that the sensing region is correctly calibrated considering the sensitivity of the device. Both pressure and temperature can have an impact on the behaviour of the range of the system, so the initial probe position must be adjusted according to the expected thermal expansion. The experimental and predicted dynamic ranges are summarized in Table X, below.

Table X: Comparison of predicted and experimentally observed dynamic range

	Predicted (PSI)	Experimental (PSI)
PoC	175 to 425	250 to 450
SOI – 200 µm	0 to 3700	600 to 2300
SOI – 300 µm	75 to 800	250 to 800
SOI – 400 µm	50 to 275	125 to 275

Comparing the predicted and experimental results, the experimental values consistently show a smaller dynamic range. This is expected due to the increased sensitivity of the as-fabricated device, which results in higher membrane deflection values than shown in the analytical values.

7.4.3 Grade of Linearity

The linearity of the sensor response is quantified as the percentage error of the data set from a fitted linear trend. This represents the consistency of the response to stimulus, where a large linearity error suggests significant variance in response data when exposed to the same change in stimulus at different points in the calibration curve. The grade of linearity is calculated by taking the percentage difference between the voltage offset of two parallel lines which pass through the minimum and maximum points of the output curve (visualized below in Figure 64). The slope of these lines is based on the fitted linear equation determined at the start of this section.

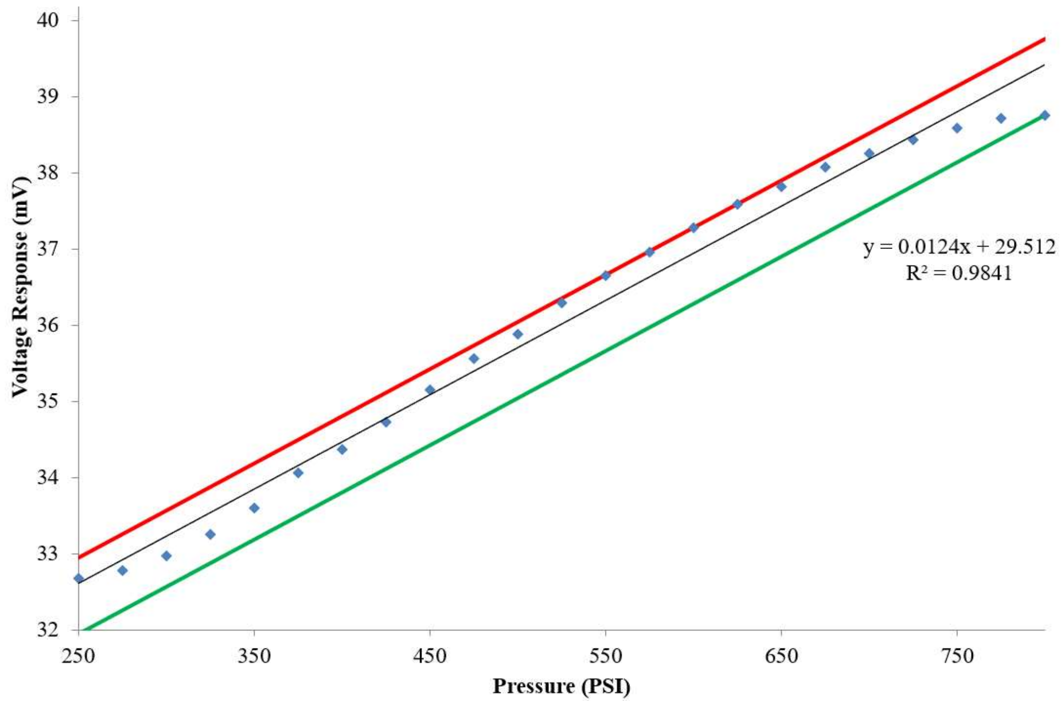

Figure 64: Linearity visualization

The dynamic range established above is examined using this linearity analysis and the calculated percentage error of full scale results are shown in Table XI. Linearity of the analytically predicted response is not compared to the experimental data in this work, due to large variance based on the examined region selected. Determining the "linear region" is based on the ability to fit a constant slope to a set of points, the limits of which are determined arbitrarily through minimization of the non-linearity. As such, small changes in the limits of this data set can result in linearity values varying from the order of tenths of a percent to errors exceeding 25%.

Table XI: Experimental grade of linearity

	Experimental
PoC	1.9%
SOI – 200 µm	0.46%
SOI – 300 µm	2.6%
SOI – 400 µm	1.4%

7.5 Reproducibility and Error

Through examining the analytical models discussed earlier in this work, a relative order of magnitude for the relative possible error sources is established. Recall that the intensity of the optical response is dependent primarily on changes in the cavity distance of the sensor; referring to the membrane deflection equations, errors in each variable is to be examined individually and their relative impact compared. Pressure, the measurand of the system, is displayed on the testing apparatus through a digital gauge and is controlled using a hand-rotated lever. As pressure increases, the resistance to further changes in pressure also increases and shows a tendency to drift toward zero unless a counter-force is applied. This behaviour introduces human error during the gathering of test data, as there may be small errors in the accuracy of applied pressure (ie. 103 PSI at the time of reading, when it should be 100 PSI). Membrane side length and thickness have the most significant impact on prediction of the sensor's behaviour but are not included on the specification sheet; these are dependent on the supplier's fabrication procedure and measurement error at the lab when using the optical inspection system. Finally, elastic modulus and Poisson's ratio material properties are also not provided by the supplier and have similar impact on sensor behaviour to the pressure accuracy. These values are estimated through literature sources, but deviation is expected from the true as-fabricated values. Additional sources of error in the behaviour of the system are as follows:

- Nonlinear stress response
- Deformation in optical fiber
    - Affects transmission of light and therefore the resulting signal collected
- Non-orthogonal optical incidence
    - Shell geometry of membrane deflection
    - Large deflection error in membrane
    - Manufacturing tolerance
- Non-ideal membrane loading conditions
    - Axial loading
        - Residual stress
    - Mid-plane Stretching
        - Longitudinal deformation, in addition to transverse
- Large deflection causes load rotation, changing the force vector due to pressure
- Inconsistency of source light
    - Changes due to temperature, current, etc.
- Error in pressure application due to manual input

Chapter 8
Conclusions

In this thesis, a Fabry-Perot interferometric pressure sensor was analyzed and developed that is capable of operating in harsh environments. The theory and applications of optical fiber Fabry-Perot interferometer pressure sensors has been described. It is shown that the discussed technology offers improved range and resolution over piezoresistive sensors, at a lower cost and significantly reduced size, among other advantages. Additionally, it is immune to RF interference and forgoes the temperature limitations of semiconductor doping, allowing for sensing in procedures where piezoresistive sensors could not be used. This technology can be implemented in a variety of systems due to the versatility of the concept, providing applications in a wide array of procedures: such as harsh manufacturing environments, local invasive blood pressure sensing, and force transduction.

Analytical and FEA models are used to predict the behaviour of existing sensors produced using anisotropic etching, as well as design and produce three custom sensors using SOIMUMPS. Once the sensors are obtained, destructive testing is carried out in order to verify the as-fabricated membrane dimensions of both the PoC and SOI chips. The mechanical behaviour and material properties of the membrane are examined to create a basis for the analytical model. FEA simulations carried out on the geometry suggest that deformation of the device structure may produce a non-ideal support condition, resulting in four times greater membrane deflection than analytically predicted.

Thermal impact on sensor response is examined through a combination of analytical and FEA methods. Position error due to the system packaging is quantified through calculation of the thermal expansion of the components of the system, where the expected initial cavity distance is expected to change by 1 and 0.4 times the wavelength in the PoC and SOI systems, respectively at 1000 PSI and 300ºC. This deformation is negligibly affected by the changes in material properties with temperature; however, the sensitivity of the membrane will be slightly increased due to softening of the elastic modulus and changes to the refractive indices. Thermal expansion of the PoC device at 100ºC is modeled using FEA to determine the impact on the membrane response. It is shown that as temperature increases, the chip expands upwards and upwards from the fixed base of support. This results in significant deformation and stretching of the membrane away from the probe tip, increasing the initial cavity distance by a further calculated 0.32 µm. The device is then modeled at 100°C and 1000 PSI, showing a maximum displacement of 0.11 µm at the center of the membrane. This is

significantly lower than the 0.4477 μm predicted by the mechanical model at room temperature, suggesting that the sensitivity of the membrane is expected to decrease at elevated temperatures due to thermal deformation.1

Finally, the PoC and three SOI sensors are experimentally validated and compared against the predicted behaviour. The PoC device is tested at temperatures from 21 to 100°C and pressures from 0 to 1000 PSI. As predicted in the FEA and analytical models, increasing temperature causes an offset in the cavity distance and a reduction in the sensitivity of the membrane. The 200, 300 and 400 μm SOI devices are testing at room temperature from 0 to 1000 PSI, with an additional trial being carried out on the 200 μm chip up to 3000 PSI. These results corroborate the findings of the FEA model, suggesting that deformation of the supporting structure is resulting in non-ideal response to pressure. Based on comparison of the experimental results and analytical models, a series of adjusted models are developed to fit the non-ideal membrane behaviour observed through modification of the equation's leading coefficient. Analysis of the results finds that the PoC device operates with a sensitivity of 0.94 nm/PSI over a dynamic range of 250 to 450 PSI with 1.9% full scale linearity error. The best operating SOI device is the 200 μm membrane, with sensitivity of 0.124 nm/PSI from 600 to 2300 PSI and 0.46% full scale linearity error.

Further development and deployment of these sensors will place Canada at the forefront of harsh environment pressure sensing, providing the framework for future research and commercialization. Beyond manufacturing, this work has applications in the biomedical, automotive and aerospace industries. Further, it will enable companies to develop plastic-molding manufacturing techniques taking advantage of increased access to in-process data previously unavailable. With expanded operating ranges, these processes will access new materials and increase production safety, quality and efficiency.

8.1 Contributions

The following are the contributions from this work:

1. A high temperature optical interference pressure sensor has been produced, which exceeds the currently published extrinsic FPI operating maximums of 100 PSI and meets 300 °C. Further, a stainless steel supporting structure is developed which improves the alignment and reliability through utilizing mechanical means to arrest movement in the sensing

system. SOIMUMPS multi-user manufacturing is utilized for fabrication of silicon membranes and material property testing devices.

2. Analytical prediction of the thermal effect on performance is implemented. This includes accounting for the variation of mechanical properties and as a function of temperature, which has been observed in literature but not predicted for the purposes of sensor operation. Additionally, thermal expansion of the materials to are predicted to account for aberrations in the cavity distance. Using analytical prediction of deformation of the membrane, in conjunction with prediction of mechanical property and expansion drift with temperature, a platform for increased fidelity of high temperature sensors is proposed.
3. It is shown that the standard membrane assumptions do not adequately predict the deformation behavior of both anisotropic and DRIE SOI etched devices. This is demonstrated through comparison of analytical and FEA models to experimental results, which show significant deviation in the shape of the deflection trend. It is shown that these devices do not form ideal supports due to deformation in the structural material. Adjusted deflection models are fitted to the experimental data to correct for the apparent discrepancy. Additionally, SOI devices show plasticity after repeated trials significantly before their expected yield strength.

8.2 Future Work

This work presents a functional extrinsic Fabry-Perot interferometric pressure sensor for harsh environments, which provides a framework on which improvements to the system can be implemented. Implementation of additional features and stability would better prepare this device for commercial viability.

8.2.1 Prediction of Non-ideal Sensor Behaviour

It has been shown that the produced sensors do not follow the analytical models typically used to predict the behaviour of MEMS pressure devices. However, the adjusted models are based on curve fitting to experimental data and do not produce a consistent value of the leading coefficient. Further work should be completed to identify or produce a model which is capable of better predicting the behaviour of membranes fabricated using DRIE and anisotropic etching.

8.2.2 Additional Stabilization

Throughout testing of the system, it was found that the membrane response was very susceptible to noise and external disturbances. This could be improved through the use of a reduced length single mode fiber, which would significantly lower the impact of these disturbances on the propagation of reflected modes. As the system is implemented in an industrial setting, vibration isolation will need to be incorporated to minimize noise in the system. Additionally, the use of a reference fiber would allow for the system to account for changes in the light source. Finally, implementation of a motor to set and maintain pressure in the laboratory environment would eliminate human error in the calibration machine.

8.2.3 Environmental Protection

Implementation of an additional layer to separate the membrane from the fluid environment may reduce the possibility of damage to the sensor. This could be accomplished through the use of a mechanical transfer plate, or parylene coating. It is expected that behavior would need to be predicted using composite material assumptions, but directly mating of the membrane and protecting layer is critical to this implementation.

8.2.4 Expanded Functionality

This work is to be expanded through adding functionality, to simultaneously determine temperature and flow-rate, and expanding the operating conditions beyond 500 °C and 10000 PSI. This will be achieved through integration of supplementary methods, such as Doppler flow and in-fiber Bragg-grating temperature detection. Using this approach, flow obstruction will be minimized and real-time data will be used to correct for temperature aberrations in pressure and flow readings.

A priority of this project will include research and selection of alternative membrane and optical fiber materials. Deflection results from this MASc thesis device will be used to optimize the required resolution and linearity of the sensor, informing the mechanical design and manufacturing process for the improved membrane. Furthermore, an optical system will be designed that compensates for the low maximum operating temperatures of commercially available fiber couplers, while avoiding the high cost of sapphire fibers. In addition to considerations for the potential of creep (i.e. temporally dependent thermo-mechanical plasticity), the model developed in this MASc thesis can account for the system's mechanical and optical properties as functions of temperature in the design

8.2.5 Medical Applications

These sensors can be used to find the local blood or fluid pressure in the body during medical procedures to ensure the safety of the patient. As the devices are fragile and expensive, the technology is mostly unusable for surgical applications, prompting the need for an improved alternative to be developed [9]. The size of the sensors is on the order of 3mm square, requiring pressure to be measured indirectly as the sensor cannot be inserted into small vasculature [55]. As a result, pressure is transferred through a fluid-filled catheter with diameters of ~0.6mm to an external sensor. The devices suffer from slow time response and mechanical disturbances due to fluid inertia in long catheters [11]. A small, robust and inexpensive alternative is needed to these devices, which is able to resist RF interference. This would expand the possible applications of intravascular pressure sensors and improve their surgical viability.

As fiber optic devices are immune to EMF (Electro Magnetic Field) interference, their use in procedures with high EMF becomes a clear application of the technology [2]. There are three main sources of this interference in medicine: MRI (Magnetic Resonance Imaging), which has applications in diagnostic imaging; RF ablation, used in cardiology and cancer treatment; and localized dielectric heating (shortwave diathermy), which is often used in physiotherapy [56].

In order for a device to be useful for the medical field, it must have a sensitivity of ~1mmHg (0.133 kPa) over a range of ~250mmHg (33.33 kPa) [57]. This is the standard biological pressure range required in medicine.

Appendix A – SE103 Data Sheet

Model SE103
Sensor Dies for General Purpose

Description

The model SE103 is designed for gauge (relative), absolute or sealed gauge pressure measurements for general purpose. As a piezoresistive sensor die, the SE103 is based on micro-electromechanical systems (MEMS) technology. The die is available in a foot-print of either 3.45mm x 2.70mm or 2.45mm x 2.45mm, depending on the pressure range.

Compared with the SE101, the SE103 has silicon-on-glass structure. Moreover, the SE103 has better linearity for precise pressure measurements. In addition, there is a metallic layer made from aluminum on the surface of the die, which can prevent the bridge resistors from electromagnetic interference and humidity.

Designed as an uncompensated sensor die, the SE103 is available in an open-bridge circuit with 5 solder pads for both adjustment and temperature compensation of zero offset. The SE103 sensor die can also have customized parameters, e.g. the die with a closed-bridge circuit of 4 solder pads, with a customized pressure range, with a sealed gauge cavity for gauge pressure measurements, or finished without glass constraint.

Before packaging, each SE103 sensor die is tested and inspected.

SE103 wafer

Features

- gauge pressure ranges: 0.1bar, ..., 25bar
- absolute/sealed gauge pressure ranges: 1bar, ..., 1000bar
- non-linearity up to 0.25%fs
- high reliability and stability
- suitable for either constant voltage or current excitation

Applications

- metrology applications
- process control systems
- pneumatic and hydraulic systems
- biomedical instruments
- automotive

Wheatstone Bridge Circuit Diagrams

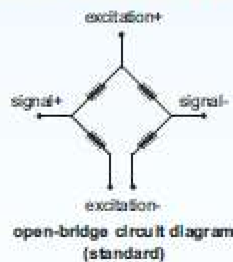

open-bridge circuit diagram (standard)

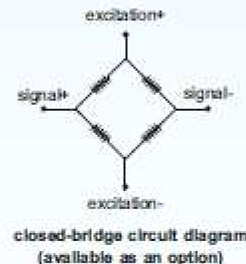

closed-bridge circuit diagram (available as an option)

BCM SENSOR TECHNOLOGIES BVBA

Industriepark Zone 4, Brechtsebaan 2
B-2900 Schoten - Antwerpen, BELGIUM

Tel.: +32-3-238 6469
Fax: +32-3-238 4171

website: www.bcmsensor.com
email: sales@bcmsensor.com

Model SE103
Sensor Dies for General Purpose

Dimensions

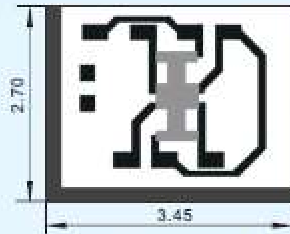

terminal pads layout
for rated pressure ≤ 25bar

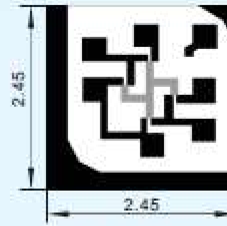

terminal pads layout
for rated pressure ≥ 40bar

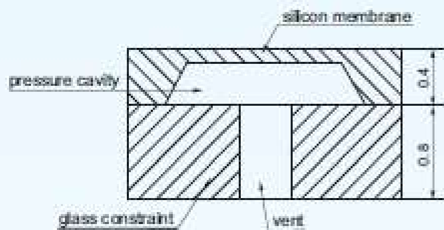

cross-section
glass constraint with vent
for gauge and differential pressure measurements
(standard)

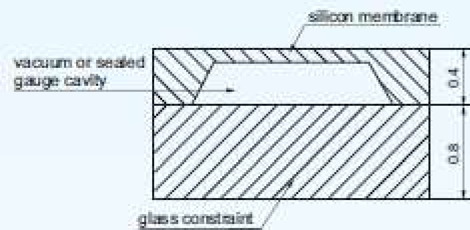

cross-section
glass constraint without vent
for absolute and sealed gauge pressure measurements
(standard)

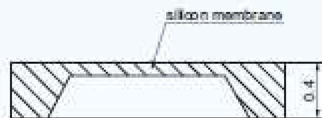

cross-section
no glass constraint
for gauge and differential pressure measurements
(available as an option)

Note:
- All dimensions in mm.
- The terminal pads are made from aluminum.

BCM SENSOR TECHNOLOGIES BVBA

Industriepark Zone 4, Brechtsebaan 2
B-2900 Schoten - Antwerpen, BELGIUM

Tel.: +32-3-238 6469
Fax: +32-3-238 4171

website: www.bcmsensor.com
email: sales@bcmsensor.com

Model SE103
Sensor Dies for General Purpose

Technical Data

Parameters		Units	Specifications	Notes
pressure ranges	gauge	barG	0~0.1, ~0.35, ~1, ~2.5, ~4, ~6, ~10, ~16, ~25	1
	absolute/sealed gauge	basA/barS	0~1, ~2.5, ~4, ~6, ~10, ~16, ~25, ~40, ~60, ~100, ~250, ~400, ~600	1
proof pressure		%fs	200 (for ranges ≤ 100bar); 150 (for ranges > 100bar)	2
burst pressure		%fs	300	
full scale output		mV	≥ 60	3
excitation	voltage	Vdc	5 (typical), 1, ..., 10	
	current	mA	1 (typical), 0.2, ..., 2	
zero offset		mV	≤ ±40	
non-linearity (NL)		%fs	≤ ±0.25 (standard), ≤ ±0.5,	4
hysteresis (HY)		%fs	≤ ±0.02	
repeatability (RP)		%fs	≤ ±0.05	
long term stability		mV/year	≤ ±0.1	
short term stability		mV/24h	≤ ±0.05	
bridge resistance		kΩ	4~6	
storage temperature range		°C	-45 ~ +125	
operating temperature range		°C	-45 ~ +125	5
temp. coeff. (TC) of bridge resistance		10^{-3}/°C	1.15 ±0.25	6
TC of zero offset		%fso/°C	0.05	7
TC of SPAN	voltage excitation	%fso/°C	0.22	7
	current excitation	%fso/°C	0.05	7
thermal HY of zero offset		%fso/°C	≤ ±0.02	
PN junction break down voltage		V (@10μA)	≥ 20	
dimensions	with glass constraint	mm	2.70 x 3.45 x 1.2 (≤ 25bar), 2.45 x 2.45 x 1.2 (≥ 40bar)	
	without glass constraint	mm	2.70 x 3.45 x 0.4 (≤ 25bar), 2.45 x 2.45 x 0.4 (≥ 40bar)	

General conditions for measurements: excitation voltage = 5Vdc, temperature = 25°C, humidity = 40%RH.

Notes:
1. For customized pressure ranges, consult BCM.
2. fs refers to full scale pressure or rated pressure.
3. Measured at full scale pressure.
4. Calculated according to Terminal Base Line (the endpoint method).
5. The +125°C is its highest operating temperature, but not its average operating temperature. Its average operating temperature should not be over 100°C.
6. Calculated as a rate of resistance change between 25°C and 70°C, and normalized by the resistance at 25°C.
7. Calculated as a rate of output change between 25°C and 70°C, and normalized by the output at 25°C, when the die is not temperature compensated.

The listed specifications and dimensions are subject to change without prior notice.

BCM SENSOR TECHNOLOGIES BVBA

Industriepark Zone 4, Brechtsebaan 2
B-2900 Schoten - Antwerpen, BELGIUM

Tel.: +32-3-238 6469
Fax: +32-3-238 4171

website: www.bcmsensor.com
email: sales@bcmsensor.com

Model SE103
Sensor Dies for General Purpose

Ordering Information

ordering code: SE103-60-A-II-OB-G8-X-(*)

pressure ranges			
010 = 0~0.1 bar	G	40 = 0~40 bar	A, S
035 = 0~0.35bar	G	60 = 0~60 bar	A, S
1 = 0~1 bar	G, A, S	100 = 0~100 bar	A, S
2.5 = 0~2.5 bar	G, A, S	250 = 0~250 bar	A, S
4 = 0~4 bar	G, A, S	400 = 0~400 bar	A, S
6 = 0~6 bar	G, A, S	600 = 0~600 bar	A, S
10 = 0~10 bar	G, A, S	customized range available as an option	
16 = 0~16 bar	G, A, S		
25 = 0~25 bar	G, A, S		

pressure type		
G = gauge	A = absolute	S = sealed gauge

non-linearity (NL)	
0.25%fs (standard)	0.5%fs

bridge type
OB = open-bridge circuit (standard)
CB = close bridge circuit (available as an option for size order)

die structure
G8 = with glass constraint of 0.8mm thickness
N = without glass constraint (available as an option for gauge or differential pressure type)

package
X = individually packaged die in plastic package (standard)
Y = diced wafer on tape
Z = non-diced wafer

"(*)" is necessary only if any customized parameter is required, otherwise it is neglectable.

Examples of Ordering Code

- standard sensor die:
  SE103-60-A-0.25%fs-OB-G8-X
- customized sensor die:
  SE103-20-G-0.25%fs-OB-N-Y-(*)
  (*): customized pressure range = 20bar.

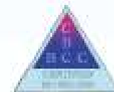

BCM SENSOR TECHNOLOGIES BVBA

Industriepark Zone 4, Brechtsebaan 2
B-2900 Schoten - Antwerpen, BELGIUM

Tel.: +32-3-238 6469
Fax: +32-3-238 4171

website: www.bcmsensor.com
email: sales@bcmsensor.com

Appendix B – On-chip Material Testing Devices

Resonant Cantilever

Through examining the resonant frequency of a set of cantilevers, the as-fabricated elastic modulus of a chip's structural layer can be determined. In their 1979 work, Torgalkar establishes a relationship between the length of a cantilever beam and its resonant frequency as shown in Equation 37 [58]. Utilizing this equation, with an assumed thickness of 25 μm, elastic modulus of 169 GPa, and density of 2500 kg/m^3, the expected resonant lengths for a range of resonant frequencies are tabulated in Table XII, below. Through measuring the as-fabricated cantilever length and using a vibrometer to test the resonant frequencies, the expected elastic modulus can be calculated. In this case, the thickness and density are assumed based on the designed values, due to the difficulty of measuring these parameters.

$$L = \sqrt[4]{\frac{Et^2}{38.34\rho f^2}} \tag{37}$$

Where L is cantilever length, E is elastic modulus, t is cantilever thickness, ρ is density, f is frequency of vibration

Table XII: Cantilever length calculation results

Frequency (kHz)	Cantilever length (μm)
20	1288
25	1152
30	1050
35	974
40	911

The curvature of the beams is measured using a profilometer, giving readings of 0.33 to 0.38 μm upwards, indicating compressive stress in the chips. This can be used to calculate the residual stress present in the devices, in conjunction with the Vernier gauges.

Vernier Stress Gauge

Zavracky et al. present a Vernier gauge design to determine the residual stress present in a chip in their 1995 work [59]. This gauge enables visualization of the structure's deformation due to residual stress as it is released from the substrate by providing reference markers to measure deflection. The geometry of the structure determines the mechanical amplification of the stress-induced deflection, where larger structures will show larger deformations but at lower resolution. By including structures with varying geometries, the as-fabricated residual stress can be measured with increased certainty.

Equations 38 and 39 are used to calculate the expected residual stress experienced in the Vernier gauge; while these equations cannot be solved analytically, they can be readily solved using numerical methods. The variables are defined visually below in Figure 65.

$$T_o = T_A - \frac{EA}{l}\left[\alpha(y_o - y_A) + \frac{1}{2}\int_0^1 [y'(x) - \alpha]^2 dx\right] \tag{38}$$

$$T = \sigma w t \tag{39}$$

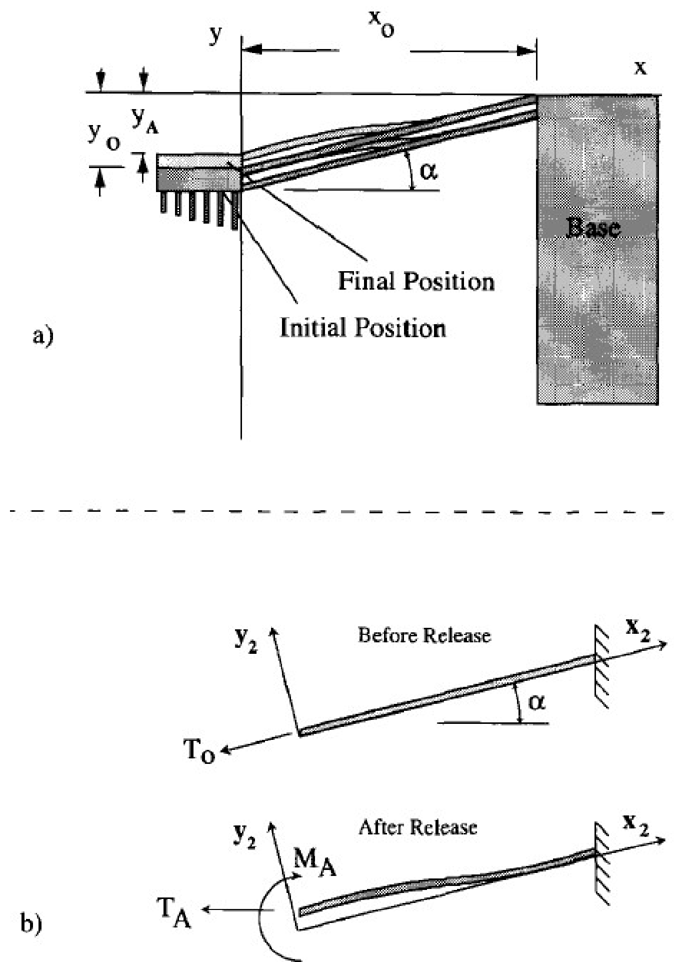

Figure 65: Vernier dimension visualization © 1995 IEEE

M-TEST

By using a combination of cantilever and fixed-fixed beams, the elastic modulus and residual stress can be determined using a combination of pull-in relationships as shown in Osterberg and Senturia's 1997 work [60]. Using equations from the paper and expected geometries from the SOIMUMPs design criteria, lengths are analytically estimated for cantilever and fixed-fixed beam structures. Through FEA, it was found that the expected pull-in voltages were much higher than those analytically calculated. It is expected that this is caused by the conductive pads being placed on the thin side of the beams, rather than on the "width", due to the orientation when using SOI fabrication. The semiconductor nature of silicon would result in unequal charge distribution through the large thickness of the beams, which may result in the much higher FEA- calculated pull-in voltages

observed. In addition, this methodology is originally designed for standard micromachined chips, where the thickness of the devices is significantly less than the length and width. Experimental testing corroborated these FEA results, for which it can be concluded that the analytical models do not predict the behaviour of these structures when actuated from their thin surface. A Matlab code is used to determine the material properties from experimental results, according to Equations 40 and 41, where S and B are material parameters determined per relationships expressed in the paper.

$$\tilde{E} = \frac{E}{1-v^2} = \frac{\bar{B}}{t_o^3 g_o^3} \tag{40}$$

$$\tilde{\sigma} = \sigma_o = \frac{\bar{S}}{t_o g_o^3} \tag{41}$$

Appendix C- Predicted Sensor Response Graphs

The response graphs presented in this section represent the predicted analytical sensor behaviour according to the equations defined in Section 4.2.1. In each figure, the maximum membrane displacement is shown and used as a point of comparison for the other operating parameters examined. The cavity distance is calculated through subtraction of the membrane deflection from the initial cavity distance, 405 μm in the PoC device and 131 μm in the SOI devices. Stress response is calculated using Equation 9 and compared against the yield strength of silicon of 3000 MPa. Finally, the expected sensor intensity response is calculated according to Equation 2.

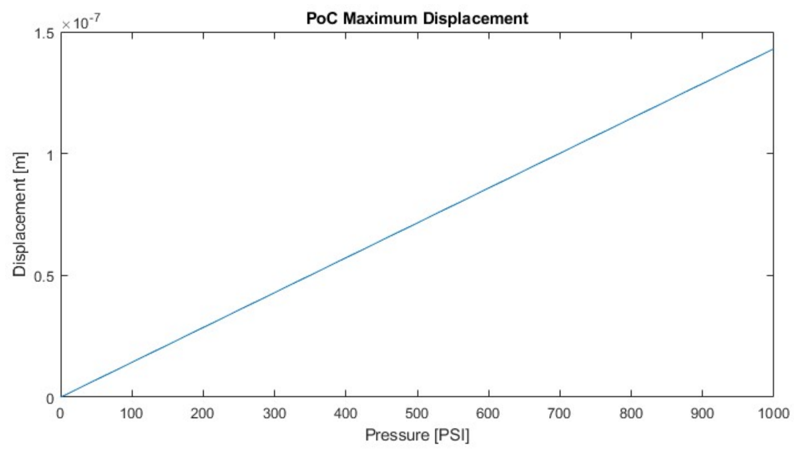
PoC Maximum Displacement
×10-7
Displacement [m]
Pressure [PSI]

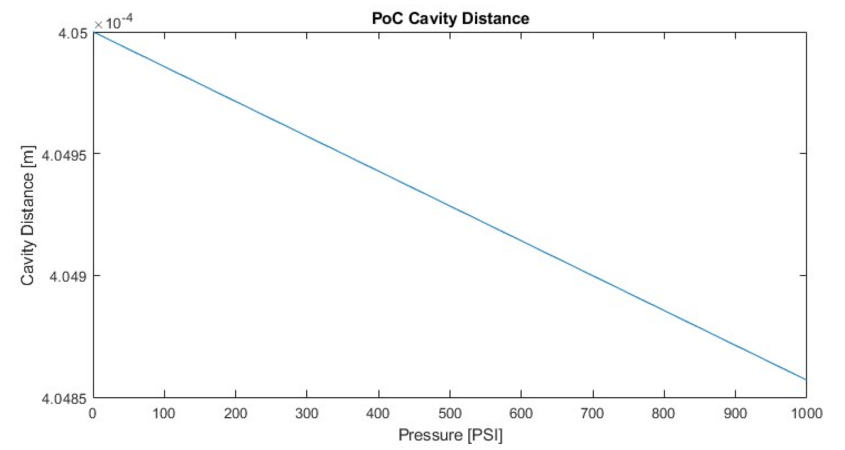
PoC Cavity Distance
×10-4
Cavity Distance [m]
Pressure [PSI]

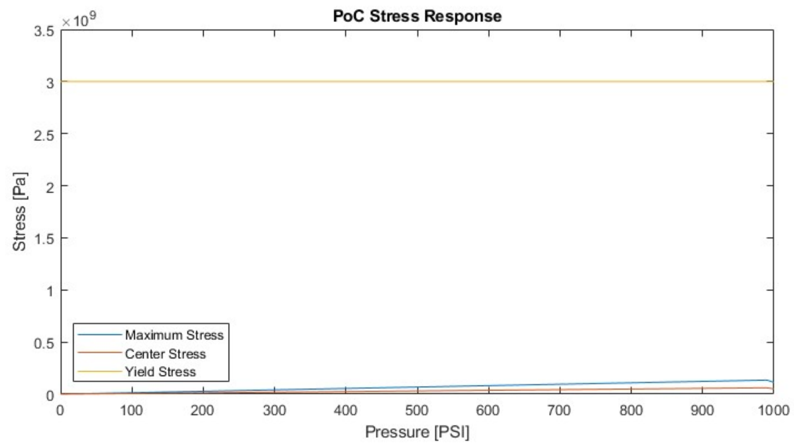
PoC Stress Response
×10^9
Stress [Pa]
Maximum Stress
Center Stress
Yield Stress
Pressure [PSI]

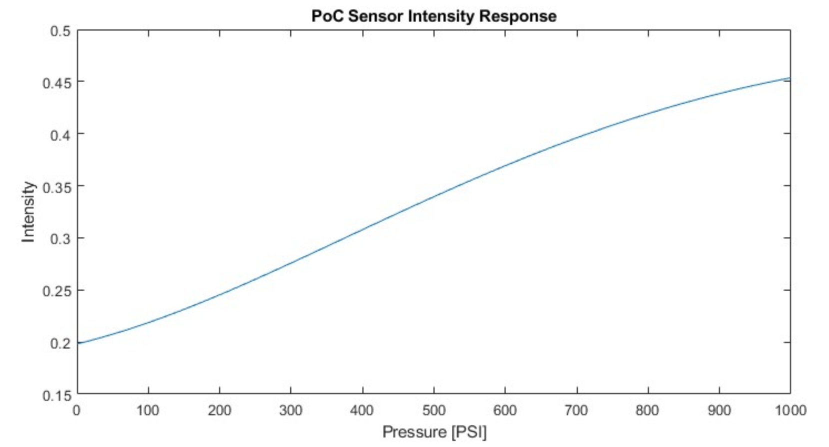
PoC Sensor Intensity Response
Intensity
Pressure [PSI]

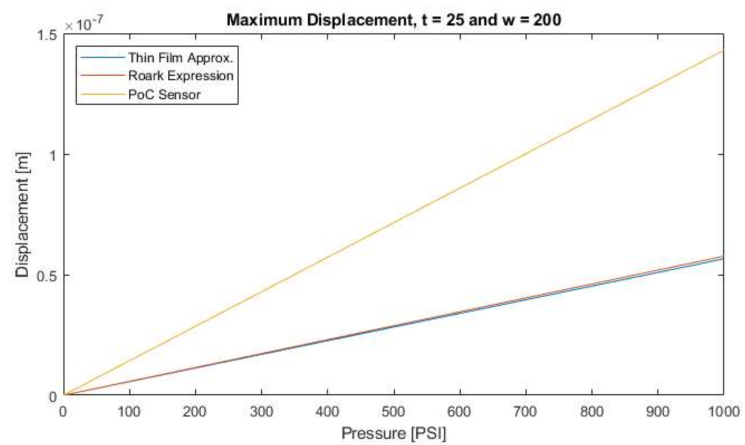
Maximum Displacement, t = 25 and w = 200
×10⁻⁷
Displacement [m]
Pressure [PSI]
Thin Film Approx.
Roark Expression
PoC Sensor

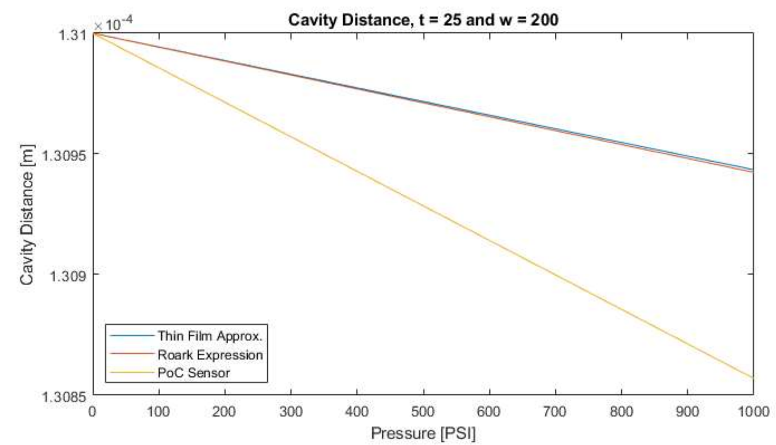
Cavity Distance, t = 25 and w = 200
×10⁻⁴
Cavity Distance [m]
Pressure [PSI]
Thin Film Approx.
Roark Expression
PoC Sensor

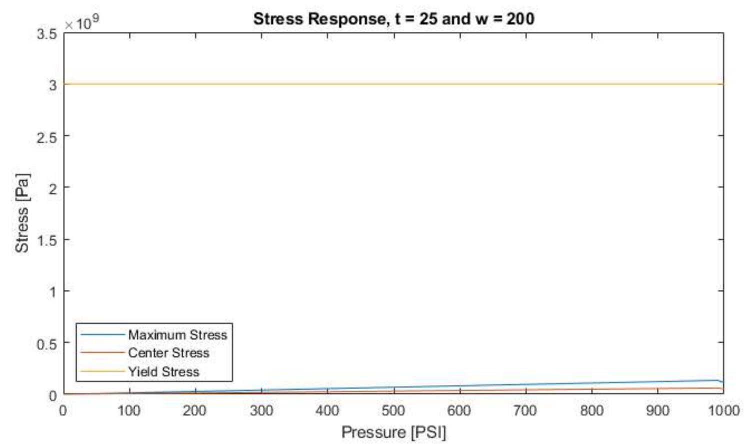
Stress Response, t = 25 and w = 200
×10⁹
Stress [Pa]
Pressure [PSI]
Maximum Stress
Center Stress
Yield Stress

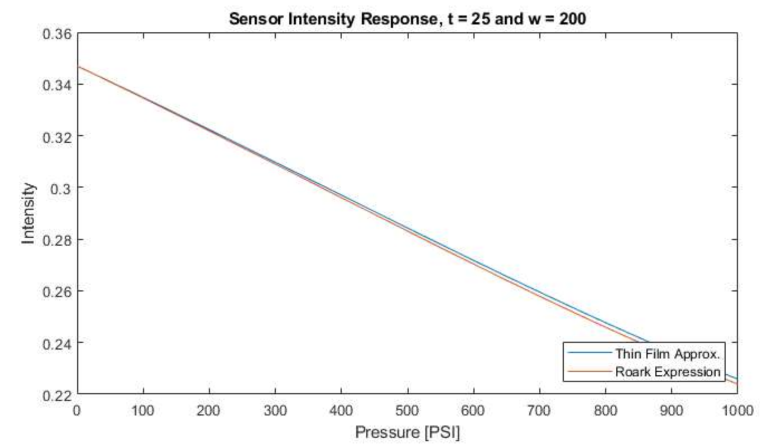
Sensor Intensity Response, t = 25 and w = 200
Intensity
Pressure [PSI]
Thin Film Approx.
Roark Expression

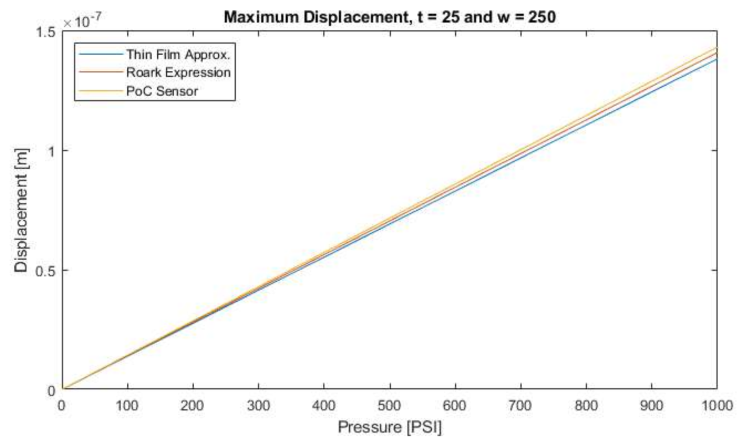
Maximum Displacement, t = 25 and w = 250
×10-7
Displacement [m]
Pressure [PSI]
Thin Film Approx.
Roark Expression
PoC Sensor

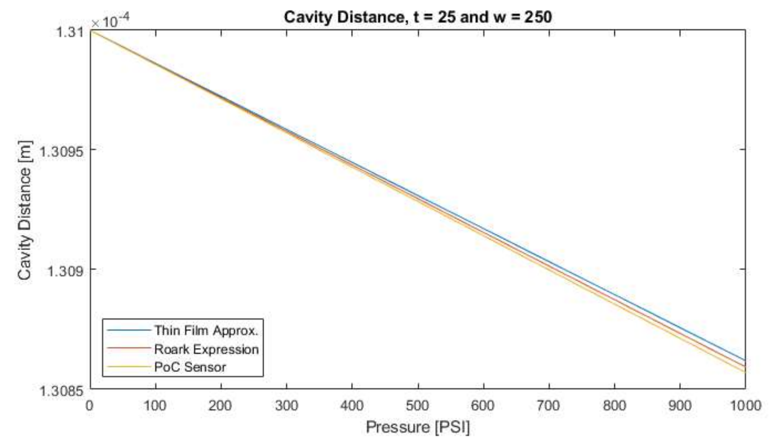
Cavity Distance, t = 25 and w = 250
×10-4
Cavity Distance [m]
Pressure [PSI]
Thin Film Approx.
Roark Expression
PoC Sensor

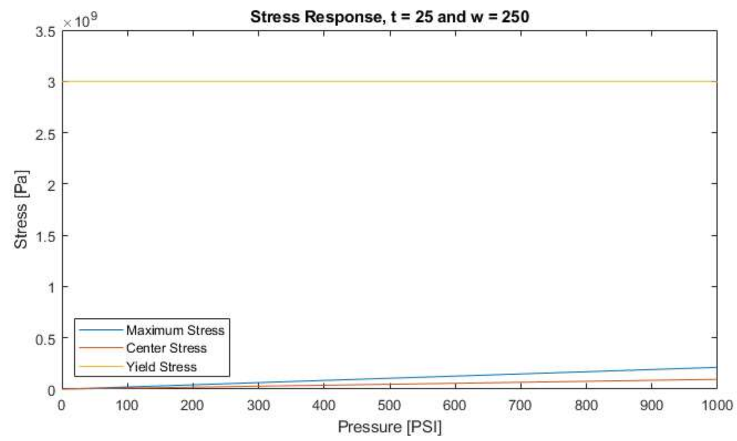
Stress Response, t = 25 and w = 250
×109
Stress [Pa]
Pressure [PSI]
Maximum Stress
Center Stress
Yield Stress

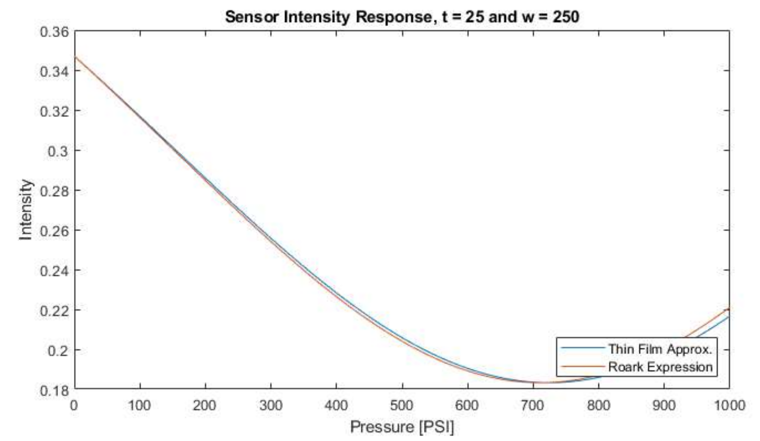
Sensor Intensity Response, t = 25 and w = 250
Intensity
Pressure [PSI]
Thin Film Approx.
Roark Expression

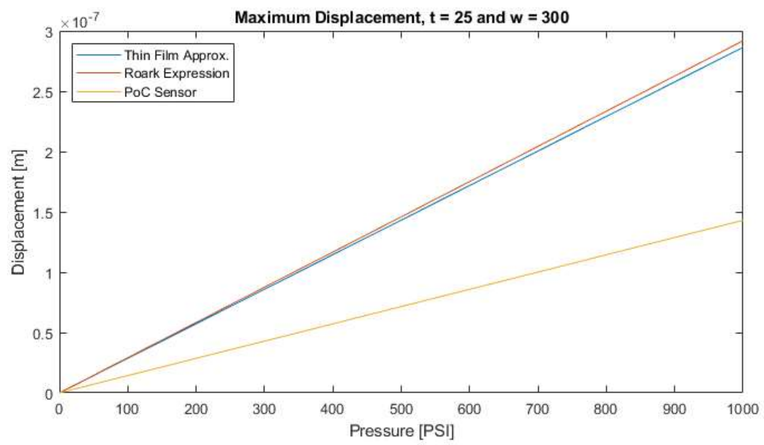
Maximum Displacement, t = 25 and w = 300
Thin Film Approx.
Roark Expression
PoC Sensor
Displacement [m]
Pressure [PSI]

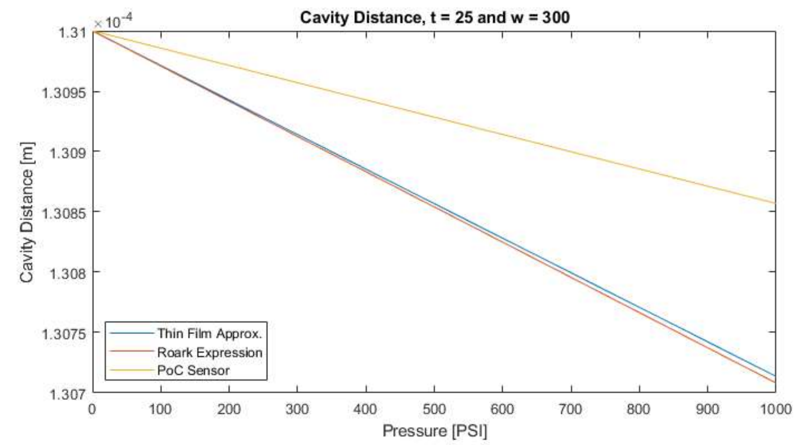
Cavity Distance, t = 25 and w = 300
Thin Film Approx.
Roark Expression
PoC Sensor
Cavity Distance [m]
Pressure [PSI]

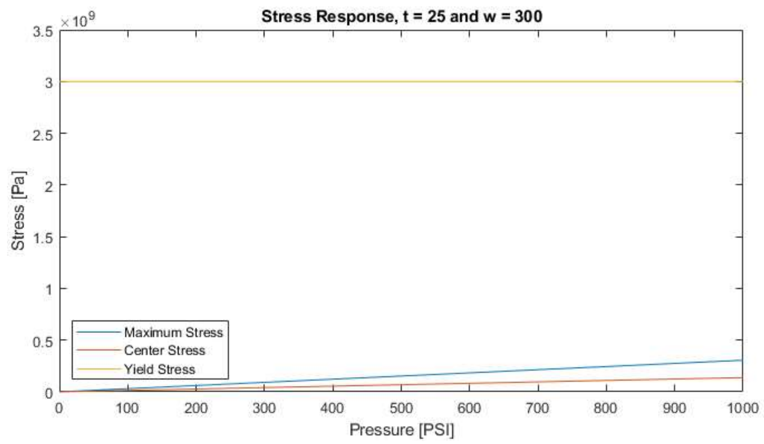
Stress Response, t = 25 and w = 300
Maximum Stress
Center Stress
Yield Stress
Stress [Pa]
Pressure [PSI]

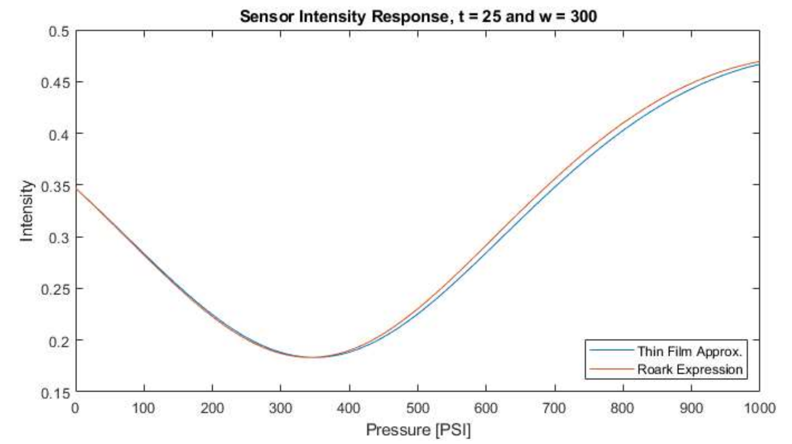
Sensor Intensity Response, t = 25 and w = 300
Thin Film Approx.
Roark Expression
Intensity
Pressure [PSI]

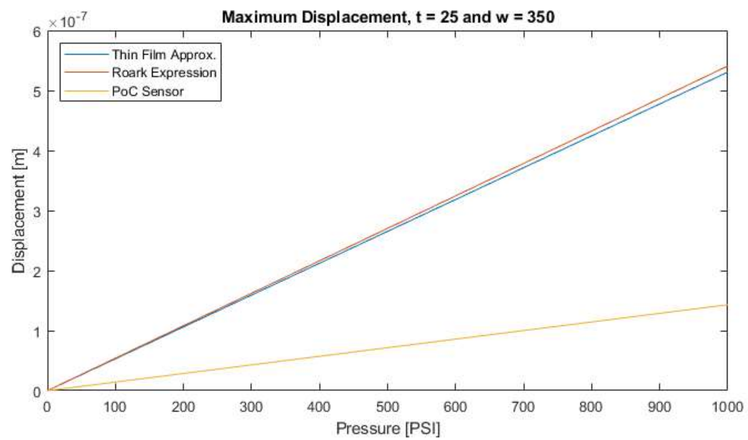
Maximum Displacement, t = 25 and w = 350
Displacement [m]
Pressure [PSI]
Thin Film Approx.
Roark Expression
PoC Sensor

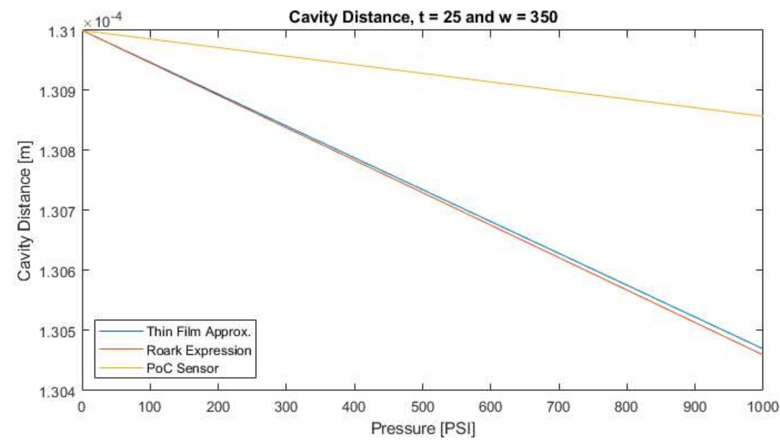
Cavity Distance, t = 25 and w = 350
Cavity Distance [m]
Pressure [PSI]
Thin Film Approx.
Roark Expression
PoC Sensor

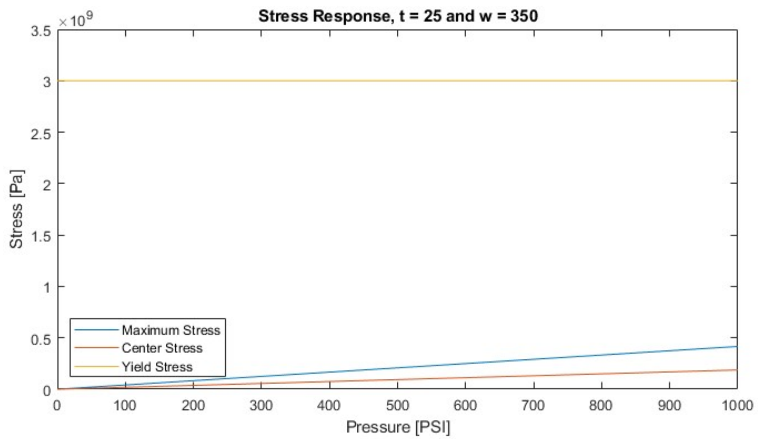
Stress Response, t = 25 and w = 350
Stress [Pa]
Pressure [PSI]
Maximum Stress
Center Stress
Yield Stress

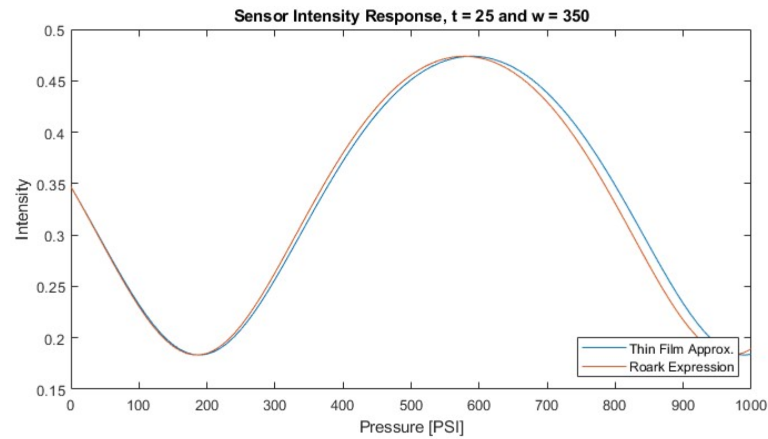
Sensor Intensity Response, t = 25 and w = 350
Intensity
Pressure [PSI]
Thin Film Approx.
Roark Expression

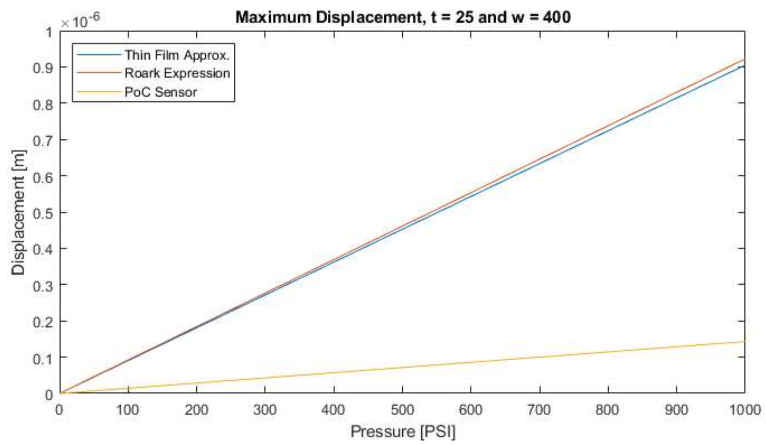
Maximum Displacement, t = 25 and w = 400
× 10^-6
Displacement [m]
Pressure [PSI]
Thin Film Approx.
Roark Expression
PoC Sensor

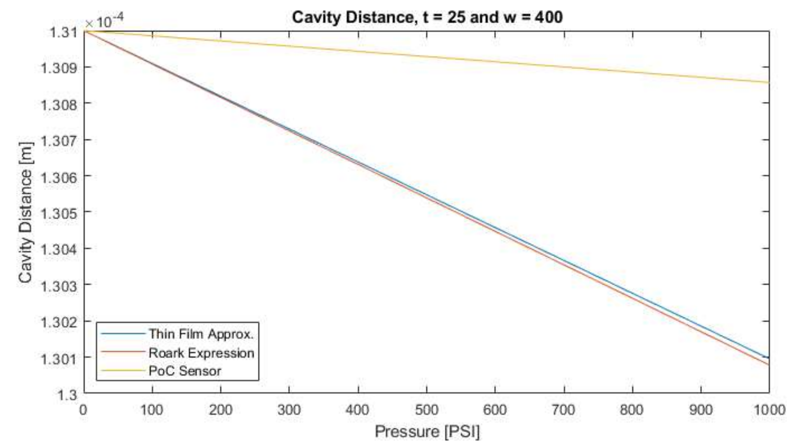
Cavity Distance, t = 25 and w = 400
× 10^-4
Cavity Distance [m]
Pressure [PSI]
Thin Film Approx.
Roark Expression
PoC Sensor

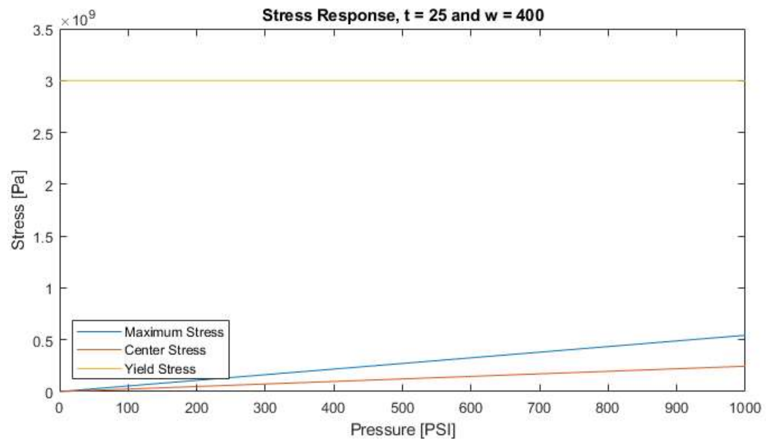
Stress Response, t = 25 and w = 400
× 10^9
Stress [Pa]
Pressure [PSI]
Maximum Stress
Center Stress
Yield Stress

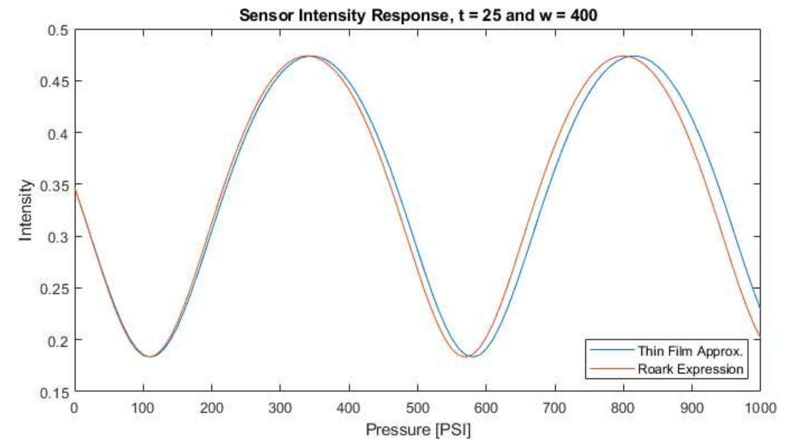
Sensor Intensity Response, t = 25 and w = 400
Intensity
Pressure [PSI]
Thin Film Approx.
Roark Expression

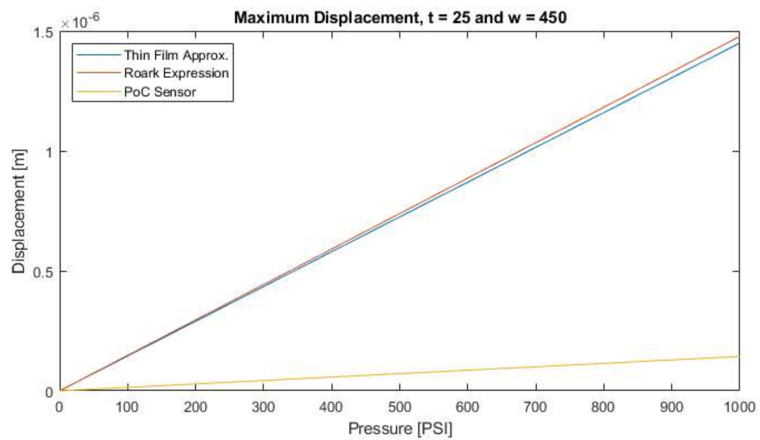
Maximum Displacement, t = 25 and w = 450
$\times 10^{-6}$
Displacement [m]
Pressure [PSI]
Thin Film Approx.
Roark Expression
PoC Sensor

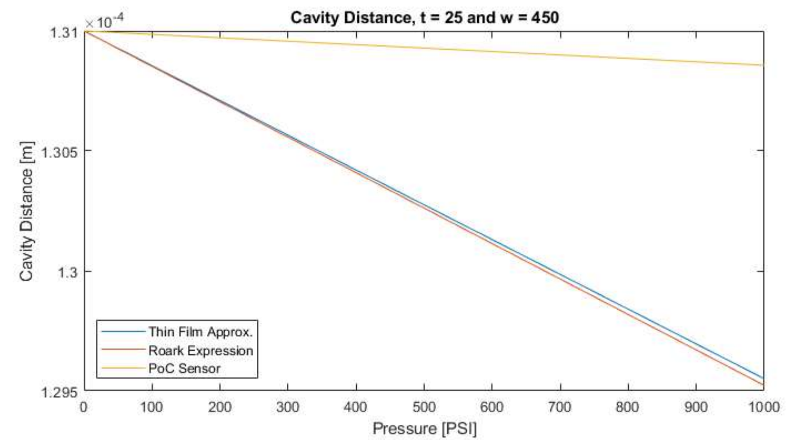
Cavity Distance, t = 25 and w = 450
$\times 10^{-4}$
Cavity Distance [m]
Pressure [PSI]
Thin Film Approx.
Roark Expression
PoC Sensor

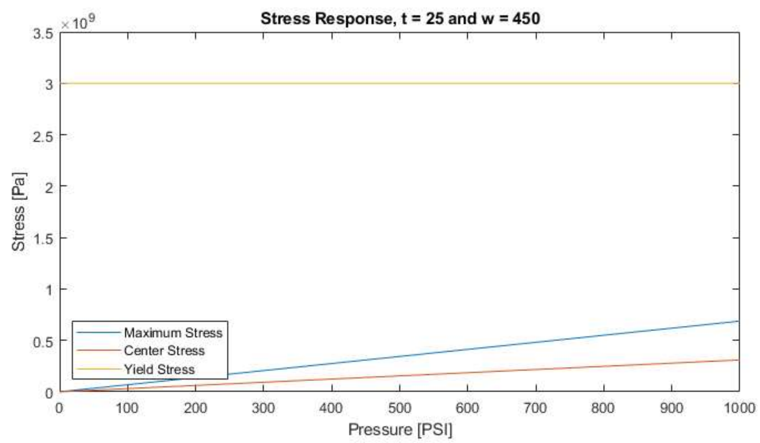
Stress Response, t = 25 and w = 450
$\times 10^{9}$
Stress [Pa]
Pressure [PSI]
Maximum Stress
Center Stress
Yield Stress

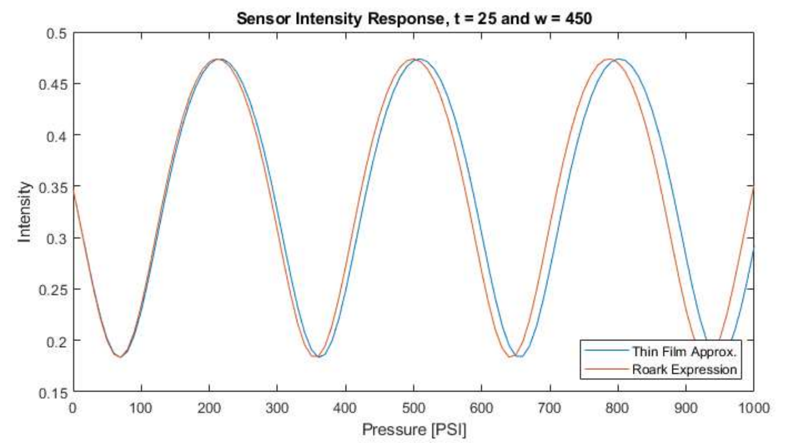
Sensor Intensity Response, t = 25 and w = 450
Intensity
Pressure [PSI]
Thin Film Approx.
Roark Expression

Appendix D – Temperature Dependence of Sensor Response

In the following figures, the impact of temperature on the PoC device is examined using the same metrics as presented in Appendix C. A similar set of graphs; showing the deflection, cavity distance and optical intensity are presented; followed by the maximum displacement of the membrane at various temperatures while the system is held at a constant pressure of 1000 PSI. Finally, a visualization of the change of material properties in silicon with respect to temperature is shown.

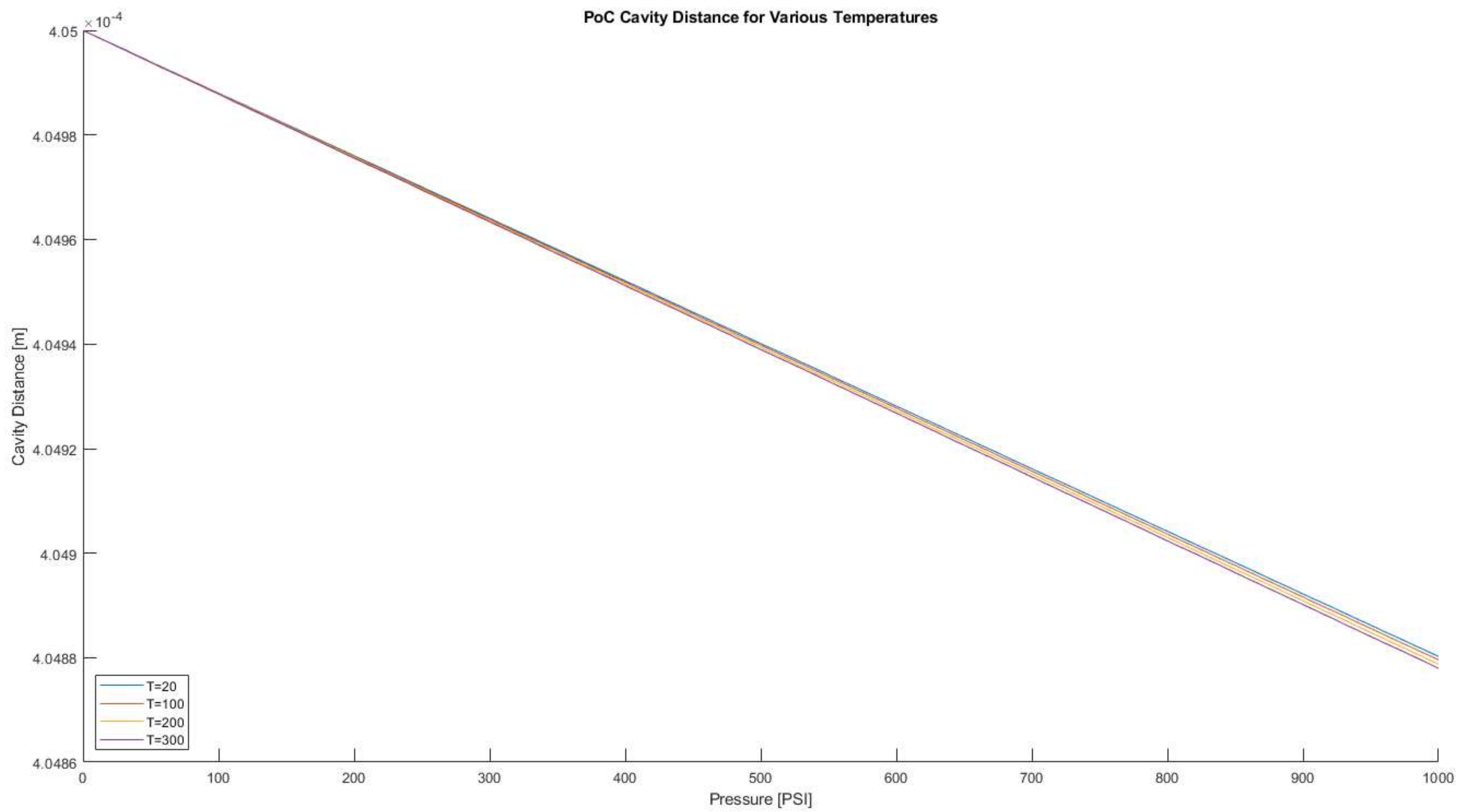
PoC Cavity Distance for Various Temperatures
×10^-4
4.05
4.0498
4.0496
4.0494
4.0492
4.049
4.0488
4.0486
Cavity Distance [m]
T=20
T=100
T=200
T=300
0
100
200
300
400
500
600
700
800
900
1000
Pressure [PSI]

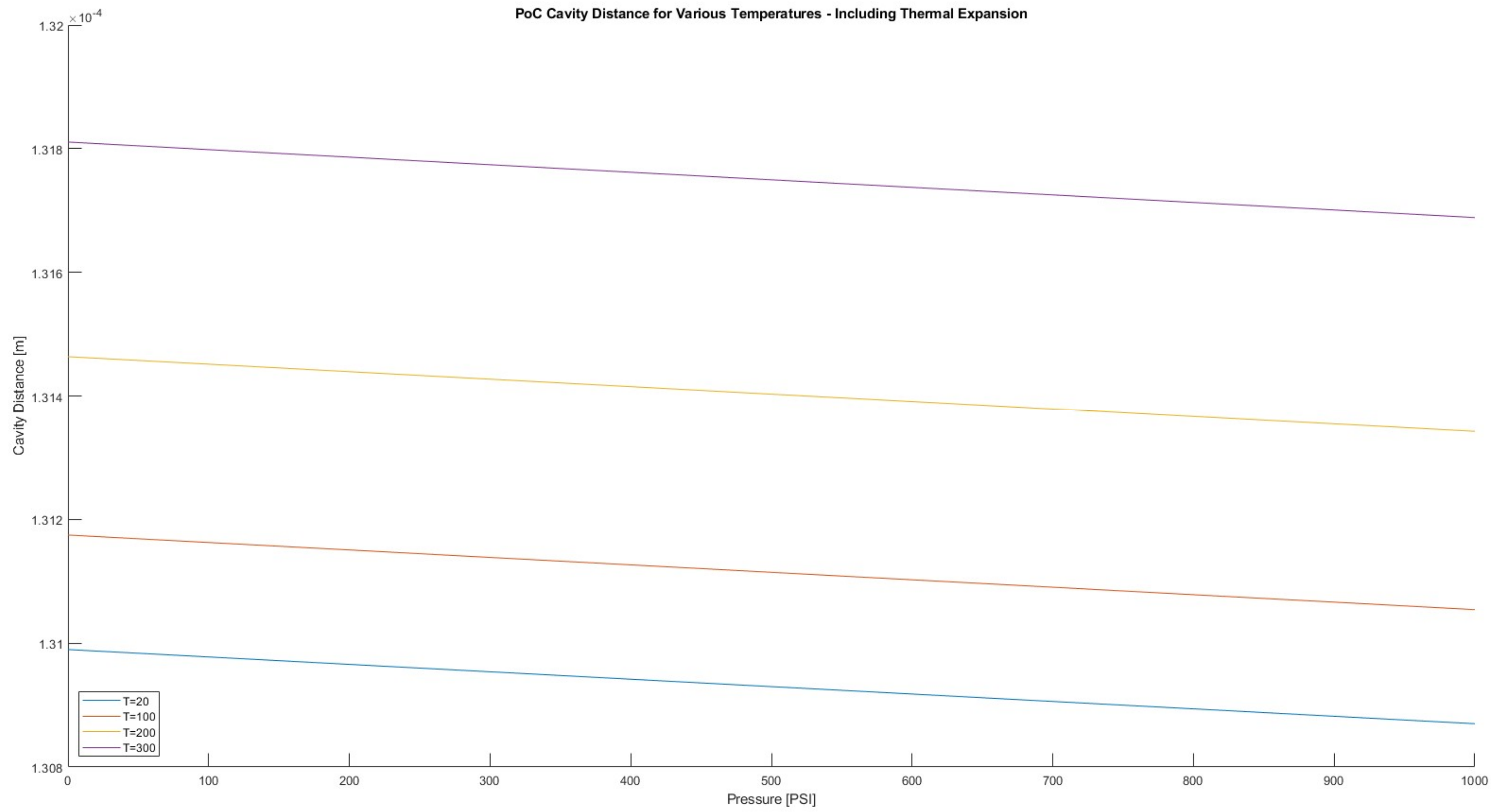
PoC Cavity Distance for Various Temperatures - Including Thermal Expansion
×10^-4
1.32
1.318
1.316
1.314
1.312
1.31
1.308
Cavity Distance [m]
T=20
T=100
T=200
T=300
0
100
200
300
400
500
600
700
800
900
1000
Pressure [PSI]

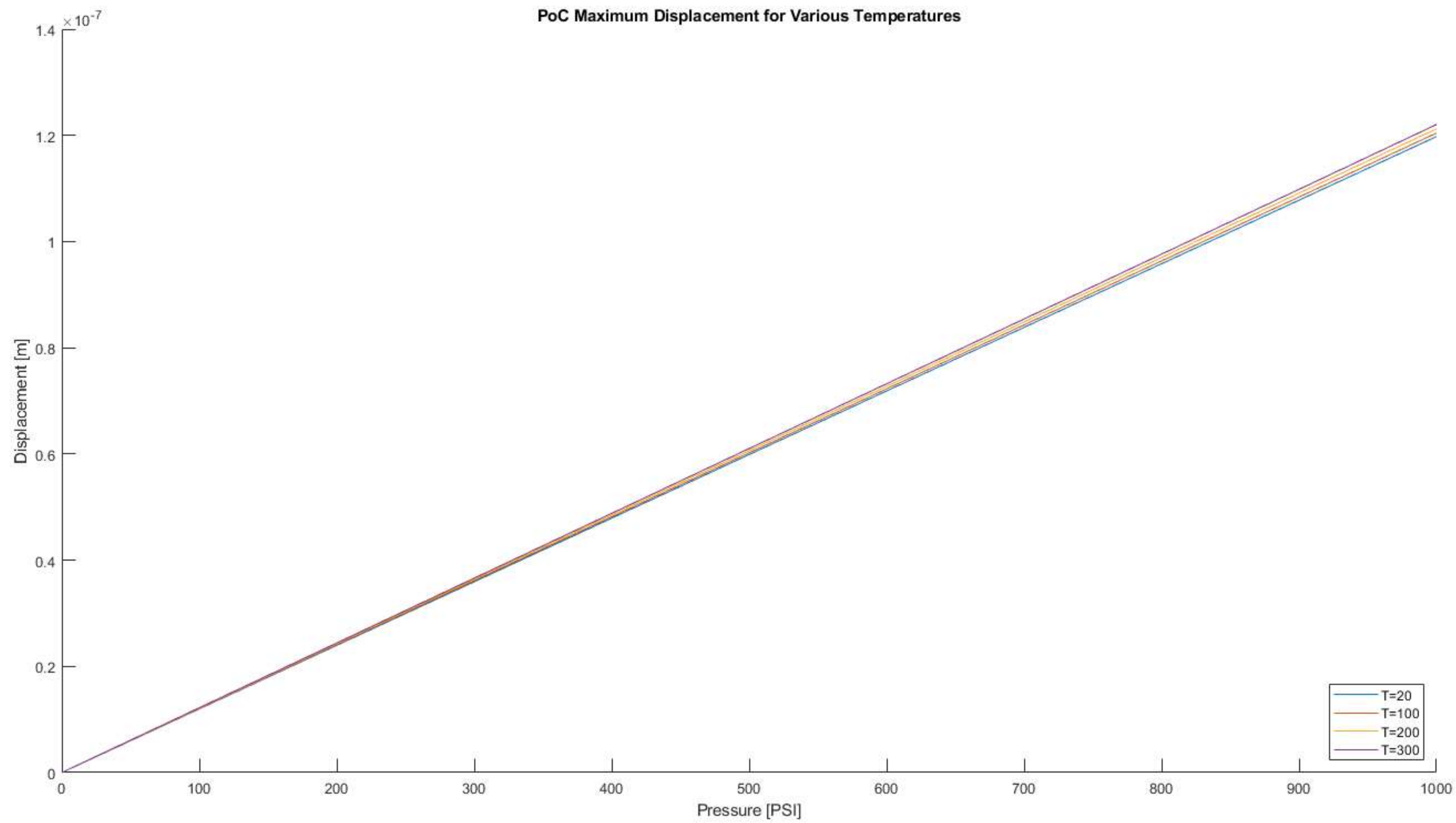
PoC Maximum Displacement for Various Temperatures
Displacement [m]
Pressure [PSI]
×10^-7
T=20
T=100
T=200
T=300
0
0.2
0.4
0.6
0.8
1
1.2
1.4
0
100
200
300
400
500
600
700
800
900
1000

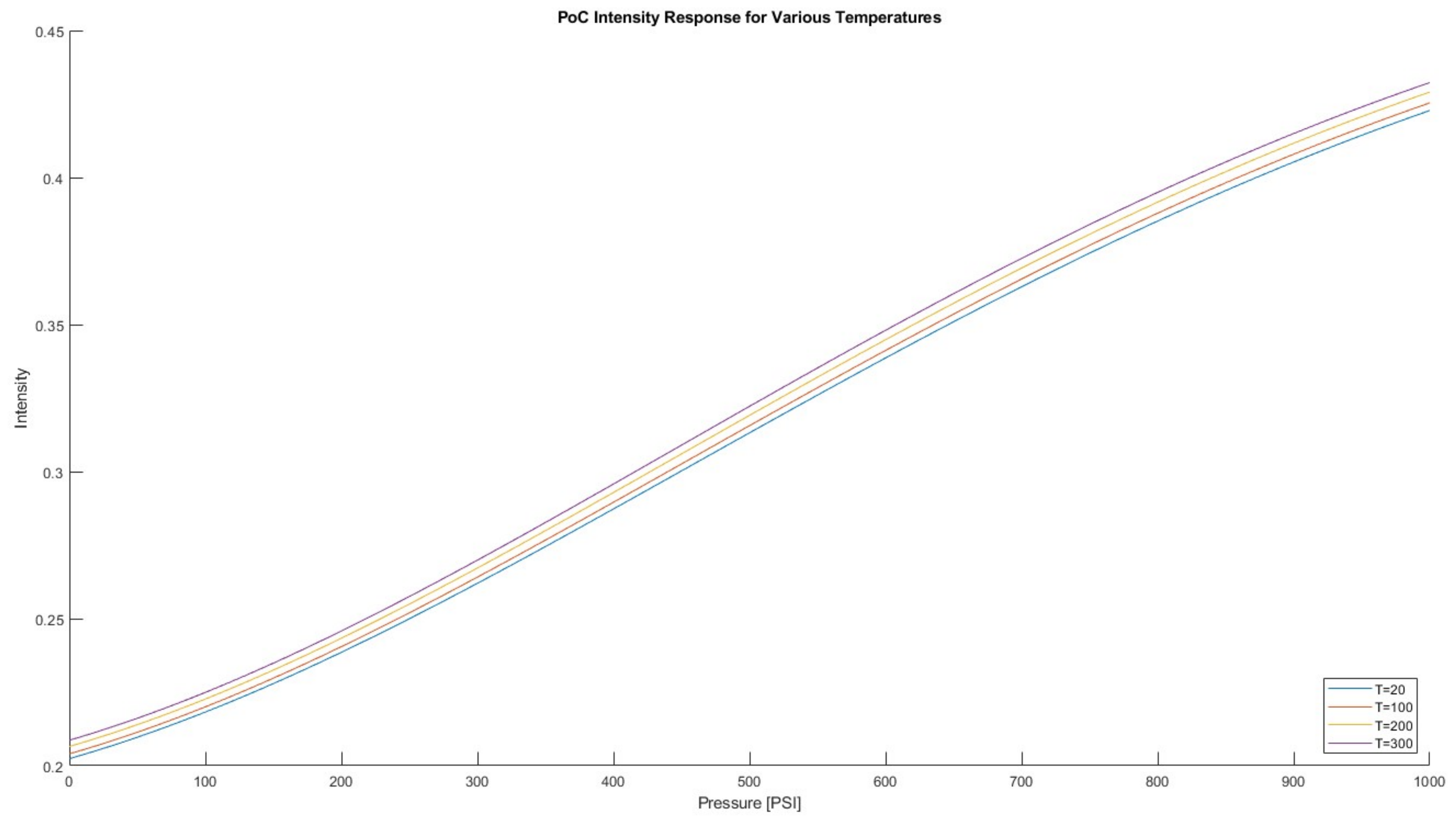

PoC Intensity Response for Various Temperatures
0.45
0.4
0.35
0.3
0.25
0.2
Intensity
0
100
200
300
400
500
600
700
800
900
1000
Pressure [PSI]
T=20
T=100
T=200
T=300

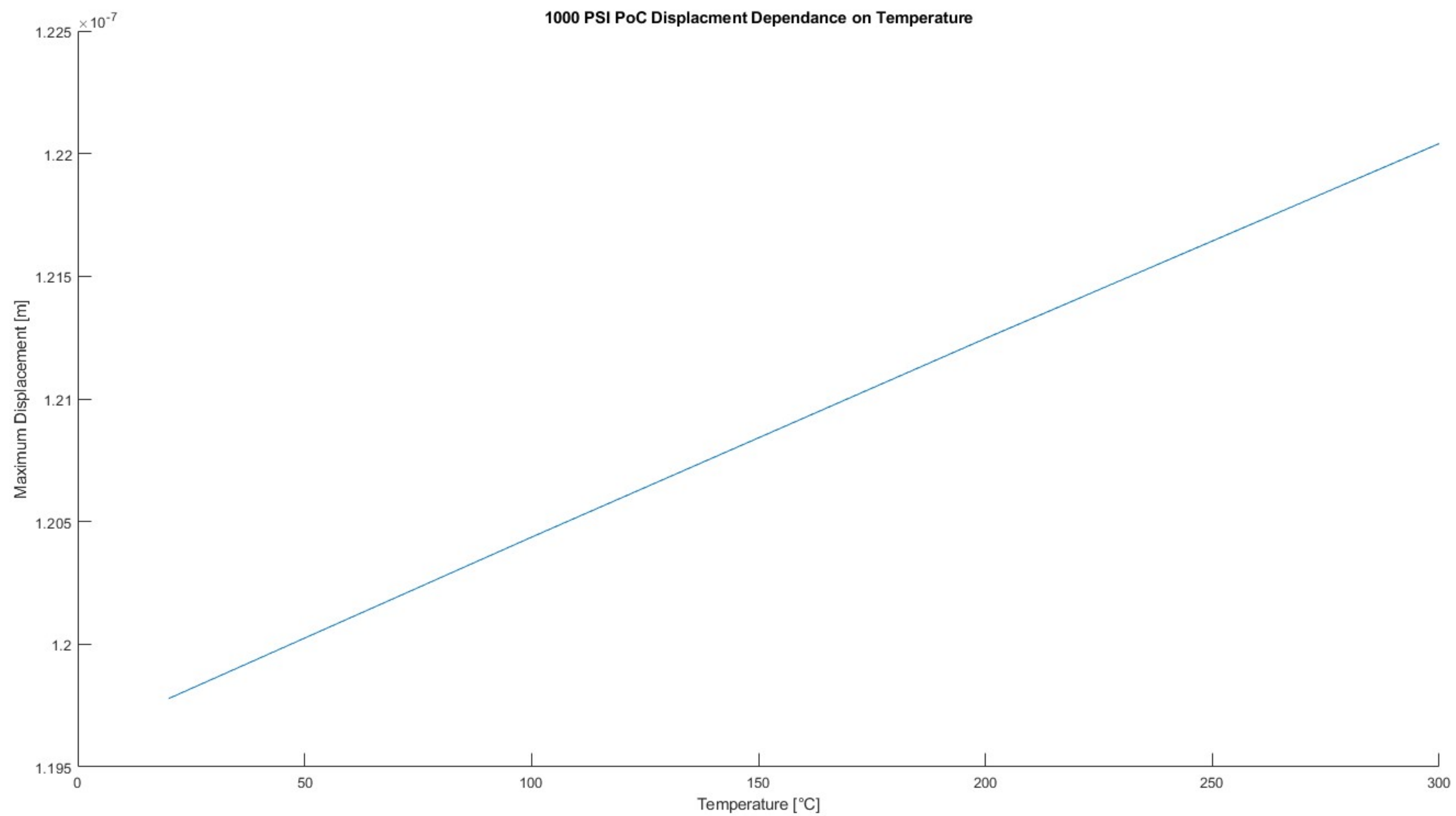
1000 PSI PoC Displacment Dependance on Temperature
×10^-7
1.225
1.22
1.215
1.21
1.205
1.2
1.195
Maximum Displacement [m]
0
50
100
150
200
250
300
Temperature [°C]

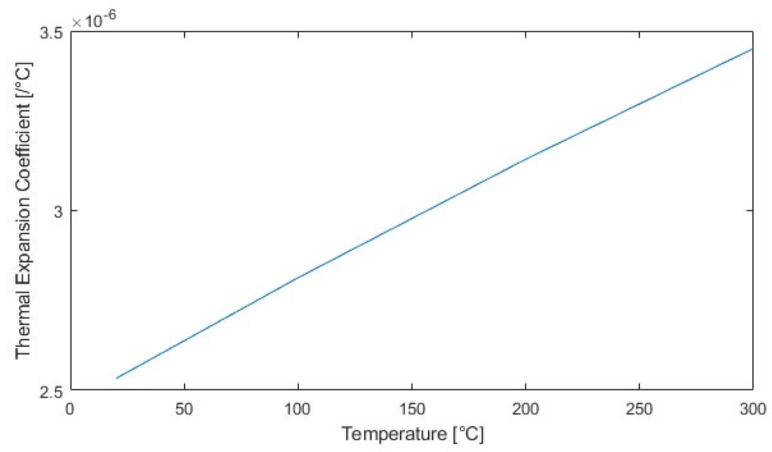
×10^-6
3.5
3
2.5
Thermal Expansion Coefficient [/°C]
0
50
100
150
200
250
300
Temperature [°C]

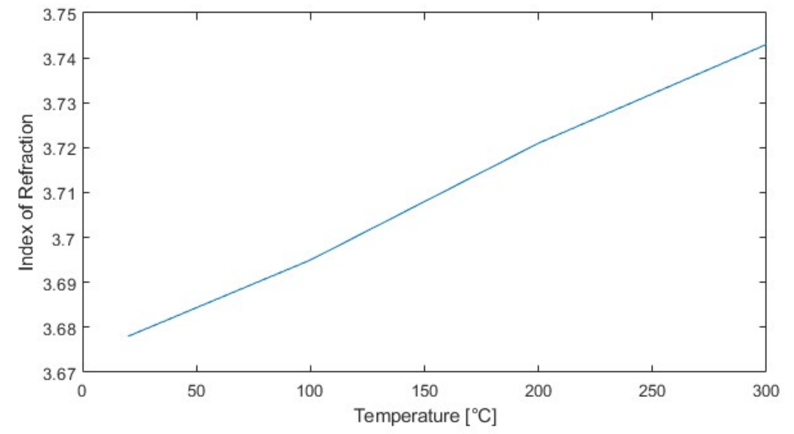
3.75
3.74
3.73
3.72
3.71
3.7
3.69
3.68
3.67
Index of Refraction
0
50
100
150
200
250
300
Temperature [°C]

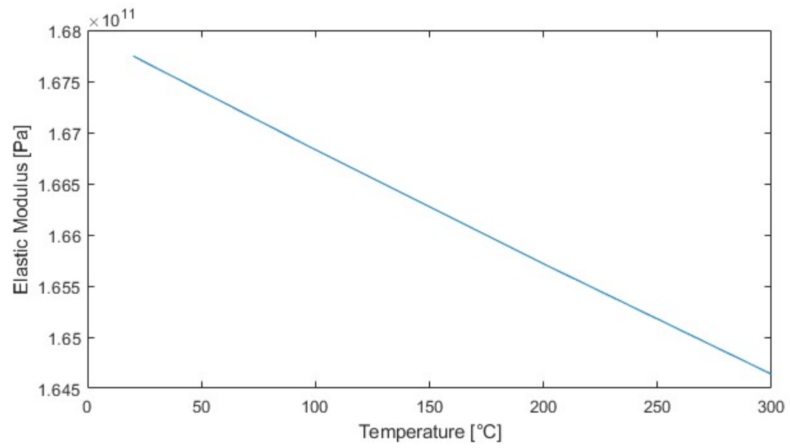
×10^11
1.68
1.675
1.67
1.665
1.66
1.655
1.65
1.645
Elastic Modulus [Pa]
0
50
100
150
200
250
300
Temperature [°C]

Appendix E - Sensor Housing Drawing

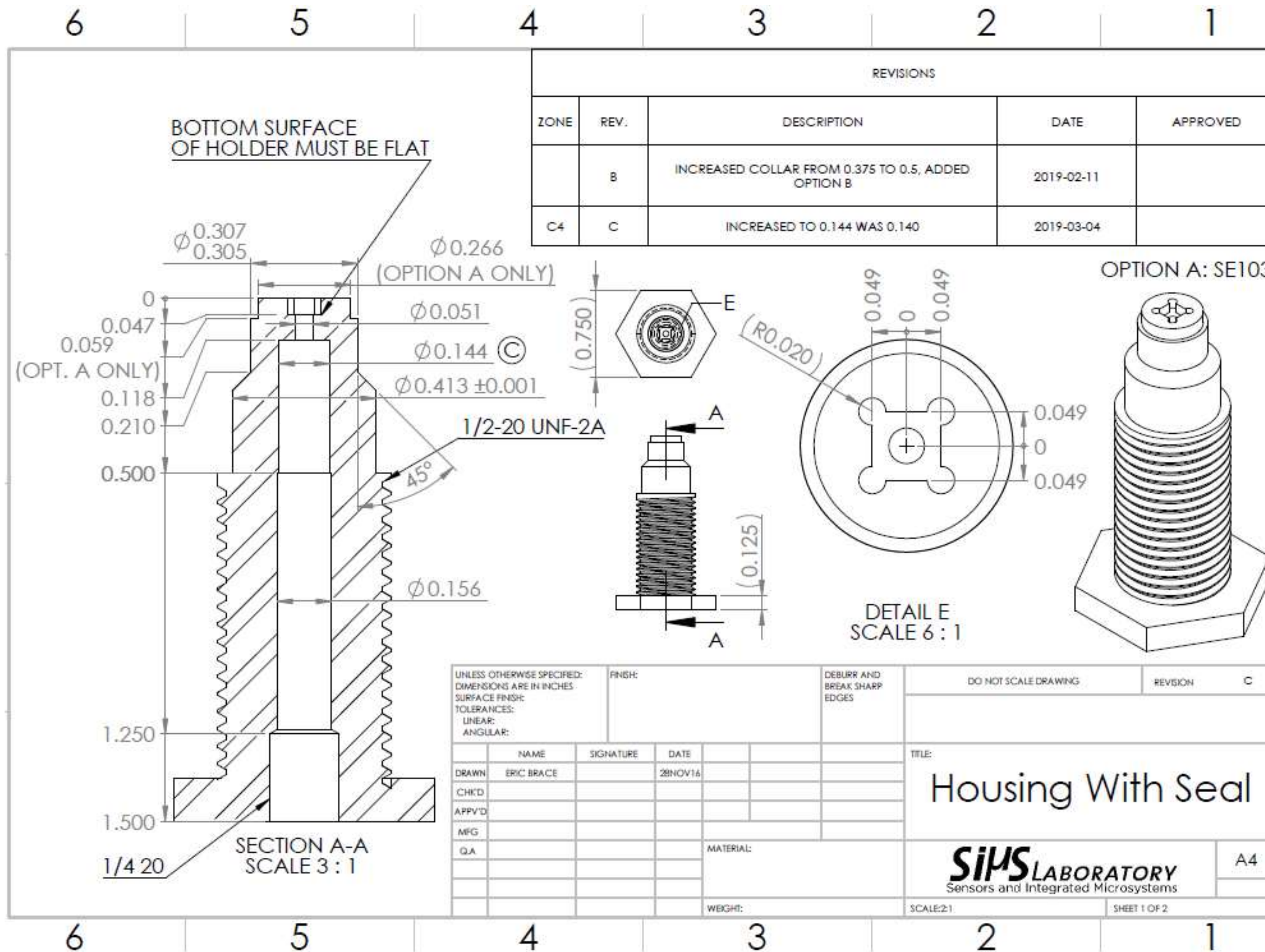

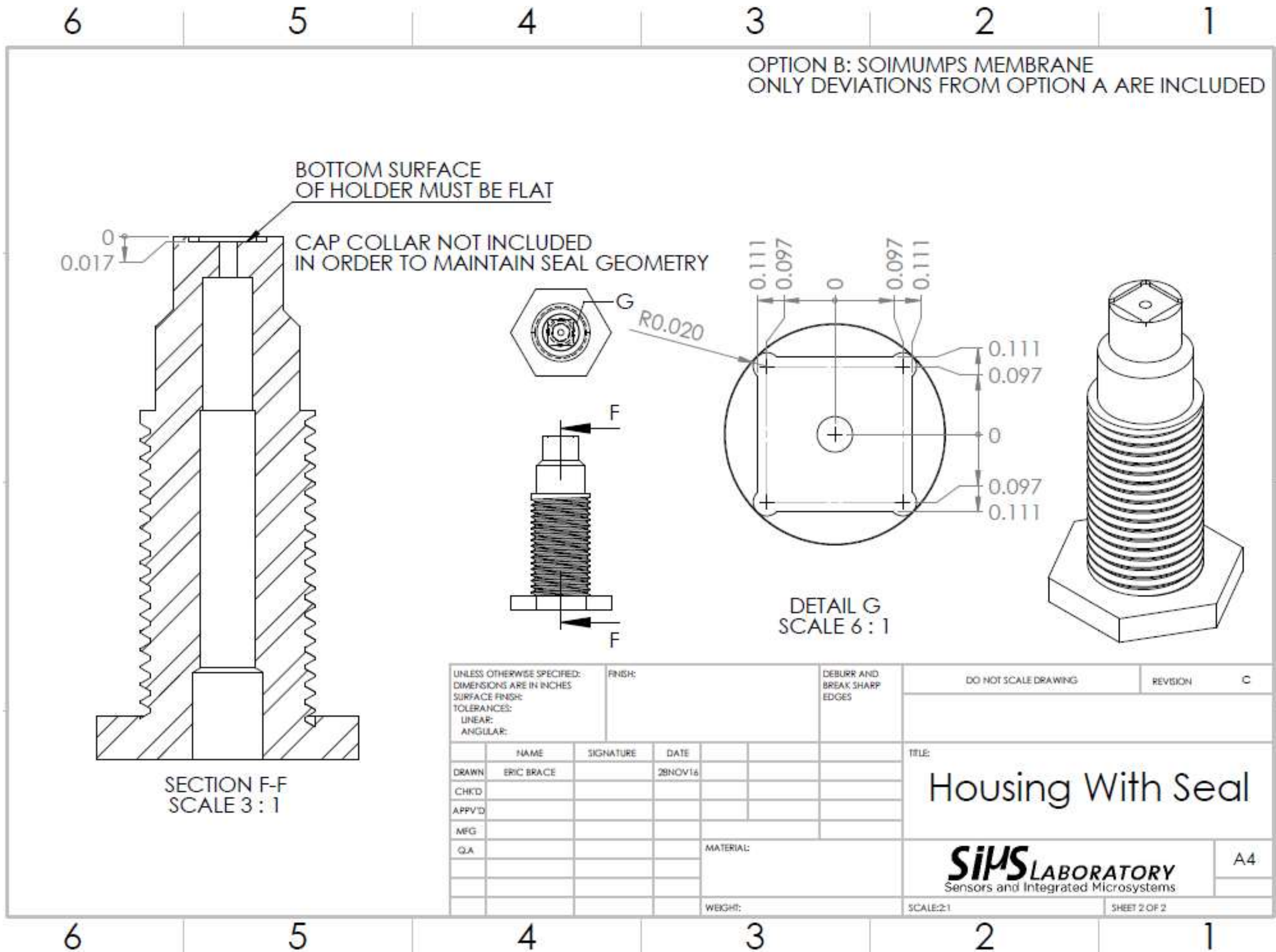

OPTION B: SOIMUMPS MEMBRANE
ONLY DEVIATIONS FROM OPTION A ARE INCLUDED
BOTTOM SURFACE
OF HOLDER MUST BE FLAT
CAP COLLAR NOT INCLUDED
IN ORDER TO MAINTAIN SEAL GEOMETRY
0
0.017
G
R0.020
0.111
0.097
0
0.097
0.111
F
F
SECTION F-F
SCALE 3 : 1
DETAIL G
SCALE 6 : 1
UNLESS OTHERWISE SPECIFIED:
DIMENSIONS ARE IN INCHES
SURFACE FINISH:
TOLERANCES:
LINEAR:
ANGULAR:
FINISH:
DEBURR AND
BREAK SHARP
EDGES
DO NOT SCALE DRAWING
REVISION
C
NAME
SIGNATURE
DATE
DRAWN
ERIC BRACE
28NOV16
CHK'D
APPV'D
MFG
Q.A
MATERIAL:
WEIGHT:
TITLE:
Housing With Seal
SiMS LABORATORY
Sensors and Integrated Microsystems
A4
SCALE:2:1
SHEET 2 OF 2

Appendix F – Fiber Locator Drawing

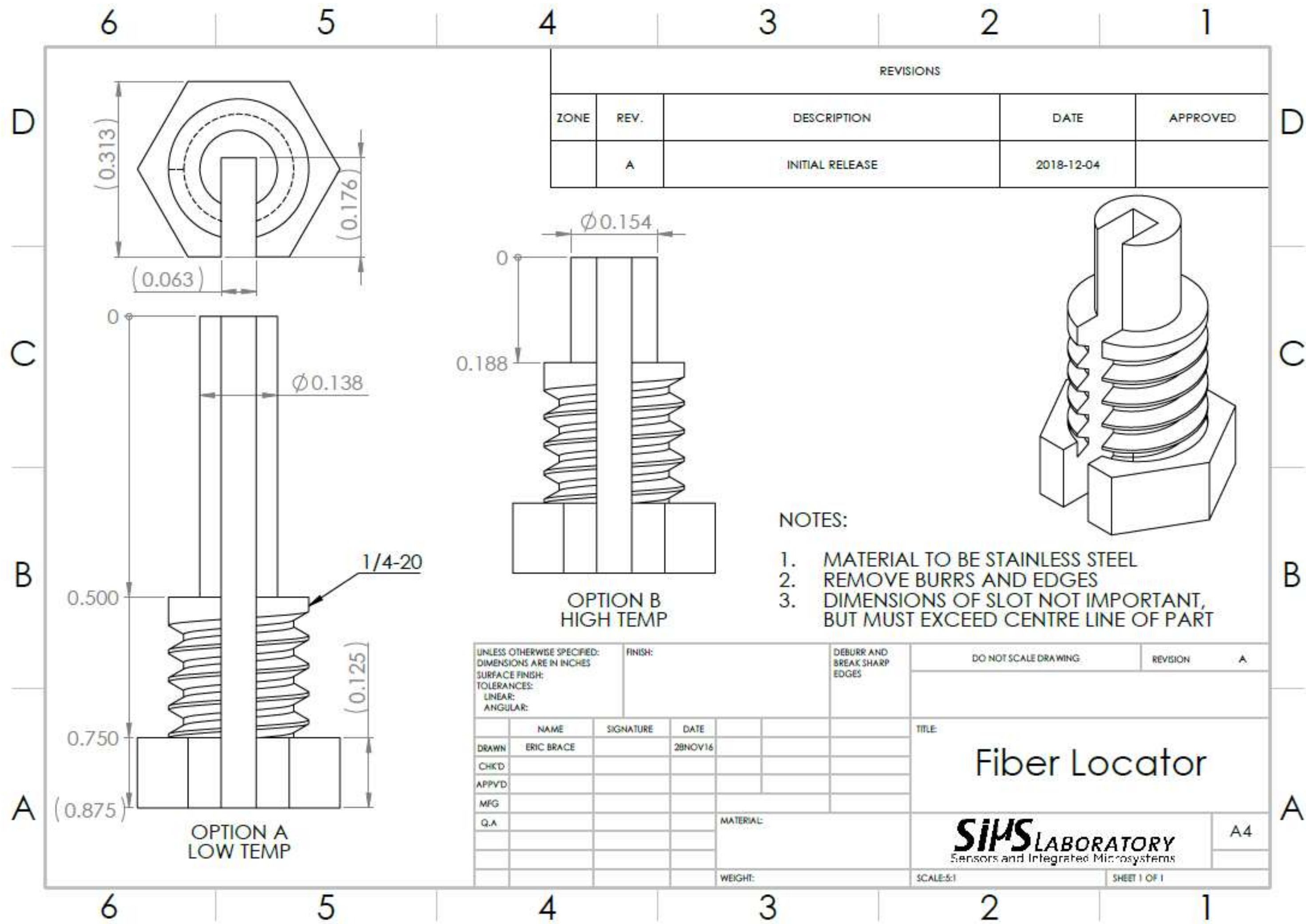

Bibliography

This document was created with the help of: Vogt, C. 1999. Creating Long Documents using Microsoft Word. Published on the Web at the University of Waterloo.

[1] Y.-J. Rao, “Recent progress in fiber-optic extrinsic Fabry–Perot interferometric sensors,” *Opt. Fiber Technol.*, vol. 12, no. 3, pp. 227–237, Jul. 2006.

[2] A. G. Mignani and F. Baldini, “Biomedical sensors using optical fibres,” *Rep. Prog. Phys.*, vol. 59, no. 1, p. 1, 1996.

[3] P. French, G. Krijnen, and F. Roozeboom, “Precision in harsh environments,” *Microsyst. Nanoeng.*, vol. 2, no. 1, Dec. 2016.

[4] H. Karbasi and H. Reiser, “Smart Mold: Real-Time in-Cavity Data Acquisition,” in *First Annual Technical Showcase & Third Annual Workshop, Canada*, 2006.

[5] J. E. Suarez, B. E. Johnson, and B. El-Kareh, “Thermal stability of polysilicon resistors,” *IEEE Trans. Compon. Hybrids Manuf. Technol.*, vol. 15, no. 3, pp. 386–392, Jun. 1992.

[6] “High Temperature Pressure Transducers, Ultra high Temperature, PX1004, PX1009.” [Online]. Available: https://www.omega.ca/pptst_eng/PX1004.html. [Accessed: 14-Oct-2018].

[7] P. C. Meza, “Study of a MEMS fiber-optic pressure sensor based on Optical Interferometry,” MASc, University of Waterloo.

[8] “SE103 Sensor Dies for General Purpose | BCM Sensor.” [Online]. Available: https://www.bcmsensor.com/products/pressure-sensor-dies/model-se103-sensor-dies-for-general-application/. [Accessed: 19-May-2017].

[9] R. A. Wolthuis, G. L. Mitchell, E. Saaski, J. C. Hartl, and M. A. Afromowitz, “Development of medical pressure and temperature sensors employing optical spectrum modulation,” *IEEE Trans. Biomed. Eng.*, vol. 38, no. 10, pp. 974–981, Oct. 1991.

[10] T. Giallorenzi *et al.*, “Optical fiber sensor technology,” *IEEE J. Quantum Electron.*, vol. 18, no. 4, pp. 626–665, Apr. 1982.

[11] E. Cibula, D. Donlagic, and C. Stropnik, “Miniature fiber optic pressure sensor for medical applications,” in *Proceedings of IEEE Sensors*, 2002, vol. 1, pp. 711–714 vol.1.

[12] A. S. Fiorillo, C. D. Critello, and S. A. Pullano, “Theory, technology and applications of piezoresistive sensors: A review,” *Sens. Actuators Phys.*, vol. 281, pp. 156–175, Oct. 2018.

[13] B. H. Lee *et al.*, “Interferometric Fiber Optic Sensors,” *Sensors*, vol. 12, no. 3, pp. 2467–2486, Feb. 2012.

[14] J. Wyant, “Multiple Beam Interference.” [Online]. Available: http://wyant.optics.arizona.edu/MultipleBeamInterference/MultipleBeamInterferenceNotes.html. [Accessed: 24-Mar-2017].

[15] X. Wang, B. Li, O. L. Russo, H. T. Roman, K. K. Chin, and K. R. Farmer, “Diaphragm design guidelines and an optical pressure sensor based on MEMS technique,” *Microelectron. J.*, vol. 37, no. 1, pp. 50–56, Jan. 2006.

[16] G. C. Hill *et al.*, “SU-8 MEMS Fabry-Perot pressure sensor,” *Sens. Actuators Phys.*, vol. 138, no. 1, pp. 52–62, Jul. 2007.

[17] W. J. Pulliam, P. M. Russler, and R. S. Fielder, “High-temperature high-bandwidth fiber optic MEMS pressure-sensor technology for turbine engine component testing,” in *Environmental and Industrial Sensing*, 2002, vol. 4578, pp. 229–238.

[18] Warren C. Young, Richard G. Budynas, Ali M. Sadegh, “Roark’s Formulas for Stress and Strain, Eighth Edition,” in *The McGraw-Hill Companies, Inc*, 2012, p. 532.

[19] Y. Zhu and A. Wang, “Miniature fiber-optic pressure sensor,” *IEEE Photonics Technol. Lett.*, vol. 17, no. 2, pp. 447–449, Feb. 2005.

[20] J. Yi, “Adhesive-Free Bonding of Monolithic Sapphire for Pressure Sensing in Extreme Environments,” *Sensors*, vol. 18, no. 8, Aug. 2018.

[21] M. Li, M. Wang, and H. Li, “Optical MEMS pressure sensor based on Fabry-Perot interferometry,” *Opt. Express*, vol. 14, no. 4, p. 1497, 2006.

[22] K. Totsu, Y. Haga, and M. Esashi, “Ultra-miniature fiber-optic pressure sensor using white light interferometry,” *J. Micromechanics Microengineering*, vol. 15, no. 1, pp. 71–75, Jan. 2005.

[23] G. C. Fang, P. G. Jia, Q. Cao, and J. J. Xiong, “MEMS fiber-optic Fabry-Perot pressure sensor for high temperature application,” 2016, p. 101552H.

[24] P. Jia *et al.*, “Batch-producible MEMS fiber-optic Fabry–Perot pressure sensor for high-temperature application,” *Appl. Opt.*, vol. 57, no. 23, p. 6687, Aug. 2018.

[25] J. Liu *et al.*, “Fiber-optic Fabry–Perot pressure sensor based on low-temperature co-fired ceramic technology for high-temperature applications,” *Appl. Opt.*, vol. 57, no. 15, p. 4211, May 2018.

[26] Q. Wang, L. Zhang, C. Sun, and Q. Yu, “Multiplexed Fiber-Optic Pressure and Temperature Sensor System for Down-Hole Measurement,” *IEEE Sens. J.*, vol. 8, no. 11, pp. 1879–1883, Nov. 2008.

[27] Y. Zhang, L. Yuan, X. Lan, A. Kaur, J. Huang, and H. Xiao, “High-temperature fiber-optic Fabry–Perot interferometric pressure sensor fabricated by femtosecond laser,” *Opt. Lett.*, vol. 38, no. 22, p. 4609, Nov. 2013.

[28] C. Wu, H. Y. Fu, K. K. Qureshi, B.-O. Guan, and H. Y. Tam, “High-pressure and high-temperature characteristics of a Fabry–Perot interferometer based on photonic crystal fiber,” *Opt. Lett.*, vol. 36, no. 3, p. 412, Feb. 2011.

[29] Q. Yu and X. Zhou, “Pressure sensor based on the fiber-optic extrinsic Fabry-Perot interferometer,” *Photonic Sens.*, vol. 1, no. 1, pp. 72–83, Mar. 2011.

[30] “Introduction to Charge-Coupled Devices (CCDs),” *Nikon’s MicroscopyU*. [Online]. Available: https://www.microscopyu.com/digital-imaging/introduction-to-charge-coupled-devices-ccds. [Accessed: 22-Mar-2017].

[31] J. Jiang *et al.*, “A polarized low-coherence interferometry demodulation algorithm by recovering the absolute phase of a selected monochromatic frequency,” *Opt. Express*, vol. 20, no. 16, pp. 18117–18126, 2012.

[32] Allen Cowen, Greg Hames, DeMaul Monk, Steve Wilcenski, and Busbee Hardy, “SOIMUMPs Design Handbook Rev. 8.” MEMSCAP Inc., 2011.

[33] M. A. Hopcroft, W. D. Nix, and T. W. Kenny, “What is the Young’s Modulus of Silicon?,” *J. Microelectromechanical Syst.*, vol. 19, no. 2, pp. 229–238, Apr. 2010.

[34] J. Jeong, S. Chung, S.-H. Lee, and D. Kwon, “Evaluation of elastic properties and temperature effects in Si thin films using an electrostatic microresonator,” *J. Microelectromechanical Syst.*, vol. 12, no. 4, pp. 524–530, Aug. 2003.

[35] T. Tsuchiya, T. Ikeda, A. Tsunematsu, K. Sugano, and O. Tabata, “Tensile Testing of Single-Crystal Silicon Thin Films at 600°C Using Infrared Radiation Heating,” *Sens. Mater.*, vol. 22, no. 1, p. 11, 2010.

[36] “EPO-TEK 353ND Data Sheet.” [Online]. Available: http://www.epotek.com/site/administrator/components/com_products/assets/files/Style_Uploads/353ND.pdf. [Accessed: 27-Nov-2018].

[37] “Datasheet_OPV314 series.pdf.” [Online]. Available: http://www.ttelectronics.com/sites/default/files/download-files/Datasheet_OPV314%20series.pdf. [Accessed: 15-Nov-2018].

[38] “FG105LCA-SpecSheet.” [Online]. Available: https://www.thorlabs.com/drawings/905805982b6bd1d1-09655CBA-B509-BA2B-4C1396FD287F7A0E/FG105LCA-SpecSheet.pdf. [Accessed: 20-Nov-2018].

[39] "UM22 100 Spec Sheet." [Online]. Available: https://www.thorlabs.com/drawings/905805982b6bd1d1-09655CBA-B509-BA2B-4C1396FD287F7A0E/UM22-100-SpecSheet.pdf. [Accessed: 20-Nov-2018].
[40] "Multimode Fiber Tutorial." [Online]. Available: https://www.thorlabs.com/newgrouppage9.cfm?objectgroup_id=10417. [Accessed: 13-Nov-2018].
[41] A. Ghannoum, P. Nieva, A. Yu, and A. Khajepour, "Development of Embedded Fiber-Optic Evanescent Wave Sensors for Optical Characterization of Graphite Anodes in Lithium-Ion Batteries," *ACS Appl. Mater. Interfaces*, vol. 9, no. 47, pp. 41284–41290, Nov. 2017.
[42] "Fiber Optic Detector - OPF480 Specification Sheet." [Online]. Available: http://www.ttelectronics.com/sites/default/files/download-files/OPF480_0.pdf?fbclid=IwAR3pWm5HE27bB-LtA8NMaWsAZwoJ9ZkFB-myNTNQJBFHl2aIj2BrwV7Q1p8. [Accessed: 15-Nov-2018].
[43] F. Xu *et al.*, "High-sensitivity Fabry–Perot interferometric pressure sensor based on a nanothick silver diaphragm," *Opt. Lett.*, vol. 37, no. 2, p. 133, Jan. 2012.
[44] Fastenal Engineering and Design Support, "Article - Screw Threads Design.pdf." [Online]. Available: https://www.fastenal.com/content/feds/pdf/Article%20-%20Screw%20Threads%20Design.pdf. [Accessed: 17-Nov-2018].
[45] "AISI Type 304 Stainless Steel Data Sheet." [Online]. Available: http://asm.matweb.com/search/SpecificMaterial.asp?bassnum=mq304a. [Accessed: 20-Nov-2018].
[46] G. Vuye, S. Fisson, V. Nguyen Van, Y. Wang, J. Rivory, and F. Abelès, "Temperature dependence of the dielectric function of silicon using in situ spectroscopic ellipsometry," *Thin Solid Films*, vol. 233, no. 1–2, pp. 166–170, Oct. 1993.
[47] "Refractive index of Si (Silicon) - Vuye-300C." [Online]. Available: https://refractiveindex.info/?shelf=main&book=Si&page=Vuye-300C. [Accessed: 03-Dec-2018].
[48] P. J. Burkhardt and R. F. Marvel, "Thermal Expansion of Sputtered Silicon Nitride Films," *J. Electrochem. Soc.*, vol. 116, no. 6, pp. 864–866, Jun. 1969.
[49] I. H. Malitson, "Interspecimen Comparison of the Refractive Index of Fused Silica," *J Opt Soc Am*, vol. 55, no. 10, pp. 1205–1209, 1965.
[50] Z.-Y. Wang, Q. Qiu, and S.-J. Shi, "Temperature dependence of the refractive index of optical fibers," *Chin. Phys. B*, vol. 23, no. 3, p. 034201, Mar. 2014.
[51] J. W. Marx and J. M. Sivertsen, "Temperature Dependence of the Elastic Moduli and Internal Friction of Silica and Glass," *J. Appl. Phys.*, vol. 24, no. 1, pp. 81–87, Jan. 1953.
[52] S. Spinner and G. W. Cleek, "Temperature Dependence of Young's Modulus of Vitreous Germania and Silica," *J. Appl. Phys.*, vol. 31, no. 8, pp. 1407–1410, Aug. 1960.
[53] "Properties: Silica - Silicon Dioxide (SiO2)," *AZoM.com*. [Online]. Available: https://www.azom.com/properties.aspx?ArticleID=1114. [Accessed: 13-Dec-2018].
[54] R. Roy, D. K. Agrawal, and H. A. McKinstry, "Very Low Thermal Expansion Coefficient Materials," *Annu. Rev. Mater. Sci.*, vol. 19, no. 1, pp. 59–81, 1989.
[55] L. Brancato, G. Keulemans, T. Verbelen, B. Meyns, and R. Puers, "An Implantable Intravascular Pressure Sensor for a Ventricular Assist Device," *Micromachines*, vol. 7, no. 8, p. 135, Aug. 2016.
[56] BCCDC, "Section 7 The Use of Electromagnetic Fields in Medicine and Its Effect on Patients and Health Care Workers." [Online]. Available: http://www.bccdc.ca/health-professionals. [Accessed: 25-Mar-2017].
[57] É. Pinet, E. Cibula, and D. Đonlagić, "Ultra-miniature all-glass Fabry-Pérot pressure sensor manufactured at the tip of a multimode optical fiber," 2007, p. 67700U.

[58] A. M. Torgalkar, “A resonance frequency technique to determine elastic modulus of hydroxyapatite,” *J. Biomed. Mater. Res.*, vol. 13, no. 6, pp. 907–920, 1979.
[59] P. M. Zavracky, G. G. Adams, and P. D. Aquilino, “Strain analysis of silicon-on-insulator films produced by zone melting recrystallization,” *J. Microelectromechanical Syst.*, vol. 4, no. 1, pp. 42–48, 1995.
[60] P. M. Osterberg and S. D. Senturia, “M-TEST: A test chip for MEMS material property measurement using electrostatically actuated test structures,” *J. Microelectromechanical Syst.*, vol. 6, no. 2, pp. 107–118, Jun. 1997.